Modelling and Simulation of Concentrated Photovoltaic / Thermal (CPV/T) Collector with a Novel Approach towards the Design of Concentrator for Residential Buildings

Leo Dixon Alphonse Irudhayaraju

A Thesis

in

The Department

of

Building, Civil and Environmental Engineering

Presented in Partial Fulfillment of the Requirements

for the Degree of Master of Applied Science (Building Engineering) at

Concordia University,

Montreal, Quebec, Canada

August 2021

© Leo Dixon Alphonse Irudhayaraju, 2021

CONCORDIA UNIVERSITY

School of Graduate Studies

This is to certify that the thesis prepared

By: Leo Dixon Alphonse Irudhayaraju

Entitled: Modelling and Simulation of Concentrated Photovoltaic / Thermal (CPV/T) Collector with a Novel Approach towards the Design of Concentrator for Residential Buildings

and submitted in partial fulfilment of the requirements for the degree of

Master of Applied Science Building Engineering

complies with the regulations of the University and meets the accepted standards with respect to originality and quality.

Signed by the Chair on behalf of the final examining committee:

_____ Chair
Dr. R. Zmeureanu

_____ Examiner
Dr. A. Athienitis

_____ Examiner
Dr. L.A. C. Lopes

_____ Examiner
Dr. R. Zmeureanu

_____ Thesis Supervisor(s)
Dr. M. Nokken

Approved by _____
Dr. M. Nokken, GPD
Department of Building, Civil, and Environmental Engineering

2021-02-26_____
Dr. M. Debbabi, Dean of Faculty

Abstract

Modelling and Simulation of Concentrated Photovoltaic / Thermal (CPV/T) Collector with a Novel Approach towards the Design of Concentrator for Residential Buildings

Leo Dixon Alphonse Irudhayaraju

The need to address the rising energy demand through clean energy and efficient management of such generated energy ranging from single family residence to larger communities has laid the foundation for this research. The necessity to accomplish this task without polluting the environment has set the path towards generating renewable energy in reliable ways, capable of sustaining distributed generation and decentralized grid architecture.

This thesis presents a hybrid model of concentrated photovoltaic / thermal collector (CPV/T) and its methodology, with waste heat recovery for domestic hot water consumption suitable for residential buildings.

This hybrid is the combination of two systems: concentrated photovoltaic (CPV) and solar thermal collector (STC). The CPV system generally concentrates inbound solar energy onto a smaller surface. The concentrator is modelled based on square spherical mirrors with a novel approach to attain uniform irradiation. This smaller surface is fitted with a photovoltaic (PV) modules made up of multi-junction solar cells (MJSC), which provide electrical outputs. This PV module is specifically chosen for this concentrator design. The module is fixed with a thermal collector to deliver the usable thermal energy to the storage tank.

This hybrid model is designed and a case study of a residential building based of Arkansas is simulated using eQuest. The energy consumption based on various parameters of an average residential building in Arkansas is prepared from ACEEE to establish the electric and thermal demand profile (Neubauer and Nadel 2011). A comparison graph is plotted to understand the influence of our proposed system on the existing energy demand and supply curve. The electrical efficiency of the system produces 5 kW_p along with a 50% thermal efficiency. The reduction in the cost of electricity is discussed along with it net metering arrangement.

Acknowledgement

This research work would not have been possible without the guidance of several individuals who in one way or another contributed their time and energy in the preparation and completion of this study. I would like to take this opportunity to thank each and every one of you for believing in me. This journey began in 2015, under the guidance of Dr. M. Zaheeruddin, in collaboration with Innovative Solar Power Inc. Despite being in a new country, surrounded by a new culture and lifestyle, my drive and determination remained unwithered.

It was in 2018 that life decided to throw a curve-ball my way, leading to a decline in my mental health. I watched, as my flame of ambition become lethargic and slowly start to fade. Life truly changed, as I contemplated giving up, and prepared to head back, wanting to wash away my dismay in the comfort of home.

It is with immense gratitude that I acknowledge the support of my family and friends, re-directing me towards the help I needed and re-igniting the passion within me. By mid-2019, I started to once again believe I could successfully complete this research.

This thesis would have remained a dream, had it not been for Dr. M. Nokken, my administrative supervisor. I thank you for embarking on this project and for your ongoing support since. I would also like to thank the members of my committee, Dr. A. Athienitis, Dr. L.A. C. Lopes, and Dr. R. Zmeureanu.

To my parents, Alphonse Irudhayaraju and Margret Auxillia, my sister, Emily Alphonse, my love, Eanjalin Kamaleswaran, and her entire family, my school friends, Sam Prabu Rajendran, the Concordians who have become lifelong friends, Duraichelvan Raju, my same same but dif-friends, and all those who have come on and gone throughout the tears and joy; I thank you all from the bottom of my heart. I will forever embrace all that you have done for me and am forever indebted to your love and care. Thank you, thank you and thank you!

Table of Contents

List of Figures viii
List of Tables xi
Nomenclature xii
Abbreviation xiv

1. Introduction 1
    1.1 Background 1
    1.2 Problem Statement 3
    1.3 Motivation 4
    1.4 Objective 4

2. Literature Review 5
    2.1 Introduction 5
    2.2 Basics of Concentrators 5
    2.3 Imaging vs. Non-imaging Optics 6
    2.4 Types of Concentrators 7
    2.5 History of Concentrators 7
        2.5.1 Circular and Parabolic Trough Models 7
        2.5.2 Fresnel Lens Models 10
        2.5.3 Parabolic Dish Models 14
        2.5.4 Hyperbolic Models 17
        2.5.5 Paraboloidal Models 18
        2.5.6 Hybrid Fresnel Models 20
    2.6 Multi Junction Solar Cell 21
        2.6.1 History of Multi Junction Solar Cell 22
        2.6.2 Fabrication Process of Multi Junction Solar Cell 22
        2.6.3 Characteristics Determination of Multi Junction Solar Cell 23
        2.6.4 Selection of Multi Junction Solar Cell 24
    2.7 Tracking System 25

3 Mathematical modelling of Reflectors 26
    3.1 Introduction 26
    3.2 Components of Ray Tracing 26
    3.3 Hemispherical Reflection Model 29
    3.4 Paraboloidal Reflection Model 31
    3.5 Selection of Reflector Profile 33
    3.6 Design of Base Reflector 34
    3.7 Approximation Equation 35
    3.8 Area of Curved Surface (3 Dimensional) 37
    3.9 System Design Parameters 38
    3.10 Design of Individual Reflector 39
    3.11 Rim Angle of Individual Reflector 39
    3.12 Focal Length of Individual Reflector 40
    3.13 Modified Focal Length of Individual Reflector for Parallel Rays 41
    3.14 Effect of Solar Disc Angle on Modified Focal Length 42

3.15 Design of Collective Reflectors 43
3.16 Design Consideration of Base Model 45
3.17 Revised Position of the Reflectors – Design Iteration 2 46
3.18 Modified Focal Length of Revised Collective Reflector 47
3.19 Revised Position of the Reflectors – Design Iteration 3 49

4 Thermal Modelling of receiver 51
4.1 Introduction 51
4.2 Flat Plate Collector 51
4.2.1 Analysis of CPVT Collector 52
4.2.2 Thermal Network of Proposed Model 53
4.3 Thermal Storage Tank 56

5 Case Study 57
5.1 Background 57
5.2 Location Analysis 57
5.3 Building Description 59
5.4 Building Shell 59
5.5 HVAC Specification 60
5.6 Simulated Results 61
5.6.1: Input data to eQUEST 61
5.6.2: Output data from eQUEST 61

6 Results 63
6.1 Ray Trace on Reflectors 63
6.1.1 Vertex approximation for profile selection of reflectors 63
6.1.2 Effect of solar angular profile on single reflector 64
6.1.3: Collective Reflector 66
6.2 Uniformity Analysis of Concentrated Solar Irradiation 67
6.2.1: Design iteration 1 67
6.2.2: Design iteration 2 69
6.2.3: Design iteration 3 70
6.3 Output data 71
6.4 Assumptions made in optics modelling 72
6.5 Thermal Modelling 73
6.5.1: Effect of CPV plate temperature on the solar collector 73
6.5.2: Effect of STC water outlet temperature on the solar collector 73
6.5.3: Thermal performance of STC 74
6.5.4: Energy balance on a Storage tank 74
6.6 Energy demand – supply curve 78
6.7: Assumptions made in thermal modeling 80

7. Conclusion 81
7.1 Contributions 81
7.2 Future Work 81
References 82
Appendices 89
Appendix A Solar insolation 89

Appendix B Solar radiation on inclined surface 90
Appendix C Steady State Analysis 92

List of Figures

Figure 1 Comparison of U.S energy consumption (U.S. EIA, 2019) 1
Figure 2: Utility-scale electricity generation (U.S. EIA, 2019) 1
Figure 3: Schematic representation of CPV / CSP method 2
Figure 4: 3D rendering of CPV/ T method 3
Figure 5: Reflected ray-diagram of a mirror – circular cross section (Nijegorodov, Jain, and Devan 1995) 8
Figure 6: Dependence of focal length of a mirror with circular cross-section on the rim angle (Nijegorodov, Jain, and Devan 1995) 8
Figure 7: Incident radiation is reflected from the primary mirror and focused on the target through a secondary mirror (Rogers et al. 2012) 9
Figure 8: Proposed Fresnel based photovoltaic concentrator (Benítez et al. 2010) 11
Figure 9: Comparison of Fresnel based concentrator with respect to SOE (Benítez et al. 2010) 11
Figure 10: Homogenized irradiation on the solar cell - reduced hotspots (Benítez et al. 2010) .. 12
Figure 11: Design based on refractive prisms with proposed homogenized function with varying slopes (Pan et al. 2011) 13
Figure 12: Compound Fresnel design based photovoltaic concentrator (Jing et al. 2012) 14
Figure 13: Dish facets proposed by Zanganeh (Zanganeh et al. 2012) 15
Figure 14: 3D Crossed Compound Parabolic Concentrator (CCPC) (Sellami and Mallick 2013) 16
Figure 15: 3D Elliptical Hyperboloid Concentrator (EHC) (Saleh Ali et al. 2013) 17
Figure 16: Schematic representation of helmet concentrator with Fresnel and reflection losses (Canavarro, Chaves, and Collares-Pereira 2014) 19
Figure 17: Schematic representation of edge rays: XX SMS concentrator (Canavarro, Chaves, and Collares-Pereira 2014) 19
Figure 18: PT concentrator with centre of mass G_c (Canavarro, Chaves, and Collares-Pereira 2014) 19
Figure 19: XX SMS concentrator with centre of mass G_c (Canavarro, Chaves, and Collares-Pereira 2013) 20
Figure 20: Proposed novel hybrid Fresnel based concentrator (Zhuang and Yu 2014) 20
Figure 21: Schematic representation of triple junction solar 21
Figure 22: Semiconductor structure of GaInP/GaInAs/Ge, BC – bottom cell, MC – middle cell, TC – topcell, TJ – tunnel junction (Barrutia et al. 2018) 22
Figure 23: Voltage and efficiency characteristics of GaInP/GaInAs/Ge (Takamoto et al. 2005) 23
Figure 24: Temperature dependence of principle photovoltaic parameters for GaInP/GaInAs/Ge (Yang et al. 2011) 24
Figure 25: I-V and concentration characteristics of InGaP/GaAs/InGaAs (Sasaki et al. 2013) ... 24
Figure 26: Performance of GaInP/GaAs//Si (Cariou et al. 2018) 25
Figure 27: Performance comparison of GaInP/GaAs//Si vs GaInP/GaAs/ InGaAs (Kao et al. 2019) 25
Figure 28: Equation of solar ray $\overrightarrow{AB}$ in terms of known $\vec{q}$ 26
Figure 29: Equation of solar ray $\overrightarrow{AB}$ with respect to $\vec{n}$ 27
Figure 30: Vector representation of incident and reflected ray 28
Figure 31: Specular reflection of solar ray $\overrightarrow{AB}$ by a spherical surface (Pereira, Fernandes, and Guerra Rosa 2019) 29

Figure 32: Specular reflection of solar ray $\overrightarrow{AB}$ by a paraboloidal surface (Pereira, Fernandes, and Guerra Rosa 2019) 32
Figure 33: Parabolic mirror behaviour – axial incident (Rogers et al. 2012) 33
Figure 34: Circular mirror behaviour – axial incident (Rogers et al. 2012) 33
Figure 35: Parabolic mirror behaviour – off axis incident (Rogers et al. 2012) 34
Figure 36: Circular mirror behaviour – off axis incident (Rogers et al. 2012) 34
Figure 37: Iso view of Concentrator Optics along with receiver 34
Figure 38: Top and Side view of Concentrator Optics without receiver 35
Figure 39: Reflection of light rays parallel to axis of spherical mirror (not to scale) 35
Figure 40: Near vertex approximation of circle and parabola ("Desmos | Graphing Calculator" n.d.) 36
Figure 41: Representation of surface area of reflector 37
Figure 42: Simple curvature profile of single mirror 39
Figure 43: Rim angle of individual r eflector 39
Figure 44: Ray tracing of a single reflector with large radii of curvature (TracePro) 41
Figure 45: Modified focal length of incident ray 41
Figure 46: Modified focal length with solar disc angle 42
Figure 47: Numerical representation of reflectors with highlighted 1/4th receiver area (a) and determination of incident angle for each reflector using single ray trace technique 44
Figure 48: Pictorial representation of single ray trace on 4th reflector 44
Figure 49: Radius of curvature of reflector design – iteration 1 44
Figure 50: Side view of collective reflectors 45
Figure 51: Dependence of focal length of proposed mirror design with circular cross-section on the rim angle (Nijegorodov, Jain, and Devan 1995) 46
Figure 52: (a) Design iteration 2 and (b) single ray trace technique to determine incident angle 46
Figure 53: Shading on the receiver due to change in orientation of the 1st reflector 48
Figure 54: (a) Design iteration 3 and (b) single ray trace technique to determine incident angle 49
Figure 55: Schematic representation of thermal collector design 51
Figure 56: Serpentine model water path 51
Figure 57: Cross sectional view of proposed solar collector 52
Figure 58: Thermal network in terms of conduction, convection and radiation resistance 53
Figure 59: Simplified thermal network: (a) resistance between plates and (b) overall loss coefficient 53
Figure 60: Schematics of absorber plate with water tubes 54
Figure 61: Unstratified water tank storage operating at temperature Ts in ambient condition 56
Figure 62: The floor plans are courtesy of plan image architectural design services 57
Figure 63: US Map of Köppen–Geiger Climate Classification (Kottek et al. 2006) 58
Figure 64: Direct Normal Irradiance of Little Rock, USA 58
Figure 65: Dry Bulb Temperature of Little Rock, USA 58
Figure 66: Prototype model developed and simulated in eQuest 59
Figure 67: Air side HVAC system 60
Figure 68: Water side HVAC system 60
Figure 69: Bar chart: Peak demand and Energy consumption of prototype model 61
Figure 70: Monthly energy consumption of prototype model (kWh X000) 62
Figure 71: Monthly peak demand by end use (kW) 62
Figure 72: Paraxial rays incident on reflector 63
Figure 73: Concentrated rays on the receiver from a circular shape 64

Figure 74: Concentrated rays on the receiver from a parabolic shape....64
Figure 75: Solar angular profile rays incident on single reflector....64
Figure 76: Contour graphs of concentrated rays for (a) spherical and (b) paraboloidal profiles..65
Figure 77: Concentrated rays of (a) spherical and (b) paraboloidal profile....65
Figure 78: Conceptualized base reflector construction support....66
Figure 79: Schematic representation of ray trace on the entire assembly....67
Figure 80: Receiver with MJSC (45mm x 45mm)....68
Figure 81: Concentrated solar irradiation distribution on the receiver (W/m2) 68
Figure 82: Displacement error based on position: iteration 1....69
Figure 83: Concentrated solar irradiation distribution on the receiver (W/m2) 69
Figure 84: Displacement error based on position: iteration 2....70
Figure 85: Concentrated solar irradiation distribution on the receiver (W/m2) 70
Figure 86: Displacement error based on position: iteration 3....71
Figure 87: Concentrated solar irradiation on the receiver surface....71
Figure 88: Comparison between concentrated solar irradiation on the receiver for the (a) proposed design vs the (b) paraboloid design 72
Figure 89: Change in CPV absorber plate temperature with different mass flow rates 73
Figure 90: Change in outlet water temperature with different mass flow rates....74
Figure 91: Thermal efficiency of collector 74
Figure 92: Integration of proposed model with the residential building 75
Figure 93: Energy balance equation on March 4th, 2019 – coldest day....75
Figure 94: Energy balance equation on March 19th, 2019 – spring equinox 76
Figure 95: Energy balance equation on June 21st, 2019 – summer solstice....76
Figure 96: Energy balance equation on August 13th, 2019 – hottest day 77
Figure 97: Energy balance equation on September 23rd, 2019 – fall equinox 77
Figure 98: Energy balance equation on December 21st, 2019 – winter solstice 77
Figure 99: Demand vs Supply on March 4th, 2019 – coldest day 78
Figure 100: Demand vs Supply on March 19th, 2019 – spring equinox 78
Figure 101: Demand vs Supply on June 21st, 2019 – summer solstice 79
Figure 102: Demand vs Supply on August 13th, 2019 – hottest day 79
Figure 103: Demand vs Supply on September 23rd, 2019 – fall equinox 79
Figure 104: Demand vs Supply on December 21st, 2019 – winter solstice 80
Figure 105: ASTM G173-03 Reference Spectra derived from SMARTS v. 2.9.2....89
Figure 106: Schematics of Solar angles....90
Figure 107: Temperature distribution on the receiver at highest concentrated solar irradiation..92
Figure 108: Temperature distribution on the receiver at lowest concentrated solar irradiation ...93

List of Tables

Table 1: Design iteration 1 – Focal length, angle and radius of reflectors 45
Table 2: Design iteration 2 – Focal length, angle and radius of reflectors 47
Table 3: Design iteration 3 – Focal length, angle and radius of reflectors 50

Nomenclature

η_{opt}	Optical Efficiency
NR_i	Number of Reflections
φ	Rim Angle
C	Concentration
°	Degree
°C	Degree Celsius
A	Area
a.u.	Arbitrary Unit
Abs	Absorber plate
A_l	Arc length
A_p	Aperture area
b	Vertical Displacement
C	Concentration
C_b	Bond Conductance
f	Focal Length
g	Grams
G_c	Center of mass
h	Hours
h	Hydraulic
I	Intensity
J	Joule
k	Thermal Conductivity
kg	Kilogram
kJ	Kilojoule
kWh	Kilowatt-hour
kWp	Kilowatt-peak
l	Length
L	Liter
m	Meter
mm	Milimeter
n	Number of Rays
Q	Energy
Q_u	Solar radiation absorbed by the collector
R	Radius of Curvature
r	Radius
s	Seconds
solar	Solar Rays
SPV	Solar Radiation absorbed by the CPV module
U	Loss Coefficient
uni	Uniform Rays
W/m^2	Watts per $meter^2$
θ_h	Half Acceptance Angle
ρ	Reflectance
$COPth$	Thermal coefficient of performance of the SDC system

Cp	Specific Heat of Air (J/kg°C)
DHi	Hydraulic Diameter (m)
fi	Friction Factor
θ	Angle
$f*$	Factor

Abbreviation	Definition
1D	One-dimensional
2D	Two-dimensional
3D	Three-dimensional
AADAT	Azimuth-altitude dual-axis tracker
Al	Aluminium
As	Arsenide
BIPV	Building integrated photovoltaic
CAP	Concentration Acceptance Product
CCPC	Cross compound parabolic concentrators
conv	Convergence
CPC	Compound parabolic concentrator
CPV	Concentrated Photovoltaic
CPV/T	Concentrated Photovoltaic / Thermal
CR	Concentration Ratio
CSP	Concentrated Solar Power
DTIR	Double Total Internal Reflection
EHC	Elliptical Hyperboloid Concentrator
FK	Fresnel Kohler
FPLT	Fermat's Principle of Least Time
Ga	Gallium
Ge	Germanium
HCPV	High concentration photovoltaic system
HPC	Hyper-Parabolic concentrators
HVAC	Heating, Ventilation, and Air Conditioning
in	Incident
In	Indium
ir	Individual reflector
I-V	Current-voltage
LCA	Linear chromatic aberration
LCPV	Low concentration photovoltaic system
MCPV	Medium concentration photovoltaic system
MJSC	Multi-junction Solar Cells
MOCVD	Metal organic chemical vapour deposition
mod	Modified
MOVPE	Metal organic vapour phase epitaxy
opt	Optic
P	Phosphide
PC	Polycarbonate
PMMA	Poly methyl methacrylate
POE	Primary Optical Element
PT	Parabolic Trough
PV	Photovoltaic
rec	Receiver
ref	Reflectors
Rev	revised position
R-R	Reflector-Receiver
RTP	Dielectric-filled truncated pyramid
SEH	Square Elliptical Hyperboloid

Si	Silicon
SILO	Single Optical surface
SMS	Simultaneous Multiple Surface
SOE	Secondary Optical Element
sr	Single reflector
STC	Solar Thermal Collector
TIR	Total internal reflection
TTDAT	Tip-tilt dual-axis tracker
UHCPV	Ultra-high concentration photovoltaic system
XR	Reflection-Refraction
XTP	Hollow-reflective truncated pyramid
XX SMS	Double reflection Simultaneous Multiple Surface
XXR	Double Reflection-Refraction

1. Introduction

1.1: Background

The global energy crisis is on the rise due to multiple factors such as the depletion of fossil fuel resources, climate change, and a hike in energy demand in relation to the increasing population. In terms of energy consumption, the USA accounts for 17% of world energy consumption, and ranks second behind China. Figure 1 pictorially represents the breakdown of USA's power consumption by source and end sector. Fossil fuel remains the highest source among all the available resources at 79.94%.[1] Residential buildings in America consume about 16% of total energy generated, but only 29% of the energy consumed by the residential end sector is generated by renewable energy.[1]

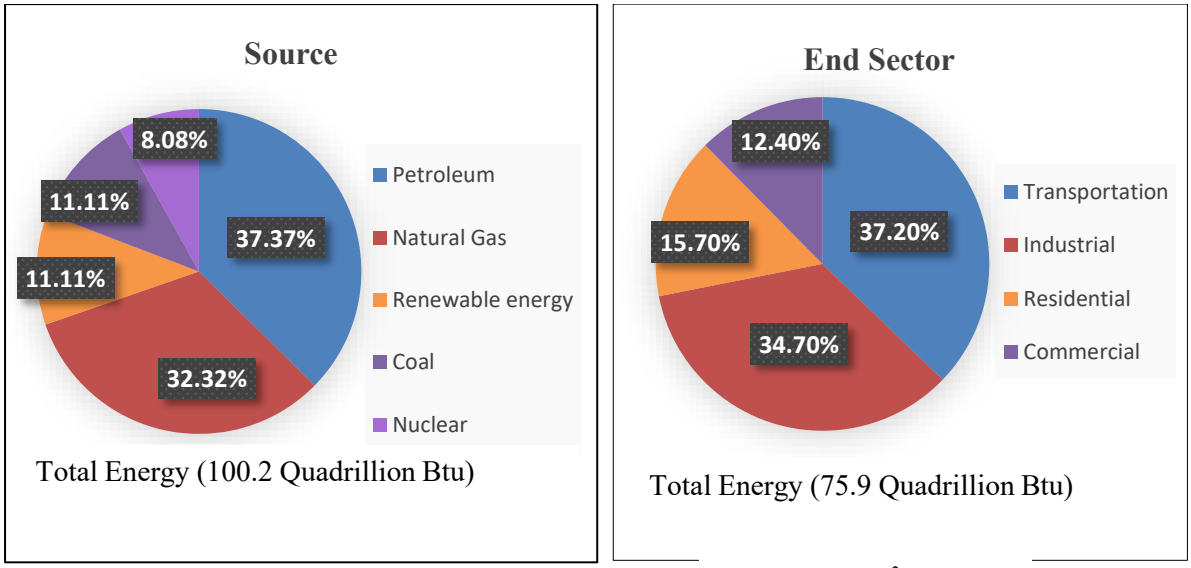

Figure 1: Comparison of U.S energy consumption[2]

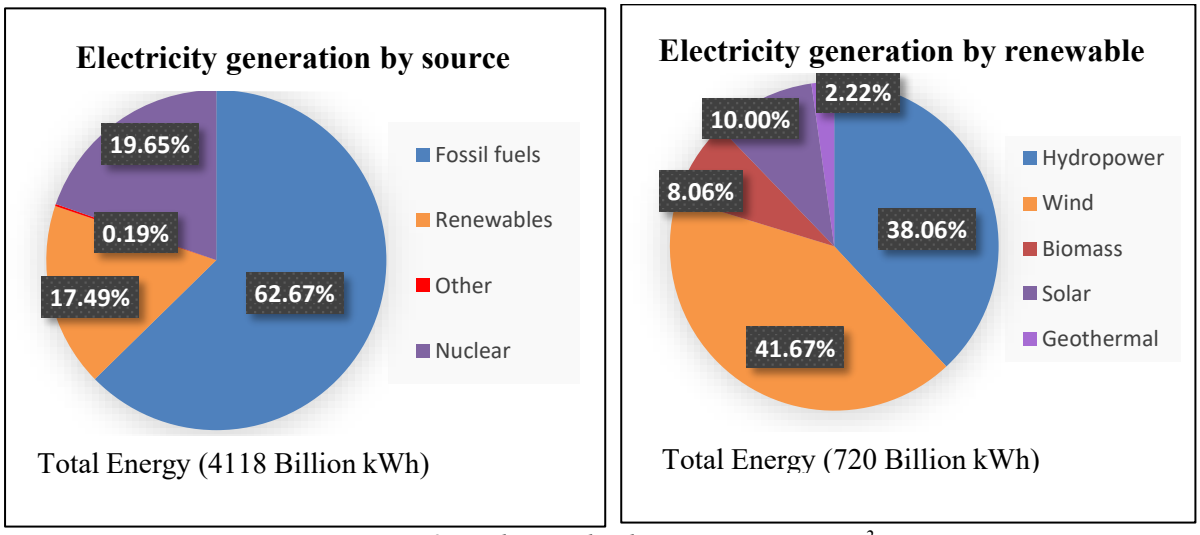

Figure 2: Utility-scale electricity generation[2]

1. "U.S. Energy Facts Explained - Consumption and Production - U.S. Energy Information Administration (EIA)." n.d. Www.eia.gov. https://www.eia.gov/energyexplained/us-energy-facts.
2. "Total Energy - U.S. Energy Information Administration (EIA)." 2016. Eia.gov. 2016. https://www.eia.gov/totalenergy/.

This report also indicates that solar renewable sources used for electricity generation amount to a mere 1.8%.[1] In addition, it is also estimated that 65% of the total energy input to the electrical system is lost during production, transmission, and distribution due to the centralized grid architecture.[1]

Fossil fuels are a non-renewable resource with an eventual depletion potential, and negative environmental impact, resulting in climatic change. In order to meet the energy demands without increasing carbon emissions, energy generation should tilt towards renewable sources.

In general, various components contribute towards selection of a particular renewable technology, including but not limited to: location, reliability, space, application, output capacity, and cost. For example: hydro energy depends on location, whereas, wind energy depends on the season, and may also require human intervention for maintenance. In contrast, solar energy is available in abundance wherever solar radiation falls on earth. Harvesting solar energy is relatively easy, and the conversion to electricity is cost efficient. As well, it has a minimal impact on the environment. The cons to adopting solar energy are that the harvesting is limited to daytime, and the cost of converting solar light into electricity spikes up with the increase of the solar cell's efficiency. In addition, the requirement to setup inverters and batteries for sustainability, and the mismatch between hours of energy availability vs. hours of energy demand add to the overall expenses. Another limiting factor is space requirement; the higher the energy demand, the larger the amount of space needed.

Furthermore, there are locations where the use of a regular grid is scarce. This is especially true for rural regions, limiting the capacity of such energy sources to fuel the day to day needs. Distributed solar power generation can prove effective in such scenarios.

Solar technology is still an emerging renewable energy source among other sources, and thus far has the least negative environmental impacts. Solar power is compatible for both urban, and rural areas, as well, is compatible for residential, and utility scale developments. This technology is continually reinvented with ongoing research, and has the potential to emerge as the main energy source of our planet, in turn contributing to lower cost per kWh, and improved energy conversion efficiency.

At this time, there are only a few established solar power plants around the world given that the fullest harvest potential has yet to be reached. Solar power plants are classified in different categories, such as, photovoltaic power plants, solar thermal power plants and the recently upcoming concentrated solar plants. In this research work, the importance and underlying problems of concentrated solar technologies are explored.

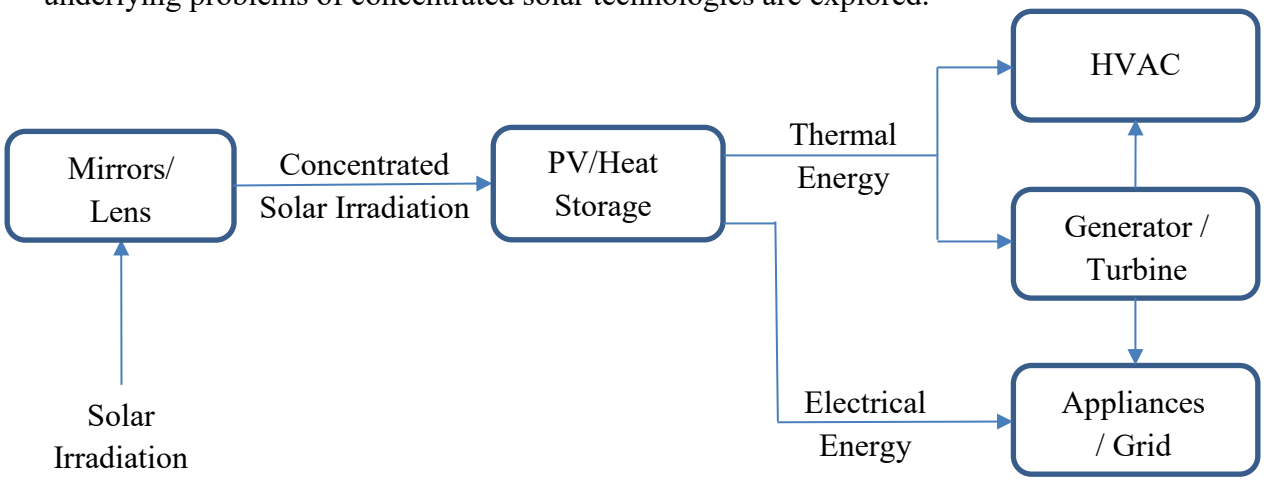

Figure 3: Schematic representation of CPV / CSP method

1. "U.S. Energy Facts Explained - Consumption and Production - U.S. Energy Information Administration (EIA)." n.d. Www.eia.gov. https://www.eia.gov/energyexplained/us-energy-facts.

Concentrated solar technology is an emerging technology that has great potential for replacing non-renewable energy sources due to its cost effective approach towards energy conversion methods. It combines solar cells or heat storage with low cost reflectors or lenses. The energy output of this technology is relatively high compared to the existing solar technologies. There are many types of solar concentrators, but all designs focus on an increased efficiency to lower cost ratio.

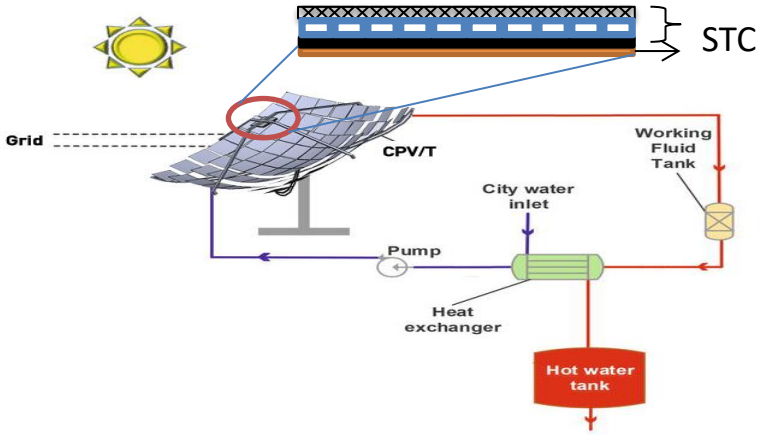

Figure 4: 3D rendering of CPV/ T method

CPV systems predominantly use high efficiency solar cells which are expensive. In order to compensate for the expenses incurred from the solar cells, these systems deploy cost effective components for concentrating the solar radiation. This reduces the overall expense of the proposed system, as the size of the solar cells employed are reduced. This system uses optics to concentrate the light. However, the optics are only functional in the presence of directional light. These high concentration systems have very small acceptance angles and therefore, require aligned parallel light. This parallel light can be achieved if the refocused solar radiation hits perpendicularly to these high efficiency cells.

The optics used for concentration is mounted on a tracking system, which follows the path of the sun during daytime. Accuracy of these tracking systems play a vital role, but can also prove expensive. The system is optimized between the accuracy of the tracker, and expenses of the system itself. CPV systems are designed based on several aspects such as concentration ratio, type of optics, and tracking requirements.

1.2: Problem Statement

In current times, residential homes adopt solar technology as a secondary source of energy generation, heavily relying on the conventional sources (predominantly non-renewable). The dependence on non-renewable sources is due to the fact that solar generation alone is unable to meet the energy demands. As such, this continues to be used as a support system. The primary reason for this existing scenario is the lower efficiency of photovoltaic panels, which use carbon silicon solar panels. The system becomes expensive when coupled with thermal collectors due to the increased size of the entire setup. On the other hand, small scale concentrated technologies focused on residential needs continue to be under development.

Recent developments have increased the efficiency of solar cells by two-folds with use of MJSC instead (Canavarro, Chaves, and Collares-Pereira 2013). The use of a higher concentration factor in CPV/T helps retain a higher efficiency of the electrical output, provided

that the solar cells are cooled down by thermal collectors, which in turn, helps with the thermal efficiency of the collector part. The hybrid model is reflected in the quantitative ratio of energy generated to the area occupied.

1.3: Motivation

Canavarro et al proposed a design with a single parabolic trough, and no secondary optic, resulting in 70x the concentration without affecting the optical tolerance, acceptance angle, or solar distribution (Canavarro, Chaves, and Collares-Pereira 2013). They then went on to propose a design which involved simultaneous multiple surface (SMS) secondary optics, reaching over 200x with increased acceptance angle. Their recent proposal featured a concentrator design using a larger aperture area with the limitation of design not surpassing medium concentration (10-100 suns). Although research suggests that Fresnel lenses outperform parabolic lenses, the parabolic reflector system has been underrated due to the lack of related research.

1.4: Objective

This research focuses on concentrated solar technology, due to its ability to replace other sources of energy generation with respect to residential buildings. The study and analysis of existing CPV systems has given an opportunity to implement such systems to a single residential house to meet their energy demands. This study has led to the following conclusions.

- The current CPV plants commonly in use can be modified and adapted to suit the needs of a single residential house. This adaptation gives rise to a distributive energy management system and has led to the performance investigation of such systems in terms of meeting the energy demands altogether.
- A novel approach is proposed for the design of concentrators. This design is mathematically modelled and simulated. The obtained data is further validated by use of the optical analysis program, TracePro.
- A simple STC is designed and a steady state analysis is simulated. The integration of the proposed model and STC gives rise to a hybrid model setup.
- The STC acts as an active cooling system for the solar cells and delivers waste heat recovered as thermal output used for domestic hot water.
- Various MJSC were studied in order to choose a suitable cell for the proposed model.
- The proposed system only requires a medium precision tracking, as the optical tolerance of the system is slightly higher than existing designs. This comparatively lesser precise tracking system renders the overall system cost effective.
- The energy demand of a residential building is simulated using energy management software to support the claim.
- The proposed system delivers high energy output in comparison to existing systems.
- An energy demand and supply curve is studied and compared.
- The proposed system has taken into consideration ease of operation with reduced complexity, whereas existing systems adopt secondary systems to compete with other technologies or are less efficient by nature due to the simplicity of the system design. The lower complexity of the proposed design with higher efficiency gives it advantage over existing technologies found on the market.

2. Literature Review

2.1: Introduction

The sun provides the Earth with 89 peta-joules of energy per second. However, the capacity to utilize this energy in an efficient and economical way remains to be challenging. In order to amplify the use of solar energy, we rely extensively on CPV systems, which use MJSC. MJSC have the potential to work at higher efficiencies under concentrated solar irradiation. In today's world, optical integrated devices are used to replace PV solar cells in order to capture solar irradiation in an effective way. This in turn reduces the cost of the system without compromising the amount of solar radiation captured. The replacement of the expensive PV material by more affordable mirrors and/or lenses not only leads to more economical systems, but also retains the surface area in which energy is captured (Shanks, Senthilarasu, and Mallick 2016). At this time, CPV systems are still at the initial stages of research, working to achieve low cost high efficiency systems when compared to commercially available PV systems.

The focus of research and development in CPV technologies aim to gradually increase the efficiency of these systems. In addition, the proven effect on albedo change, and reduction in CO_2 emission with the use of lower semiconductor components by CPV systems, as opposed to commercial PV panels, indicate CPV systems have a lower impact on the environment (Shanks, Senthilarasu, and Mallick 2016). Despite the many advantages of the proposed technology, the present day commercial market poses great difficulty to surpass the economic dominance posed by the flat plate PV. In order to combat this dominance, extensive research is required in designs resulting in reliable, high concentrated optics with a lower dependency on tracking, and inexpensive cooling systems. The other aspect of the design should focus on solar cells, specifically on fabrication technique, and optimised cell size, to suit the design parameters of optics.

The following literature review provides information on various designs in order to help understand the progress made in the field of CPV. These solar concentrator technologies vary on the basis of differing parameters such as, types of systems, design structure, efficiency, materials, limitations, and their advantages over one another. This review also establishes a simplification of the categories to better determine the appropriate design for the desired application.

2.2: Basics of Concentrators

The significant progress made in the field of concentrated solar technology over the past few decades is evenly distributed within the categories of solar cells, cooling systems, and optical accuracy. This review will focus on the aspects of optics, its accuracy, and a new category of concentrated solar technology.

Every system's optics design begins by first establishing a concentration ratio based on the energy requirement and ground area availability. The definition of concentration ratio (CR) is directly linked to the geometrical CR, optical CR or flux CR as such

$$\text{Geometrical CR} \times \text{Flux CR} = \text{System concentration}$$[3]

CR can be manipulated in many ways. One such way includes the use of stages of concentration multipliers such as single stage, double stage or more. However, there remains a preference towards a lower number of stages in order to reduce the overall complexity, and

[3] Stine 2010

uncertainty of the system. The outline of the CPV system dictates that a single stage design possesses a primary optic with possible additional optics such as secondary and tertiary in direct correspondence to each additional stage.

The primary optics, also referred to as high concentration, serves to collect the incident light and concentrate it, thereby increasing the number of 'suns'. The secondary optics, or, receiver optics, produces a lower concentration of 'suns' when compared to the primary. This optics serves the purpose of improving the system's angle and irradiance distribution on the PV. The secondary optics is also referred to as a low or medium concentration because of its inability to concentrate as many 'suns' as many as the primary optics.

The use of secondary optics is often accompanied by a tracking method; this integration leads to enhanced performance of the CPV system. The function of the tracking system determines the characteristics of the concentrator, specifically whether it will be two-dimensional (2D) or three-dimensional (3D). 2D concentrators are usually described as line-focused systems, as they track the sun's rays linearly or along a single axis, and are predominantly used in thermal concentrator systems. The need for symmetry can be observed in these profiles due to their geometrical design along the axis. 3D concentrators track the sun's rays along a plane, adopting a dual-axis tracking to fulfil their purpose of high performance. These systems are described as point-focused systems, and are predominantly used in cassegrain setups. These systems do not have the necessity of symmetry, but rather may lead to the irregular distribution of solar irradiation. The geometrical design of a line-focused 2D design can be extended into point-focused 3D design, and can also be reversed from 3D optics to 2D profiles.

2.3: Imaging vs. Non-imaging Optics

Concentrators are classified based on the formation of optical images. Imaging optics in CPV systems are best described by their ability to refract light from the source to the receiver, while retaining its image, independent of the size formed at its focal plane.

Non-imaging optics are designed specifically to collect solar irradiation in order to maximize optical efficiencies, and increase flux distribution output in accordance with the laws of reflection of solar irradiation. The primary concern of the non-imaging system is its inability to replicate the image of incident solar irradiation onto the reflector, hence the formation of a distorted image at the focal plane. Non-imaging concentrators result in larger aberrations for systems with smaller aperture ratios when used in image forming systems. Geometrical aberrations hinder the performance of imaging optics, and result in a non-ideal environment for them to function.

Imaging optics for concentration has the necessity to treat each ray in the same way, from input reflector to output receiver, resulting in the formation of an image, irrespective of the size. Such optics concentrates through reflection or refraction. A single stage reflection will lead to the formation of an image, and a material with high index will do the same for refraction. Most optical imaging concentrators eliminate rays at varying incident points in an attempt to retain the image within the system, thus compromising on the concentration factor. In contrast, non-imaging concentrators can maximize performance by suiting appropriate conditions to different patterns of irradiation.

The greatest advantage of imaging optics is the capacity of the system to approach the thermodynamic limit of the focussed irradiation, and increased possibility of reaching higher flux levels than its counterpart. The ideal optical system for solar concentrators will have 100% optical efficiency, higher optical tolerance, and maximised acceptance angle providing uniform

irradiance distribution throughout the receiver panel, matching its size and dimensions. In addition, cost effectiveness in terms of manufacture, robustness, and ease of installation must also be considered. Each system has its own advantages and disadvantages. Application and location must be considered when choosing a suitable design.

2.4: Types of Concentrators

CPV systems are widely classified based on their concentration factors, optics, tracking methodology, geometrical design, and number of stages involved within the system. These systems can be grouped into categories. The first category is based on optics, and energy concentration. They are classified as LCPV (low concentration photovoltaic system), which concentrate less than 10 suns, MCPV (medium concentration photovoltaic system), which concentrate between 10 and 100 suns, HCPV (high concentration photovoltaic system), which concentrate between 100 and 2000 suns, and UHCPV (ultra-high concentration photovoltaic system), which concentrate more than 1000 suns. The second category is based on concentrating techniques adopted by the primary optics, namely reflective, refractive, TIR (total internal reflection), and luminescent. The third category is based on the concentrating techniques adopted by secondary optics, namely conic reflector, homogeniser, and CPC (compound parabolic concentrator). The fourth category is based on the tracking method, namely stationary, linear focus tracking, point focus tracking, and quasi static. The fifth and final category is based on the geometry of the CPV optics, including circular, parabolic, hyperbolic, elliptical, dish and trough.

2.5: History of Concentrators

The first reflecting telescope using parabolic mirrors, as opposed to regular spherical mirrors, was built by John Hadley in 1721 (Bell 1922). In solar thermal concentrators, it was Shuman who came up with an external flat reflector; this is what powered a water pumping system in 1911(Butti and Perlin 1980). Lighthouses commonly used parabolic mirrors to collimate a point of light from a lantern into a beam, eventually getting replaced by the higher efficient Fresnel lens. It was Augustin Jean Fresnel, in the year 1822, who first replaced glass collimators by Fresnel lenses in lighthouses (Lloyd 1841). Fresnel lenses weren't affordable until the late 1950s. The affordability and accessibility only increased following the discovery of polymethylmethacrylate (PMMA); making the manufacturing cost of the Fresnel lens cheaper.

In the 1960s, Giovanni Francia applied the concept of Fresnel reflector for industrial thermal processes (Silvi 1995). Following this, in 1978, Sandia National Laboratories built their modern Fresnel lens CPV system (Swanson 2000). The CPV technology witnessed a massive growth after 1988, when experiments were conducted for ultra-high flux measurements at the University of Chicago in 1988 (Winston 1995). These technologies have undergone testing and are now commercialised for small-scale power-production in phases.

2.5.1: Circular and Parabolic Trough Models

Nijegorodov et al, made a theoretical and experimental analysis on a non-tracking cylindrical solar concentrator, which had a circular cross section of radius R (Nijegorodov, Jain, and Devan 1995). A 2d cross section of both the parabolic mirror and circular mirror are compared in this paper.

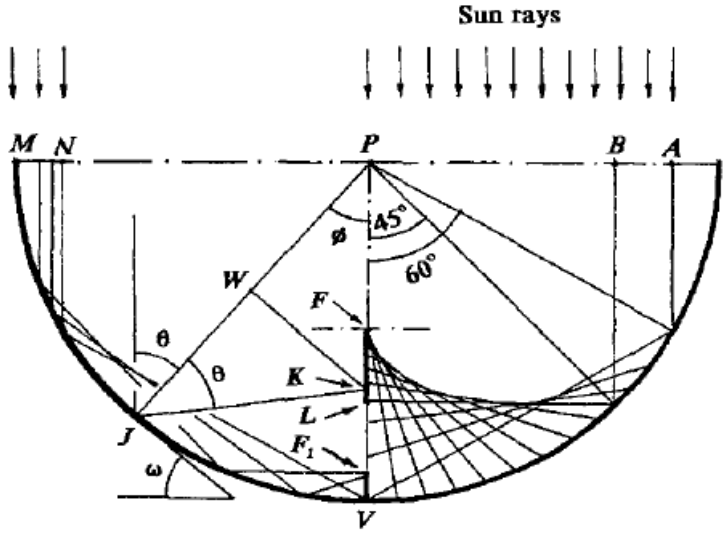

Figure 5: Reflected ray-diagram of a mirror – circular cross section (Nijegorodov, Jain, and Devan 1995)

The focal length of a parabolic mirror is constant irrespective of the rim angle, while that of a circular mirror varies. A relationship between the focal length and rim angle of the circular cylindrical solar concentrator is established. The focal length decreases from 0.5 R to 0 with an increase in rim angle from 0º to 90º. As well, an important correlation between the focal length and the aperture of the mirror is noted. The ratio ($A_p/2f$) of half the linear aperture to focal length is used as a design parameter for both parabolic and circular mirrors. The maximum value of ($A_p/2f$) is 2 for a circular mirror. However, by manipulating the linear aperture, a parabolic mirror ($A_p/2f$) can be as large as need be. The circular mirror of small segments, which has ($A_p/2f$) ≤0.55, has a performance which is in par with the parabolic profile of similar sizes. The rays undergo single reflection for all rim angles ranging from 0º-60º, beyond which the rays undergo multiple reflection to reach the focal length. The focal length (f) is expressed in terms of the radius of curvature with respect to incident angle, where n is the number of reflections, as seen in equation (2.1).

$$f_n(\emptyset) = R\left\{1 + (-1)^n \frac{\sin \emptyset}{\sin\ 2n\emptyset}\right\} \qquad (2.1)^4$$

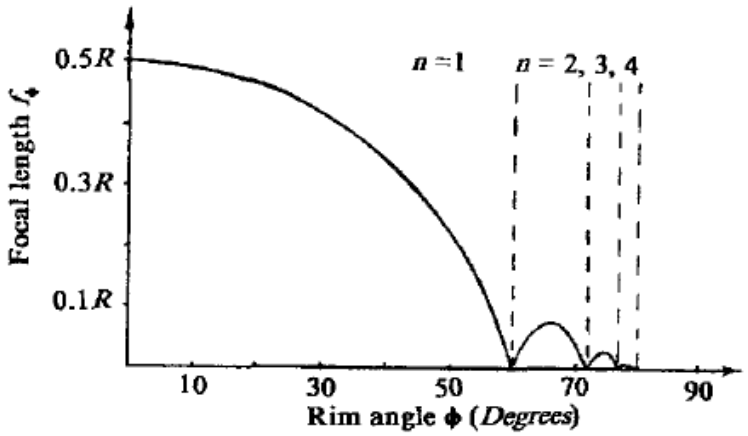

Figure 6: Dependence of focal length of a mirror with circular cross-section on the rim angle (Nijegorodov, Jain, and Devan 1995)

[4] Nijegorodov, Jain, and Devan 1995

Rogers et al, presented a paper on concentrating sunlight with a 3 stage model which consists of immobile primary mirror, mobile secondary mirror and an immobile target receiver (Rogers et al. 2012). The proposed system concentrates sun light at each stage, and the trough geometry exhibits concentration of 38 suns. The primary mirror is made of a circular cross section. The simulation of the ray tracing is carried over by computer codes, and commercially available software. A simple comparison is carried over between circular mirrors, and parabolic mirrors. Traditionally, parabolic mirrors are used for concentration; however, this study focuses on the disadvantage as the aberration increases with this setup, whereas there is a deviation in the solar incidence. In contrast, for any off axis incidence, the circular mirror produces consistent aberrations. Although the setup mentioned in this study reduces the movement of parts in the assembly, which can help the load factor of tracking system, it also increases the complexity of the tracking mechanism, reduces the solar concentration and system efficiency

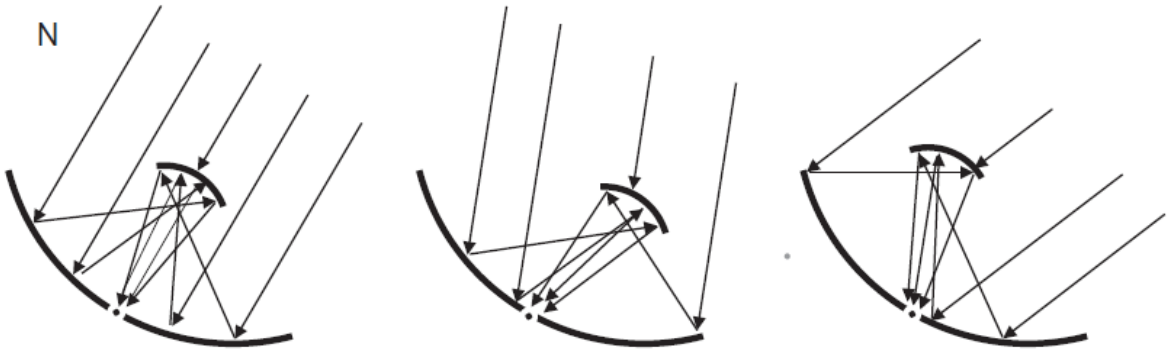

(a) Equinox (b) Summer (c) Winter

Figure 7: Incident radiation is reflected from the primary mirror and focused on the target through a secondary mirror
(Rogers et al. 2012)

Brunotte et al, proposed a two stage concentrator with the concentration factor reaching up to 300, while the system employed a single tracking mechanism (Brunotte, Goetzberger, and Blieske 1996). The first stage consisted of a Parabolic Trough (PT), used to focus irradiation on a second stage fitted with a single axis tracking mechanism. The second stage consisted of dielectric, non-imaging 3D concentrators. The concentrators are coupled with solar cells. The efficiency of the system deeply depends on the angular acceptance of the secondary concentrators. These concentrators have to capture a square shaped angular distribution of solar radiation falling onto the focal line of the PT. A new profile for secondary concentrators is proposed to capture the ideal square acceptance characteristic against the standard CPC. The CPC profile adopted in the earlier designs would have increased the acceptance angle from 23.5° to 57.4°, affecting the concentrator factor by 3.2.

This paper will discuss the potential issues such as, reflective losses at the entrance of the second stage, absorption and scattering of reflected irradiation inside the dielectric, total internal reflection losses due to poor surface finish owed to manufacturing methodology constraints, reflective losses at the solar cell affected by the irradiation profile at the exit of second stage concentrators, and the inhomogeneous illumination of the solar cell affecting the fill factor of the solar cell, thereby reducing the efficiency of the electrical output.

Murphree presented a point focus concentrator, replacing the existing 3D paraboloidal concentrators, which have higher flexibility with respect to specific high concentration designs (Murphree 2001). The point focus concentrator is designed using two reflective PTs. The

orientation of the longitudinal axes of the primary PT is aligned perpendicularly to the secondary PT, and distanced by their focal length difference along the optical axis. This design is more advantageous than the paraboloidal design due to its relative ease of fabrication; manufacturing troughs are simpler. However, the disadvantages of this system include its complexity, and the reduced efficiency, due to use of two PTs and its double reflection. The secondary trough is also an imaging mirror, which reduces the concentration. In addition, there is a shading factor, where the incident radiation is blocked by secondary troughs.

Nilsson et al, published an article on micro structured reflector surfaces for a stationary asymmetric parabolic solar concentrator (Nilsson, Leutz, and Karlsson 2007). They highlight the issues with parabolic concentrators combined with standard PV, which in turn produce non-uniform radiation on the cells. Three designs are proposed for reflectors that increase the homogeneity of the irradiation. These designs are capable of approaching concentration levels from 2D limit ($1 / \sin \theta_{max}$) to 3D limit ($1 / \sin^2 \theta_{max}$). The proposed designs also break the symmetrical formation of the troughs, which in turn helps in reaching a higher etendue of the existing optical design. An ideal concentrator would have its light rays spread in all directions from its exit aperture. The idea of the proposed designs for collaborating dissimilar angles attempts to solve all the above mentioned issues. These designs have lesser irradiation reaching them, compared to the reference model. The 120º V-shaped reflector has the highest optical efficiency among the proposed designs. In contrast, sinusoidal reflectors have a higher even distribution of rays, and reduced peak thermal nodes over the azimuth angles. The 60º V-shaped reflector has the combined effect of both above mentioned reflectors, but still ranks last in terms of performance. Due to the reduced peak illumination, this system achieved reduced intake of irradiation, which was a major drawback. Nilsson also highlights that its annual data had slightly lower reference than smooth reflectors. However it proved to be effective on net value irradiance distribution, and optical efficiency of 88%.

2.5.2: Fresnel Lens Models

Gonzalez put forth an article about the design and analysis of a curved cylindrical Fresnel lens that can produce high quantity uniform irradiance on the solar cell (González 2009). This paper focuses on the two existing types of Fresnel lens (flat and curved). The performance of a flat lens is not up to par because of the low acceptance angle, and optical efficiency. However, the biggest advantage of these systems is the reduced manufacturing cost. The performance of a curved Fresnel lens is matched with the theoretical maximum limit, and is promising in terms of achieving close to full optical efficiency, neglecting the losses. This is the design adopted by Gonzalez. In the curved lens, the grooves are designed to be finite in size. The surface of the groove design is continuous along the axis, but discontinued along the normal to the surface, hence SMS. The irradiations are most uniform when one point of input rays collected to the solar cell doesn't coincide with another point of input rays, but rather are parallel to one another. This lens design also uses ray tracing techniques to summarize the performance outcome. The disadvantage of the grove design of Fresnel lens is the questionability when accounting for manufacturing limitations, which need to be overcome by further research.

Benitez et al, proposed a Fresnel based PV concentrator with the need to include manufacturing tolerances for mass-production, and manufacturing ease (Benítez et al. 2010). In this proposal, Benitez et al, presented a two stage concentrator, which constitutes of a primary Fresnel lens, and a secondary refractive dome with an independent rotational symmetry.

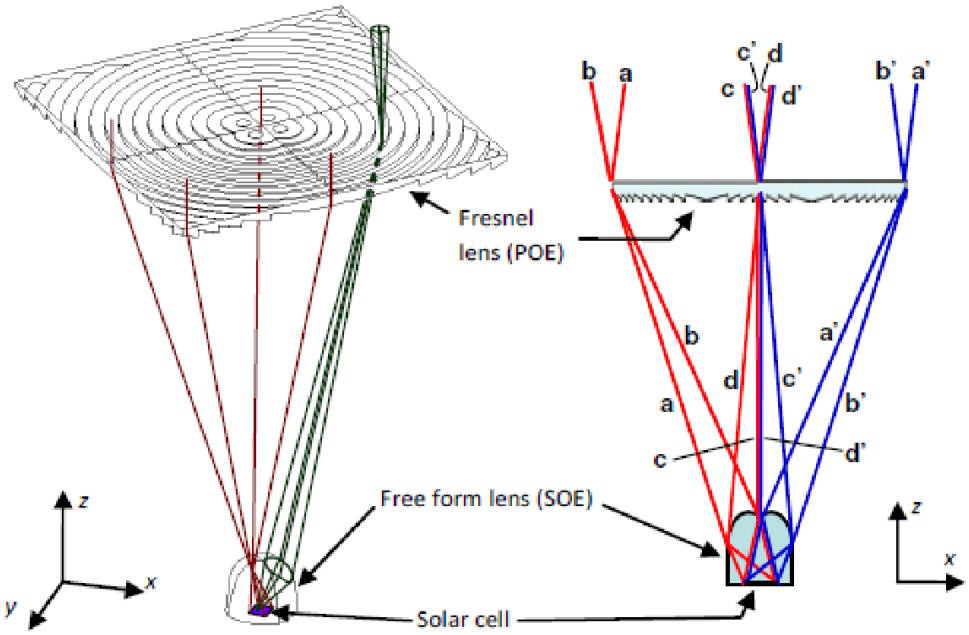

Figure 8: Proposed Fresnel based photovoltaic concentrator (Benítez et al. 2010)

The outcome of the design has both concentrating irradiation (625x) with high acceptance angle, and even distribution of concentrated light using Kohler integration. The Primary Optical Element (POE) used here is a flat Fresnel lens, and a refractive surface, which acted as the Secondary Optical Element (SOE). Manufacturing methods adopted by conventional Fresnel lenses are similar to this Fresnel – Kohler (FK) optical element. The design of this system followed the edge ray theorem of non-imaging optics. In this research, the proposed SOE design is compared with five other conventional SOE designs based on flat Fresnel lens.

The comparison of maximum Concentration Acceptance Product (CAP) between the proposed design and the design of flat Fresnel without SOE showed a significant non-uniformity of focused irradiation (Benítez et al. 2010). Thus CAP is minimalized to reduce

No SOE *Spherical dome* *SILO* *XTP* *RTP* *FK*

peak concentration.

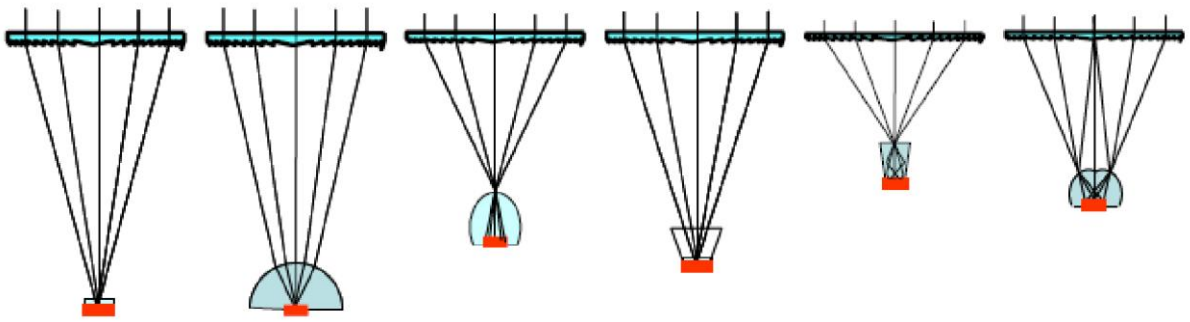

Figure 9: Comparison of Fresnel based concentrator with respect to SOE (Benítez et al. 2010)

The second comparison is between the proposed design, and the flat Fresnel with a hemispherical glass dome, as SOE has shown impact on the optical efficiency due to higher Fresnel reflections. This system proved to be an improvement on a system without SOE. The

third comparison was made with a Single Optical surface (SILO) as the SOE. The SILO design resembled the principles of the Kohler integration, but consisted of a single source against the proposed 4 axis, which reduces the overall output. The fourth comparison was carried out with a hollow-reflective truncated pyramid (XTP), and the fifth with a dielectric- filled truncated pyramid (RTP). The consistency of the coating used in XTP reduced due to TIR resulting in light being trapped between the air and coated surface. This in turn affected the optical efficiency, while the absolute efficiency of RTP design was reduced by 4%. In addition, the comparison made in terms of better irradiance distribution found to have good results with FK concentrators, RTP and SILO, while XTP, spherical dome, and Fresnel designs without SOE has poor homogenization.

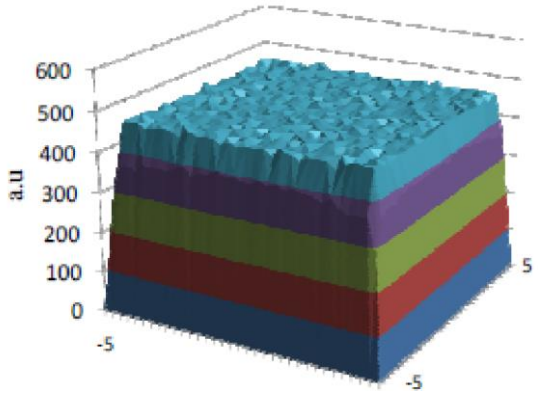

Figure 10: Homogenized irradiation on the solar cell - reduced hotspots (Benítez et al. 2010)

Although the FK concentrator proved to be a more advantageous model in the prior comparison, when competing with higher concentrator designs such as reflection-refraction (XR) PV concentrator (950x), and double reflection-refraction (XXR) Kohler design based on parabolic mirrors (2070x), it failed to outperform due to the saturation point of the concentration factor (Hernández et al. 2007) (Zamora et al. 2009).

Languy et al, presented a paper on flat Fresnel doublets made of poly methyl methacrylate (PMMA), and polycarbonates (PC), which use the technique of combining cost efficient production, and high concentration ratio for their CPV models (Languy et al. 2011). This paper compared singlet, doublet, and hybrid lens designs. These lenses were designed by combining PCs and PMMAs. The study and experiment were focused on linear chromatic aberrations (LCA). The results indicated that the maximum theoretical concentration limit of refractive singlet lens to be around 1000x, while that of hybrid lens to be 5000x, and refractive doublets to be $2e^6$x respectively. The paper also discussed the necessity to reduce the LCA, as it directly affects the concentration factor. It also presented a new achromatization equation against the existing Abbé equation, as Abbé's numbers fail to provide information about the quality of the achromatization. The research paper highlighted that doublets designs are suitable to reach high concentration at low cost.

Pan et al, published an article on the single concentrator to produce an output of high concentration. The single concentrator consists of an arrangement of refractive prisms in a Fresnel lens design (Pan et al. 2011). The pitch of the Fresnel lens focuses solar irradiation on different positions of the receiver, thereby ensuring homogeneity of concentrated solar irradiation.

The two parameters that a concentrator should address are increased concentration ratio, and high acceptance angle. Subsequently, when the above parameters meet, they are accompanied by hot spots, which reduce the output and efficiency. To solve the issue at hand,

Fresnel lens integrated SOE to their existing POE. This added SOE would increase the cell module cost, and increase complexity of the system, which decreases the overall efficiency of the system.

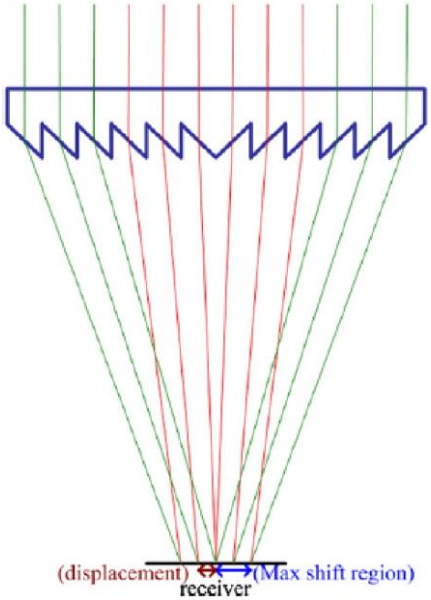

Figure 11: Design based on refractive prisms with homogenized function with varying slopes (Pan et al. 2011)

Pan et al, propose an idea for the development of a Fresnel design, which would meet the required concentration ratio and homogeneity of solar irradiation without the integration of SOE. This paper discussed 3 Fresnel lens designs. The first design used the right edge ray of each pitch to pass the irradiation through the facet, and focused them to the central region of the receiver. The second design used solar rays from the centre portion of the pitch to pass the irradiation, and then focus them to the central region of the receiver. The third design used the left edge ray of each pitch to pass the irradiation through the facet, and focus them to the central region of the receiver (Pan et al. 2011). The advantages and disadvantages of all three designs are studied, and implemented in our proposed design.

The second design mentioned above is taken as the primary model for our proposed design due to its higher acceptance angle. The disadvantage of this model is the presence of hot spots leading to the non-uniformity of concentrated irradiation; thus decreasing the overall efficiency. To overcome this disadvantage, Pan et al proposed a homogenizing function added to the selected model. The incident ray corresponding to the right/left pitch will focus the radiation distribution on the right/left side of the receiver. The distance between the lens and receiver determined the maximum focus of solar irradiation on the receiver. This distance is fixed, and the pitch of the Fresnel lens is altered. The change in pitch was achieved by varying the slope. This helped with the uniformity (14.6 a.u.) of radiation (Pan et al. 2011). Though the uniformity increased, it affected the acceptance angle, reducing it from 0.45° to 0.305° for the proposed system. The disadvantage of the Fresnel designs without SOE is the very low acceptance angle, requiring a precise tracking system to compensate.

Jing et al, put forth the idea of a high performance CPV through the novel design of a compound Fresnel lens (Jing et al. 2012). This design involves two lenses. The primary lens focused irradiation onto the secondary lens through the combination of TIR for the outer saw-teeth ring structure and refraction for the inner saw-teeth ring structure. The secondary lens used refraction to further concentrate the solar rays. Unlike previous designs, the proposed

model had a high acceptance angle and uniform distribution of rays over the solar cells. This paper also highlighted the reduced aspect ratio of the design. To efficiently reduce the design complexity, more than a few rings of primary Fresnel lens concentrate their rays onto a single ring of secondary lens. Further, to increase the optical efficiency, the bottom central part of the secondary lens is designed as a cone-shaped prism.

In the traditional Fresnel lens designs, a high concentration factor is achieved by the enlarged focal length of the CPV, along with their geometrical concentration. This proposed model has an increase in its concentration, not by the enlarged focal length, but rather by the outermost saw-teeth rings of Fresnel lens; these were designed as total internal reflectors. The ratio of focal length to aperture of the lens of the above mentioned system is less than 0.5. A simple trigonometry approach helped determine the critical radius for the outer saw-teeth for TIR. This model is based on the assumption that the sun produces parallel rays. The results are based on the production of a quarter of the design, and through symmetry estimated for half, and then full portion. This system can be further optimized by modifying the design, as the complexity of the centre, and the vertical facet resulted in Fresnel loss.

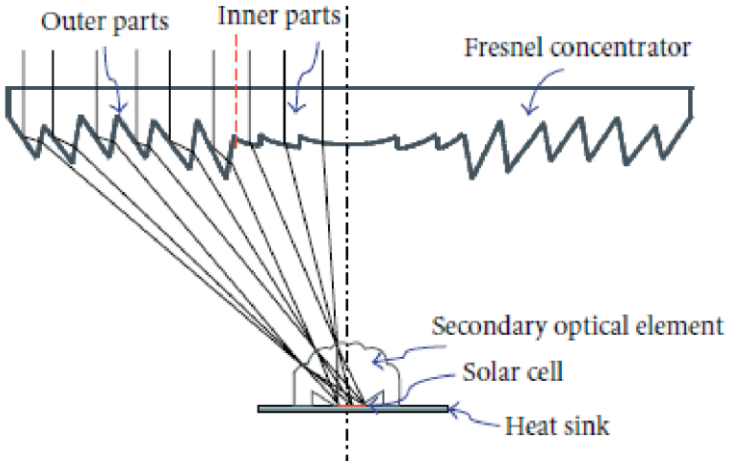

Figure 12: Compound Fresnel design based photovoltaic concentrator (Jing et al. 2012)

The geometrical concentration of the system is higher when compared to the traditional designs with 625x the output, and an optical efficiency of 82%. The acceptance angle of the proposed model is found to be 90% of +/- 1.3°, which outperformed traditional designs with less than +/- 1°. Conventional Systems with secondary lenses perform equivocally to the proposed design in terms of the acceptance angle, however the aspect ratio is more than double the value of the proposed design.

2.5.3: Parabolic Dish Models

Zanganeh et al, proposed a solar parabolic dish concentrator design based on the array of membrane facets (Zanganeh et al. 2012). The membranes are made of polyester mirrors held in place by elliptical rims, and a vacuum is created underneath to forge the optimal focal length needed to concentrate solar rays. The membrane takes up an ellipsoidal profile due to the vacuum created. The axes ratio of each membrane is decided by its position on the dish. These collective membranes converge to take up a paraboloid shape. Monte Carlo ray tracing techniques were used to study the flux distribution, which governed the focal plane of the dish. The deformations on the elastic mirror membrane due to uniform pressure loads were simulated through finite element structural analysis.

According to Zanganeh et al, design change of the large solar concentrators into segmented optic surfaces was preferred over a continuous optics surface, as this was a known method to increase the performance of reflector concentrators.

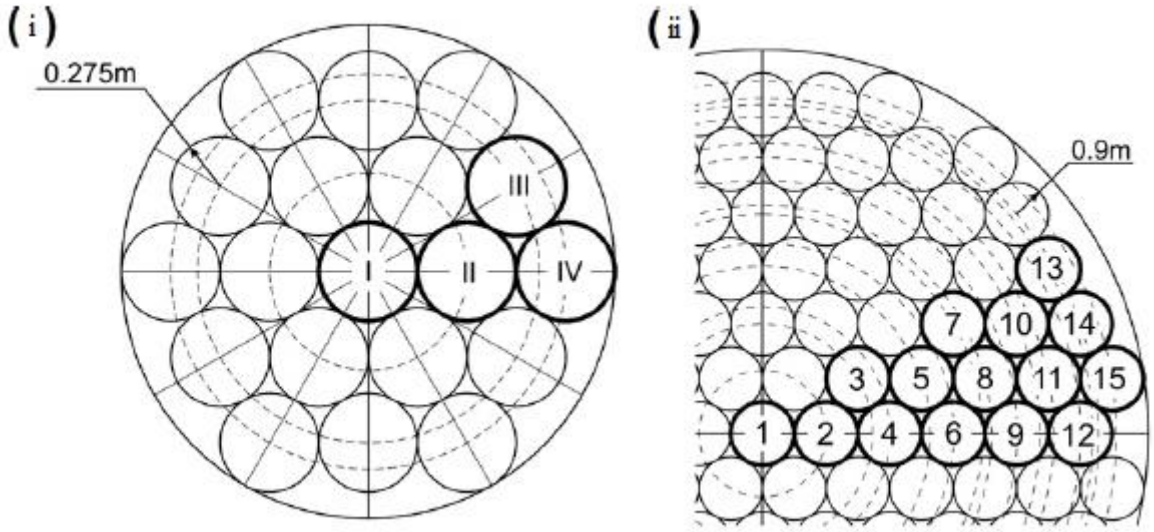

Figure 13: Dish facets proposed by Zanganeh (Zanganeh et al. 2012)

Two geometries were investigated in this paper: (i) small dish with 1.5 m radius, 3m focal length, 19 facets with 4 different mirror membrane facet curvatures and (ii) large dish with 10.m radius, 11m focal length, 121 facets with 15 different facet curvatures. The above designs were compared with the circular rim designs. The mean concentration ratio significantly relied on the radial position, accounting for the off axis aberrations. This investigation suggests that there is a smaller variation in the attainable mean concentration ratio with the increased distance from the parabolic centre for the elliptical design, rather than the circular rim. The large dish elliptical facets design outperforms circular facets when the incident radiation is targeted at 10.4 cm. The captured incident solar radiation is 6.6% higher, and the average concentration ratio is 12% higher.

The small dish captured a 90% incident solar radiation with an output of 28º rim angle, and an average concentration ratio of 1435 suns against the ideal paraboloidal concentrator, which captured 97.4% incident radiation and an average concentration ratio of 2605 suns. The large dish had performed better, as its capacity to capture incident radiation is 90% with a 53º rim angle, and an average concentration ratio of 8199 suns, compared to ideal system of 97% incident solar radiation, and an average concentration ratio of 10,679 suns. The bigger dish performed well with respect to the smaller one due to its higher rim angle, and better dish surface coverage by facets.

Sellami et al, presented a paper on 3D cross compound parabolic concentrators (CCPC) (Sellami and Mallick 2013). This paper had studied the theoretical optical efficiency and flux distribution of the CCPC for various incidence angles of solar radiation. At the PV cell level, it compared the results with 3D CPC. The presented model had an improved geometry, with a concentration ratio of 3.6x of the static concentrator. The static solar concentrators overcame the cost of building integrated photovoltaic (BIPV) by their reduced area of solar cells.

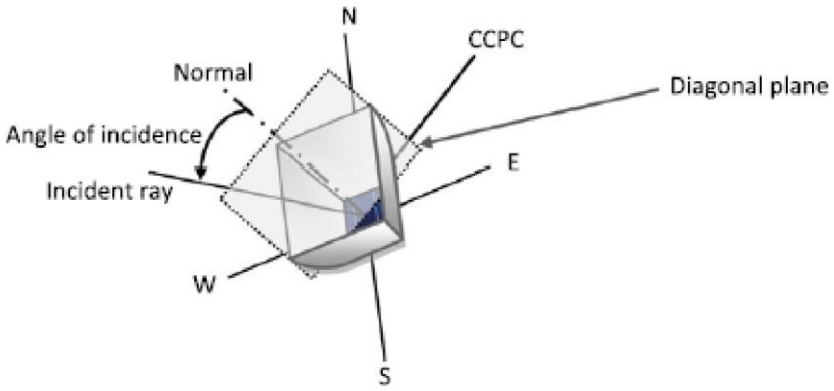

Figure 14: 3D Crossed Compound Parabolic Concentrator (CCPC) (Sellami and Mallick 2013)

The study of the 2D CPC trough revealed a high efficiency because of its solar collection and concentration abilities, however, it is limited by its concentration. The 3D CPC, on the other hand, is an improvement to the 2D CPC. CPC systems are used in second stage concentration. The disadvantage of CPC systems is the profile of their entry and exit aperture through which the solar radiation reaches the solar cell. The circular shape along the aperture incurred losses in the radiation collection. The entry aperture was modified to a hexagonal shape to minimize the loss of solar rays; this in turns led to the compromise of the concentration ratio for the recovered solar rays. The proposed CCPC design solved this issue, as the geometry of the system was designed for a square profile of the collected radiation at the entry and exit aperture.

The CCPC is designed based on 2 requirements, firstly the concentration ratio, and secondly the geometry. 2D CPC forms the basis for 3D CCPC designs. The side profile of 2D CPC is considered for the parabolic profile of a 3D CCPC. These parabolic profiles were translated into the four sides of the 3-D CCPC or via the intersection of two 2D CPCs. The concentration ratio of 3D CCPC is 3.6, compared to that of the 2D CPC, which is 1.9, with an acceptance angle of 30º for both systems (Sellami and Mallick 2013).

The ray trace technique was used to determine the optical performance of the proposed system. The optical efficiency (η_{opt}) is calculated by the total rays reaching the cell, divided by the total radiation incident on the entry aperture. The optical efficiency also accounts for reflectance (ρ) of the material, and the number of reflection (NR_i) undergone by the same ray before it reaches the cell, as well as the number of rays (n).

$$\eta_{opt} = \frac{\sum_{i=1}^{i=n}(\rho^{NR_i})}{number\ of\ incident\ rays\ at\ the\ entry\ aperture} \qquad (2.2)^5$$

The acceptance angle is based on the variation of optical efficiency as a function of incidence angle of solar irradiation (Sellami and Mallick 2013). The reduction in optical efficiency (95% to 50%) indicates that system has approached its maximum acceptance angle (30º). The optical flux distribution highlights the difference in distribution of rays collected at the exit aperture compared to the distribution of rays at the entry aperture. The optical flux of the system is denoted by the quantitative amount of radiation focussed in the same area of the exit aperture. The energy of incident rays takes up the same value of 950 W/m^2. The exit aperture after reflection multiplies this energy value by the optical flux to indicate the energy of the concentrated irradiation.

[5] Sellami and Mallick 2013

The proposed system had a better geometrical concentration than the CPC (3.6x Vs 1.9x). The decrease of concentrated energy at the exit aperture or the non-uniformity of the flux distribution will decrease the overall efficiency of the system. The MATLAB simulated results from this study highlighted the creation of hotspots. However, this was overcome by the reduced space between the conducting fingers, and the back surface field of the cell. Sellami et al, also verified the simulated results experimentally, and found a great accordance between the simulated and experimental values with a minimal error of 12% due to flux distribution patterns.

2.5.4: Hyperbolic Models

Saleh Ali et al, published an article which investigated the optical performance of static 3D solar concentrator in order to find an economical way for potable water production (Saleh Ali et al. 2013). The optical efficiency had a direct correlation with the geometry of the concentrator profile. The concentrator taken into account was an Elliptical Hyperboloid Concentrator (EHC). Optical efficiency was calculated by the aid of ray tracing, which was done through the OpticWorks software. The performance of the elliptical profile was studied for different aspect ratios to determine the most suitable one. Parameters such as, concentration ratio, and optical efficiency were evaluated for chosen elliptical ratios. The overall performance of EHC was assessed based on the acceptance angle, concentration ratio, and optical efficiency. Net flux distribution on the receiver was also presented for various concentrator heights.

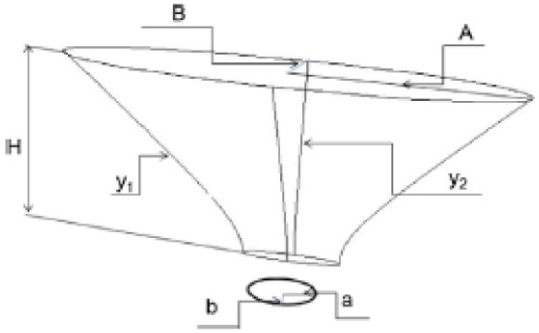

Figure 15: 3D Elliptical Hyperboloid Concentrator (EHC)
(Saleh Ali et al. 2013)

In the field of non-imaging optics, the system components are designed to collect solar rays rather than to mirror them. CPC systems are widely designed as non-imaging optic concentrators. Design techniques such as Flow-line methods were extensively used to investigate the performance of 3D CPCs and their variations. Other researchers have found that the reflective concentrators outperformed 3D CPC. This led to an investigation of 3D CPC by flow-line, which gave rise to a family of higher order concentrators, such as Hyper-Parabolic concentrators (HPC). Apart from this, photometric field theory, and ray bundle methods were used to research asymmetric concentrators.

Hyperbolic concentrators matched the ideal 3D asymmetric concentrator. The flow line technique of an elliptical disk indicated no disruption in the shape of the concentrator. The hyperboloid profile showed an increased performance in terms of acceptance angle, and collection of solar rays. The 3D concentrator, which is classified under the non-imaging optic design, had the ability to concentrate all of the incoming solar irradiation. This led to the investigation of Square Elliptical Hyperboloid (SEH), which consists of a hyperbolic profile, an elliptical aperture for incoming rays, and a square profile for exit rays, with a high acceptance angle of 120º. However, the concentration ratio was limited to 4x, due to its

geometric profile. This paper focused on the development of the 3D solar thermal concentrator design, which would be enhanced in their optical efficiency, concentration ratio, and acceptance angle. An EHC design was studied, and documented using ray tracing techniques based on the findings of various concentrator profiles that have been discussed.

The concentration for various aspect ratios increased as the height of the concentrator increased at the expense of the acceptance angle. The optimal aspect ratio value was found to be 5. At an aspect ratio of 5, the optical efficiency was found to increase by three folds as the entry aperture shifted from a circular profile to an elliptical profile. The optical efficiency reached 27% with a concentration ratio at 20, concentrator height at 0.4m, and half-acceptance angle at 30º. Truncation has been carried out to minimize the material used by the system. The effect of truncation directly affects the concentration ratio.

2.5.5: Paraboloidal Models

Canavarro et al, put forth their idea of new second stage concentrators in the field of Concentrated Solar Power (CSP) technology (Canavarro, Chaves, and Collares-Pereira 2014). PT concentrators have dominated this field, and have faced many challenges in reducing costs, while bettering their performance. This paper explored the use of second stage concentration combined with the trough design, which had a higher concentration, and a larger acceptance angle. The optic principle behind the proposed idea was double reflection simultaneous multiple surface (XX SMS). The primary surface was approximately parabolic. Significant Fresnel loss reduction was achieved by means of the approximate parabolic design. Comparisons on the proposed model were made between SMS Helmet concentrators and commercial PT concentrators.

The PT concentrator largely depended on the rim angle of the primary reflector for achieving maximum concentration. The half- acceptance angle of the system is defined by $\theta_{h,PT,}$ the concentration of the PT concentrator is defined as C_{PT}. The angular spread of sun was taken to be 0.26º, which would result in a maximum concentration of 70x, even with a maximum rim angle ($\varphi_{PT} = 90º$).

$$C_{PT} = \frac{sin\varphi_{PT}}{\pi \, sin \, \theta_{PT}} \qquad (2.3)^6$$

The proposed system did not depend on the rim angle of the system, and the elimination of $1/\pi$ factor accounted to a maximum concentration limit of 213x (Canavarro, Chaves, and Collares-Pereira 2013). This gave space to improve the existing system. To increase the productivity of the PT system, the aperture area was increased, which in turn required a higher diameter for the receiver tubes.

$$C_{XX\,SMS} = \frac{1}{sin \, \theta_{XX\,SMS}} \qquad (2.4)^6$$

The receiver incurred more conduction or convection loss if immersed in air. To eliminate this obstacle, this system had its receiver enclosed in glass to create a vacuum. This established a system with very low heat loss coefficient.

Earlier SMS concentrators, such as asymmetric secondary optic reflector systems (Snail concentrator), and symmetric secondary optic reflector system (Helmet concentrator) were proposed to increase the concentration factor as an alternative for PT concentrator. The inclusion and exclusion of the glass envelop created shortcomings to the output with respect to

[6] Canavarro, Chaves, and Collares-Pereira 2014

each scenario. Consider the Helmet concentrator (as shown below), where the edge ray clearly indicates the light passed through the glass envelope multiple times before it reached the receiver. This created transmission loss (Fresnel loss at the entry-exit of glass envelope; reflection loss at the secondary reflector). In order to overcome this obstacle, the system was designed without the glass envelope, however the receiver was subjected to loss, due to conduction and convection, resulting in reduced efficiency.

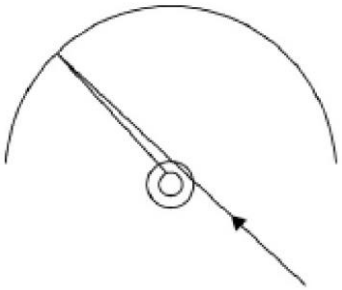

Figure 16: Schematic representation of helmet concentrator with Fresnel and reflection losses (Canavarro, Chaves, and Collares-Pereira 2014)

The proposed system overcame these shortcomings by way of a redesigned secondary reflector. It avoided the transmission losses, which paved the way to include evacuated tubes.

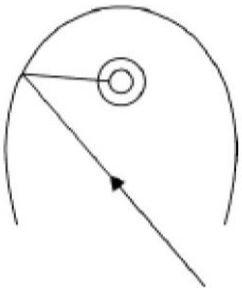

Figure 17: Schematic representation of edge rays: XX SMS concentrator (Canavarro, Chaves, and Collares-Pereira 2014)

Another short coming faced by the PT concentrator was that the centre of mass of the system was located at the lower portion, closer to the primary reflectors. In order to bring the G_c of the system closer to the receiver tubes, the primary reflectors needed to extend beyond a 90º of rim angle. The change facilitated the tracking axis aligned with the system. It also affects the aperture of the system and CAP. The proposed new design rectified the obstacles as the secondary reflector surface brought the G_c position closer to the receiver tubes.

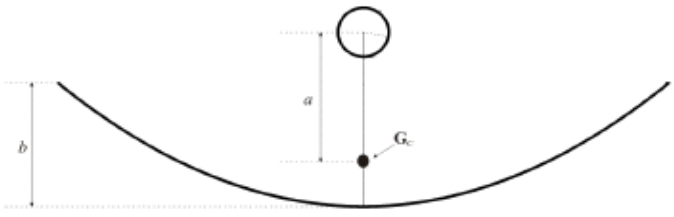

Figure 18: PT concentrator with centre of mass Gc (Canavarro, Chaves, and Collares-Pereira 2014)

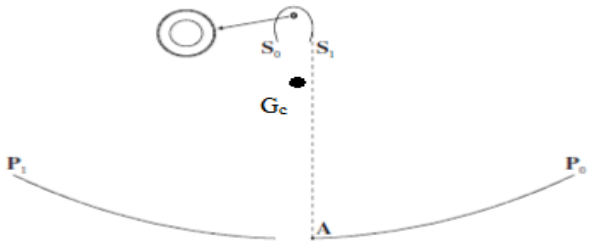

Figure 19: XX SMS concentrator with centre of mass Gc (Canavarro, Chaves, and Collares-Pereira 2013)

The performance of the XX SMS concentrator was higher with a CAP of 0.61 against 0.32 for PT concentrators. This was backed by the fact that concentration doubled for XX SMS concentrators for the same acceptance angle. The optical efficiency was reduced for XX SMS concentrators as the focused light underwent one more reflection before it reached the receiver, while the solar rays reached the receiver directly from the primary reflector in PT concentrators. Although the optical efficiency, and aspect ratio of the PT system was better, the XX SMS optic delivers 1.71x more solar radiation to the receiver. The XX SMS concentrator also outperformed the Helmet concentrators in terms of efficiency and CAP for the same acceptance angle.

2.5.6: Hybrid Fresnel Models

Zhuang et al, proposed a novel hybrid Fresnel based concentrator without the aid of SOE (Zhuang and Yu 2014). This design had a higher uniformity in terms of irradiance spread on the solar cell. The absence of SOE eliminates the Fresnel losses, which decreases the efficiency. The hybrid design consisted of two parts; the inner region was designed using a conventional Fresnel lens, while the outer region used the Double Total Internal Reflection (DTIR) lens. The prism-like structure used in the Fresnel lens design adopted a simpler algorithm to focus irradiation for uniformity. The prism displacements were optimized and different prism focuses were used on different positions.

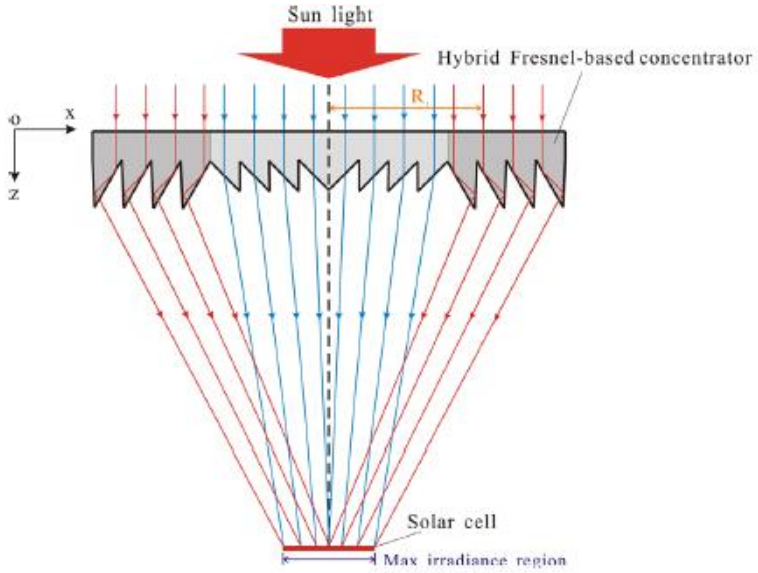

Figure 20: Proposed novel hybrid Fresnel based concentrator (Zhuang and Yu 2014)

Research work published by Pan et al had formed the basis for this design. The proposed design in this paper focused on methodology with reduced Fresnel losses and high concentration ratio. Initial design was based on geometric relation and segment method was used to enforce the profile for the concentrator. To optimize the design further, focus displacement approach was used to bring uniformity in focused irradiation on the multi junction solar cell. This proposed design also had a good acceptance angle, which helped to reach higher efficiency.

The proposed design had a higher CR with 1760x compared to 1018x of traditional designs. The aspect ratio of the system was lower (f-number: 0.59 improved; 1.00 traditional), hence stability of the proposed system was more. The slight disadvantage of the proposed system was uniformity (improved design – 84%; traditional design - 86%) and half acceptance angle (improved design – 0.23º; traditional design – 0.305º) were slightly lower compared to conventional design.

2.6: Multi Junction Solar Cell

The existing PV modules have plateaued in potential, as such, there is a need to look for alternative methods to improve energy conversion efficiently. The development of high-performance solar cells offered a potential to achieve high power per unit cost (Yamaguchi and Araki 2019). The price of Si based PV modules have saturated, while those of MJSC have a higher prospective for price cut. The potential price reduction stems from using a similar fabrication techniques used as the LED industry. The LED manufacturing industries can be retrofitted with CPV cells, which would drive the price lower. The MJSC also needs more than 1 sun to increase power output, which is supported by the optics discussed earlier. The MJSC has numerous advantages and disadvantages, which are discussed below.

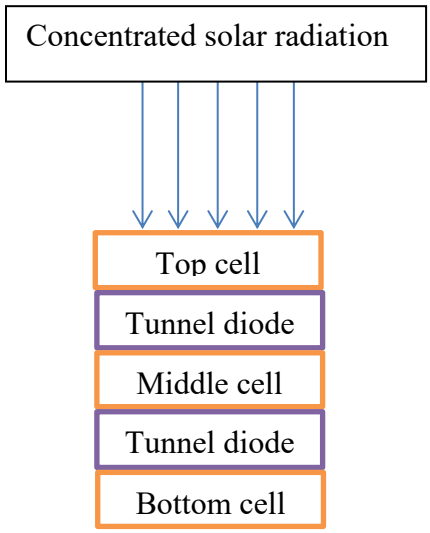

Figure 21: Schematic representation of triple junction solar cell

A MJSC is a quantum solar converters, which possess two or more sub-cells. These cells are made of semiconductor materials with different band gaps. The basic operation of a MJSC is to improve the solar conversion efficiency. The key to achieve high efficiency is to convert as much energy photons in the solar spectrum into electrical energy as possible (Philipps and Bett 2014). In a conventional single junction solar cell, only a part of the solar spectrum is converted, which can be identified by the bandgap. A semiconductor material, which can be identified by the same bandgap can replace the conventional cell. With

conventional cells, the photons with energy levels below the bandgap are unable to be absorbed, and are lost due to transmission. On the other hand, energy levels above the bandgap are well absorbed, but lost due to the thermalization process. The idea behind MJSC is to stack 2 or more sub-cells with increasing bandgap on top of each other in order to utilise a larger part of the solar spectrum, and reduce transmission and thermalization losses (Philipps and Bett 2014).

2.6.1: History of Multi Junction Solar Cell

The need to power satellites led to the birth of solar cells in the year 1958 (Fernández, García-Loureiro, and Smestad 2015). Since then, it has become an integral part of everyday life. There has been a continuous development in solar cells starting from silicon (Si) cells, which have a 10% efficiency, to tandem cells, which has reached almost 50% efficiency (Andreev 2018). These tandem or MJSC cells have been researched since 1960. Computer analyses were used to study, and improve the performance of tandem cells as early as 1982. One of the earliest tandem cells designed was the AlGaAs/GaAs tandem cell (Yamaguchi and Araki 2019). This design faced obstacles such as an unstable tunnel junction, which was later rectified with the introduction of a double hetero structure for the tunnel junction. These hetero structures were produced by the MOCVD (metal organic chemical vapour deposition) technique.

2.6.2: Fabrication Process of Multi Junction Solar Cell

There are various steps involved in the manufacturing process of a MJSC. Theoretical calculations are done for the selection of an optimal band combination. Based on the combinations, corresponding materials are selected. Lastly the architecture of the solar cell is established. Although there are a variety of materials to choose from, the property and availability of the material restricts the choice. The bandgap based selection of materials is a function of the lattice constant, implying that a chosen material needs to be lattice matched in order to have a high efficiency. Based on this fabrication process, the triple junction solar cell made of GaInP/GaInAs/Ge meets all necessary requirements (Fernández, García-Loureiro, and Smestad 2015).

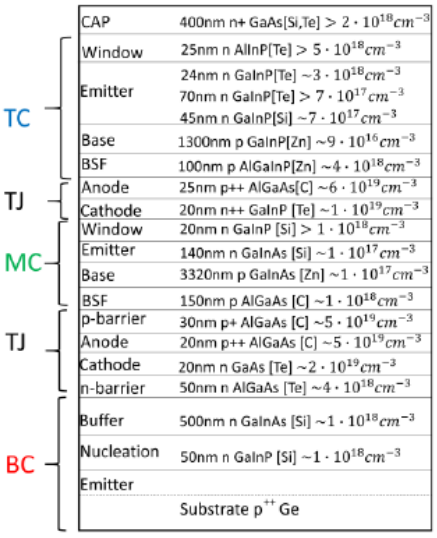

Figure 22: Semiconductor structure of GaInP/GaInAs/Ge
BC – bottom cell, MC – middle cell, TC – topcell, TJ – tunnel junction
(Barrutia et al. 2018)

This MJSC is fabricated through the MOVPE (metal organic vapour phase epitaxy) method, with Ge acting as the substrate. This architectural arrangement of sub-cells reduces the thermalization losses. The current flow of the entire cell is limited to the sub-cell, which generates the least current. The problem associated with this solar cell is the need to fabricate the cell with different materials of differing lattice constants to achieve an overall system efficiency. The voltage performance of each sub-cell is 1.88 eV (GaInP), 1.41eV (GaInAs), and 0.67eV (Ge). This lattice matched setup isn't effective, due to the high amount of photons incident on Ge bottom cell. This affects the I-V characteristics of the MJSC. The amount of voltage generated is higher in the other 2 sub-cells when compared to that of Ge. Manufacturing limitations result in 1-2% mismatch in the lattice constant between sub-cells, resulting in excess current built up on the bottom cell.

To avoid the above mentioned issues, a metamorphic arrangement of sub–cell architecture is preferred, where the system is built with lattice mismatch containing buffer layers to link the sub-cells. The fabrication process of lattice matched, or metamorphic arrangement of sub-cells is a single process. Hence, there exists various method to overcome this difficulty. One such method which can overcome both the issues mentioned is the inverted-metamorphic. In this technique, the solar cell is fabricated in the inverse order on the suitable substrate, which is later removed and replaced by a front metallic contact. Another such technique is one where the sub-cells are mechanically stacking after being grown separately. The shortcoming of this method is the complexity involved in the fabrication and assembly of sub-cells, which in turn affects the cost of the system. There is also the wafer bonding technique, where semiconductor materials are combined with different lattice constants by forming semiconductor bonds at the common interface layer (Fernández, García-Loureiro, and Smestad 2015).

2.6.3: Characteristics Determination of Multi Junction Solar Cell

Various parameters need to be established for the research work intended in this thesis. The effect of concentrated solar radiation on the tandem cells with respect to its performance is vital in determining the output of the solar cell.

The open circuit voltage tends to increase with the increase of sun concentration levels, and decrease with an increase in cell temperature. The temperature coefficient of various semi-conductors influences the performance of the system. Ge sub cells have lesser output in terms of open circuit voltage when compared to InGaP or InGaAs. At a higher concentration, the Ge sub cell can withstand temperatures of up to 200°, and cease to operate at 120° for one sun concentration (Nishioka et al. 2005). For a concentration ratio of 70, it can function at 190 °.

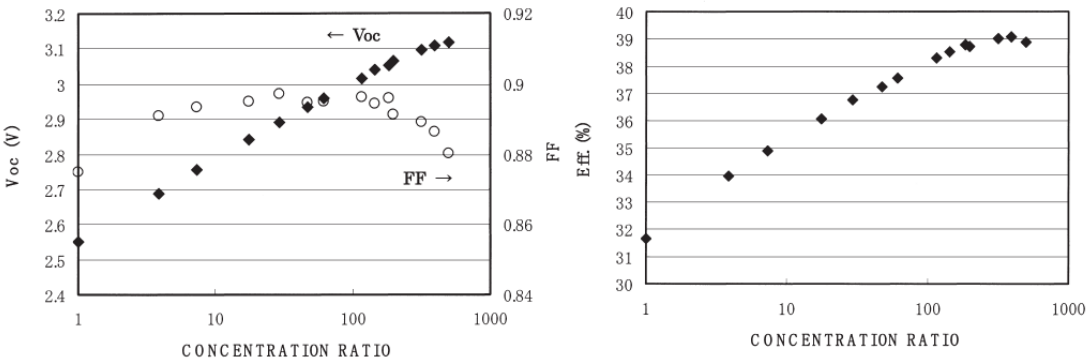

Figure 23: Voltage and efficiency characteristics of GaInP/GaInAs/Ge (Takamoto et al. 2005)

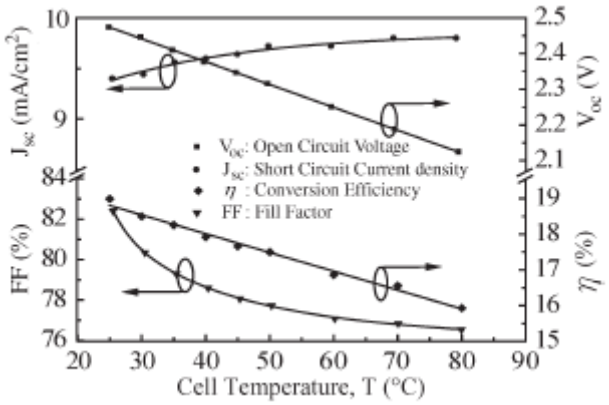

Figure 24: Temperature dependence of principle photovoltaic parameters for GaInP/GaInAs/Ge (Yang et al. 2011)

The current increases marginally with increase in temperature, and eventually saturates. The increase in current has minimal benefit on the output of the solar cell. However, fill factor is reduced due to the increase in temperature. The effect of increase in temperature influences the overall efficiency of the solar cell, which is indicated by a drop in temperature coefficient 0.053%/°C. For a solar cell at a standard operating condition of 25°C under illumination, there is almost a 50% jump on the forward voltage. As the cell temperature increases, the forward voltage drops by 6% before it saturates at 48°C. This indicates the need for further research of the above work with respect to solar concentration.

2.6.4: Selection of Multi Junction Solar Cell

It is established that the current generated in the MJSC with a Ge bottom cell is high, and lost due to the series connection. Further research in this domain has led to the creation of many similar variants, such as, InGaP/GaAs/InGaAs and GaInP/GaAs/Si, each with differing advantages. The replacement of the Ge cell with InGaAs proved to be beneficial as the voltage rating of latter cell is 1eV, thus improving on the output of the solar cell.

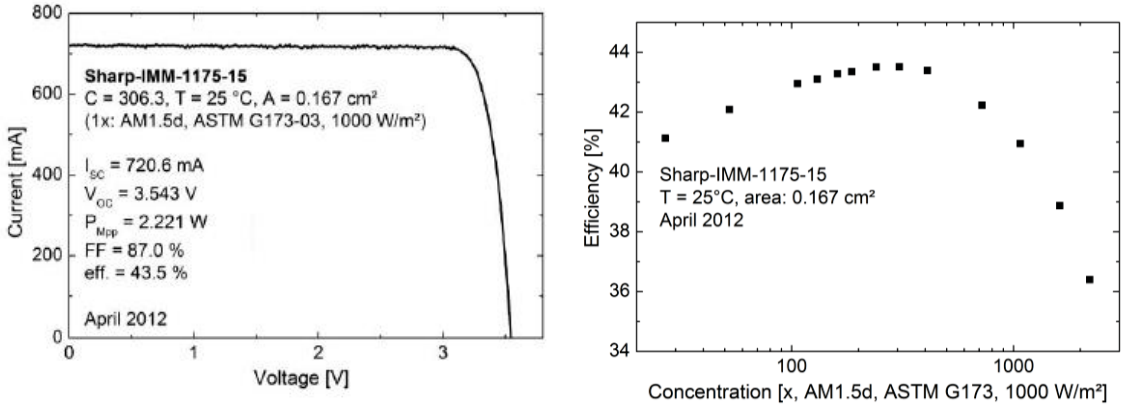

Figure 25: I-V and concentration characteristics of InGaP/GaAs/InGaAs (Sasaki et al. 2013)

Despite the advantages, all sub cells made of semiconductors are expensive. To reduce the unit price of a MJSC, the top and middle sub-cell is grown on a Si substrate through mechanical staking or the wafer bonding technique.

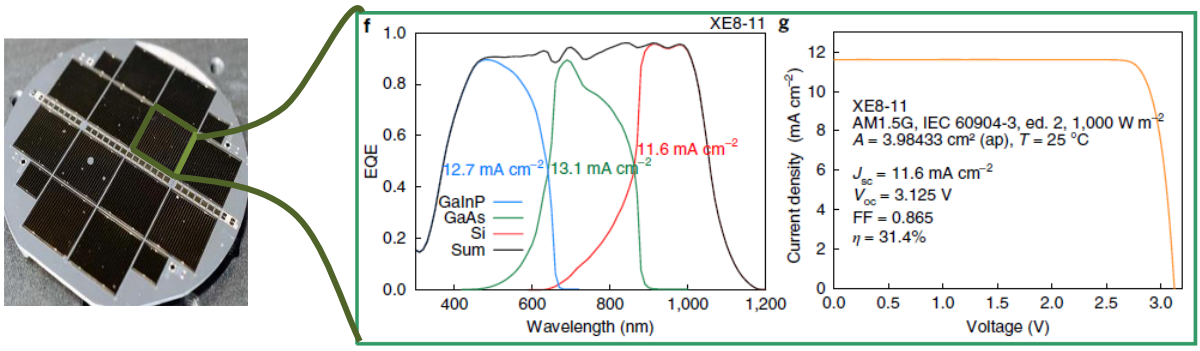

Figure 26: Performance of GaInP/GaAs//Si (Cariou et al. 2018)

Although the MJSC with InGaAs has higher efficiency, given that Si is available in abundant compared to Ge cells or InGaAs, MJSC with Si cell is preferred due its economic advantage. Another advantage of selecting a Si MJSC for this design, is it's the optimal cell size. All other designs have a cell size of less than 1cm^2 while the Si based design has a cell size of 4 cm^2, which proves to be more advantageous in our design.

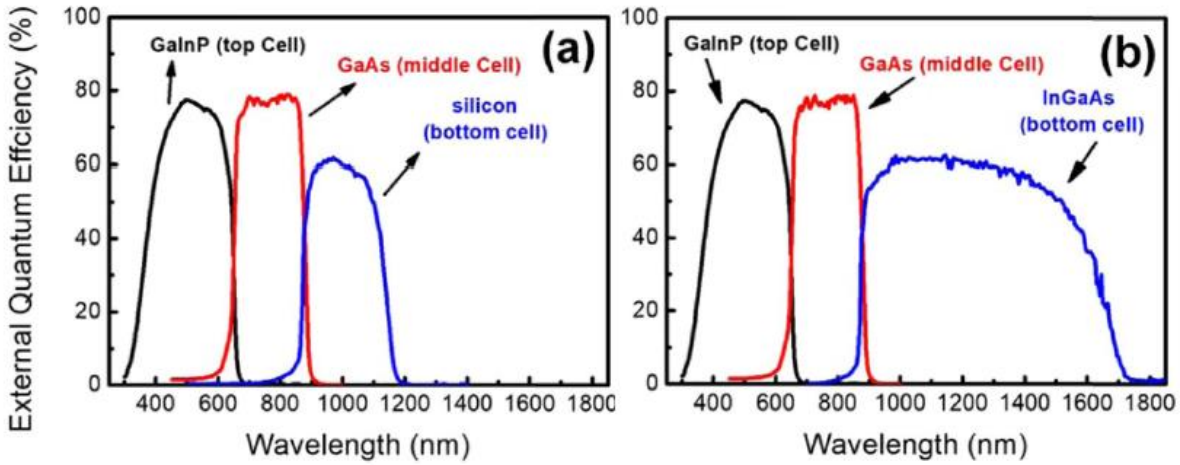

Figure 27: Performance comparison of GaInP/GaAs//Si vs GaInP/GaAs/ InGaAs (Kao et al. 2019)

2.7: Tracking System

The working principle of the proposed system is to concentrate solar radiation onto the receiver at all times. In order to capture the insolation, the proposed system should deploy a tracking system to assist in the process. Many tracking system have been developed along the line of solar technology. This system requires a dual axis tracking system. There are two kinds of tracking systems, namely the tip-tilt dual-axis tracker (TTDAT) and azimuth-altitude dual-axis tracker (AADAT). The former one holds the system in the centre and rotates along the pole, while the latter one uses a ring mounted on the floor with the help of rollers to change the direction. For our proposed system, the AADAT would provide better stability as the tracking system needs to be of medium precision. This is necessary, as the deviation from the sun alignment angle by 1° results in the loss of 10% solar insolation on the surface and 22% for a 2° deviation.

3. Mathematical Modelling of Reflectors:

3.1: Introduction

The modelling of solar rays from the origin of the sun, through reflectors, to its final destination point is achieved through ray tracing. The directions of these rays are studied through vector analysis, and helps establish the bases required to understand the proposed CPV system. The proposed system is a reflector based concentrator, therefore a few assumptions are made. For simplicity, the system is designed without the refraction or absorptance elements, and the path of the rays is governed by Fermat's Principe of Least Time. The system is modelled in order to establish various parameters of our proposed system. For the purpose of mathematical modelling, we need to understand some basic equations

3.2: Components of Ray Tracing

In order to ray trace, the rays of solar irradiation are represented using vectors. The parametric representation of the ray is given by a point A (x_1, y_1, z_1) on the line, with a known vector $\vec{q}$ (q_x, q_y, q_z), which lies parallel to the ray line mentioned above. The ray reaches the reflector surface on the same plane (*yz plane)* at point B (x_2, y_2, z_2). The line which connects the points A and B is called a directed line segment, otherwise known as a displacement vector. This line segment is represented as $\overrightarrow{AB}$ which equals the scalar multiple of $\vec{q}$ as per the vector law of addition.

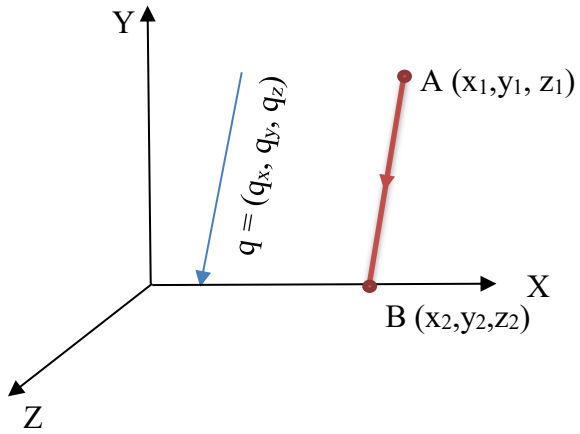

Figure 28: Equation of solar ray $\overrightarrow{AB}$ in terms of known $\vec{q}$

$$\overrightarrow{AB} = s\,\vec{q} \qquad (3.1)^7$$

The vector $\overrightarrow{AB}$ can also be represented by its parametric counterpart

$$[x_2 - x_1\,,\, y_2 - y_1\,,\, z_2 - z_1] = s\,\vec{q}$$

Resolving their components along x, y, and z direction

$$\left.\begin{aligned} x_2 - x_1 &= (s)(q_x) \\ y_2 - y_1 &= (s)(q_y) \\ z_2 - z_1 &= (s)(q_z) \end{aligned}\right\} \qquad (3.2)^8$$

[7] Thomas 2013
[8] Feldman 2011

The dot product of any two non-zero vectors, which are orthogonal to each other will always result in zero. The $\vec{n}$ (n_x, n_y, n_z) represented in the drawing is the normal unit vector.

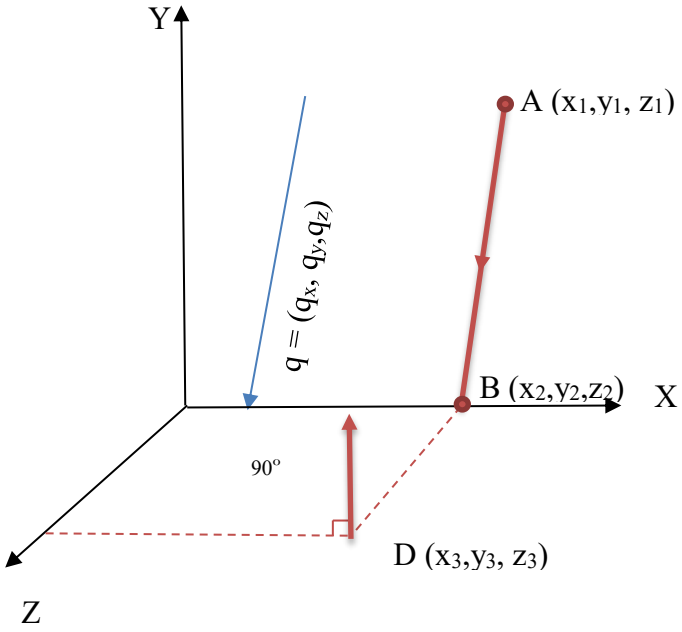

Figure 29: Equation of solar ray $\overrightarrow{AB}$ with respect to $\vec{n}$

$$(\overrightarrow{BD}) \cdot \vec{n} = 0 \qquad (3.3)^{8}$$

The parametric form of $\overrightarrow{BD}$ and $\vec{n}$ are represented as

$$[x_3 - x_2 , y_3 - y_2 , z_3 - z_2] \cdot \vec{n} = 0$$

$$[x_3 - x_2 , y_3 - y_2 , z_3 - z_2] \cdot [n_x , n_y , n_z] = 0$$

$$n_x (x_3 - x_2) + n_y (y_3 - y_2) + n_z (z_3 - z_2) = 0$$

$$n_x x_3 + n_y y_3 + n_z z_3 = n_x x_2 + n_y y_2 + n_z z_2 \qquad (3.4)$$

Substituting equation *(3.2)* in *(3.4),* we get

$$n_x x_3 + n_y y_3 + n_z z_3 = n_x \{x_1 + (s)(q_x)\} + n_y \{y_1 + (s)(q_y)\} + n_z \{z_1 + (s)(q_z)\}$$

$$n_x (x_3 - x_1) + n_y (y_3 - y_1) + n_z (z_3 - z_1) = (s) \{n_x q_x + n_y q_y + n_z q_z\}$$

$$s = \frac{n_x(x_3 - x_1) + n_y(y_3 - y_1) + n_z(z_3 - z_1)}{n_x q_x + n_y q_y + n_z q_z} \qquad (3.5)$$

The above equation dictates the scalar value of the ray, which is incident from the sun. According to the laws of reflection, these ray traces follow a specular reflection due to the polished surface finish of reflectors. These surfaces possess reflectance, which has a close approximation of mirror reflection, and reflected rays are along the same plane as their incident light rays. The incident and reflected ray are equal with respect to the normal vector acting perpendicular to the plane on which the reflection takes place, while the direction n of vectors

[8] Feldman 2011

of all these rays is coplanar. The displacement vector $\overrightarrow{AB}$ is incident along the – *yz* plane and reflected onto the *yz* plane with normal vector perpendicular to *x* axis.

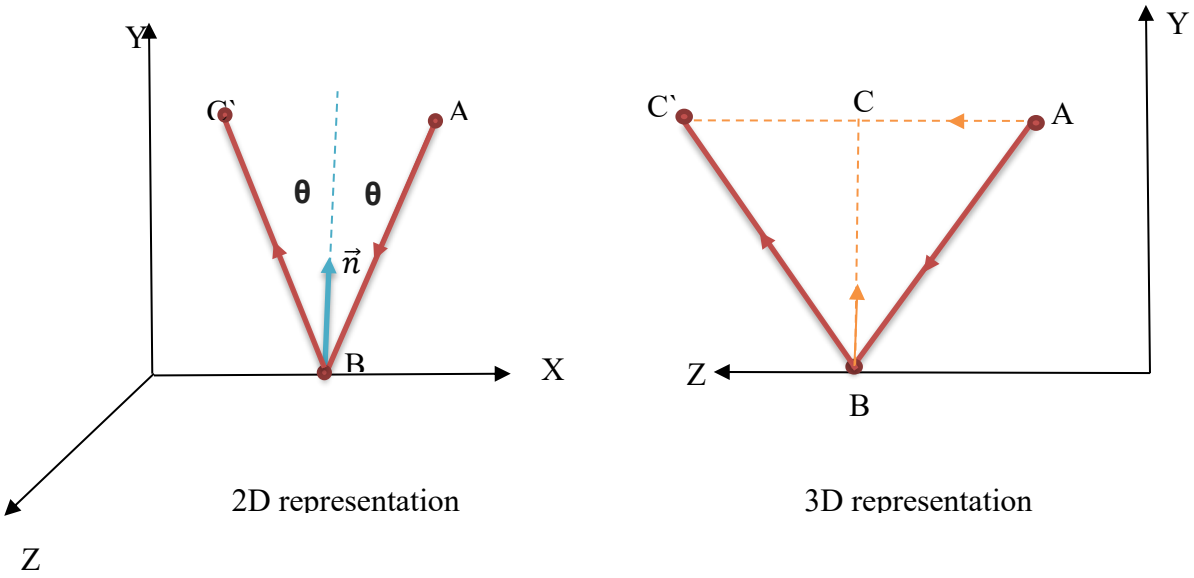

Figure 30: Vector representation of incident and reflected ray

According to triangle law of vector addition

$$\overrightarrow{AB} + \overrightarrow{BC} = \overrightarrow{AC}$$

$$\overrightarrow{BC} + \overrightarrow{CC'} = \overrightarrow{BC'}$$

In other words $\overrightarrow{AB}$ represents the incident ray ($\vec{\imath}$) and $\overrightarrow{BC'}$ represents the reflected ray ($\vec{r}$) and $\overrightarrow{AC}$ equals $\overrightarrow{CC'}$

$$\left.\begin{aligned} \vec{\imath} + \overrightarrow{BC} &= \overrightarrow{AC} \\ \overrightarrow{BC} + \overrightarrow{AC} &= \vec{r} \end{aligned}\right\} \quad (3.6)$$

The projection of $\overrightarrow{AB}$ on $\overrightarrow{BC}$ can be represented as below, as the magnitude of $\overrightarrow{BC}$ is the dot product of incident ray and normal vector

$$\overrightarrow{BC} = (\vec{\imath} \,.\, \hat{n})\, \hat{n} \quad (3.7)^{8}$$

Replace $\overrightarrow{BC}$ vector from *(3.7)* in *(3.6)*

$$\vec{\imath} = \overrightarrow{AC} - \overrightarrow{BC} = \overrightarrow{AC} - (\vec{\imath} \,.\, \hat{n})\, \hat{n} \quad (3.8)$$

$$\vec{r'} = \overrightarrow{AC} + \overrightarrow{BC} = \overrightarrow{AC} + (\vec{\imath} \,.\, \hat{n})\, \hat{n} \quad (3.9)$$

Equating *(3.8)* in *(3.9)*

$$\vec{r} = \vec{\imath} - 2\,(\vec{\imath} \,.\, \hat{n})\, \hat{n}$$

$$\overrightarrow{BC'} = \overrightarrow{AB} - 2\,(\overrightarrow{AB} \,.\, \hat{n})\, \hat{n} \quad (3.10)^{9}$$

[8] Feldman 2011
[9] de Greve 2006

As discussed earlier, the curvature profile of a single mirror is considered as either circular or parabolic. A single ray of solar insolation is traced through the mathematical equation. This equation is applied to the entire mirror surface and further integrated to the rest of the mirrors found on the base. The mathematical equation of a traced ray gives the focal distance and the position of the reflected ray with respect to its curvature.

3.3: Hemispherical Reflection Model

The hemispherical model is made of a circular cross section along the 2D plane which is revolved about y axis. An assumption is made that the solar ray incident on the curved surface of the model is parallel to y axis. The vector denoting all these rays can be assumed to be one and the same as the ray which represents the along the y-axis. For better understanding of the ray trace, only 2d model of the system is considered. Vector equation of line parallel to y axis is denoted by *(0, -p_1)*.

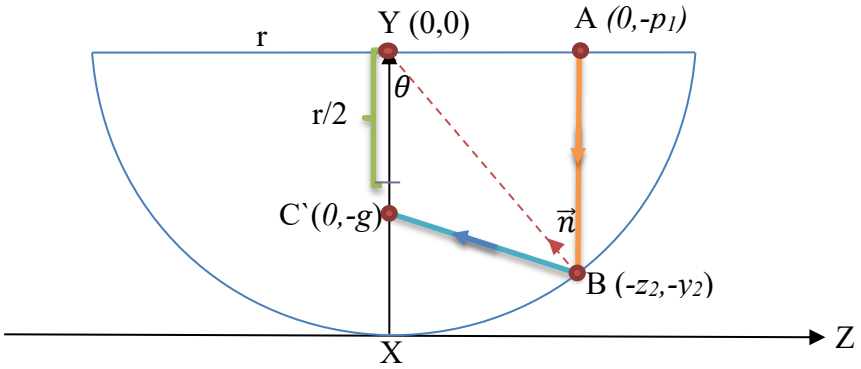

Figure 31: Specular reflection of solar ray $\overrightarrow{AB}$ by a spherical surface (Pereira, Fernandes, and Guerra Rosa 2019)

The incident rays are reflected at B *(z_2, y_2)* and converge at C' *(z_3, y_3)*, which can also be represented as *(0, -g)* as it is known that the circular profile converges the reflected rays at its focal point.

Substituting equation *(3.1)* and *(3.2)* to the hemispherical model

$$(0\ ,-g) = (-z_2\ ,-\ y_2) + s\ \overrightarrow{BC'} \qquad (3.11)$$

Bringing equation *(3.10)* to the hemispherical model

$$\overrightarrow{BC'} = \overrightarrow{AB} - 2\ (\overrightarrow{AB}\ .\ \vec{n}\ )\ \vec{n} \qquad (3.12)$$

$\overrightarrow{AB}$ is parallel to *y axis* making its vector point *(0 , -p_1)*.

To determine the unit normal vector to a circle

Equation of circle: $z^2+y^2 = r^2$

$$F(z , y) = z^2+y^2 - r^2= 0$$

$$F(z) = 2z;\ F(y) = 2y$$

$$\vec{n} = \frac{\nabla F}{\| \nabla F \|}$$

$$\vec{n} = \frac{(2z , 2y)}{\sqrt{(2z)^2 + (2y)^2}}$$

$$\vec{n} = \frac{(2z , 2y)}{\sqrt{4(z^2 + y^2)}}$$

$$\vec{n} = \frac{z}{r} , \frac{y}{r} \qquad (3.13)^{10}$$

Substituting equation *(3.13)* in equation *(3.12)*

$$\overrightarrow{BC'} = (0, -p_1) - 2\{(0, -p_1) . (- \tfrac{z_2}{r} , - \tfrac{y_2}{r})\} (- \tfrac{z_2}{r} , - \tfrac{y_2}{r}) \qquad (3.14)$$

Substituting equation *(3.14)* in equation *(3.11)*

$$(0 , -g) = (-z_2 ,- y_2) + s [(0, -p_1) - 2\{(0, -p_1) . (- \tfrac{z_2}{r} , - \tfrac{y_2}{r})\} (- \tfrac{z_2}{r} , - \tfrac{y_2}{r})]$$

$$(0 , -g) = (-z_2 ,- y_2) + [s\ (0, -p_1) - 2\ s\ \{(0, -p_1) . (- \tfrac{z_2}{r} , - \tfrac{y_2}{r})\} (- \tfrac{z_2}{r} , - \tfrac{y_2}{r})]$$

$$(0 , -g) = (-z_2 , -y_2) + s\ (0, -p_1) - 2\ s\ (\tfrac{p_1 y_2}{r}) (- \tfrac{z_2}{r} , - \tfrac{y_2}{r}) \qquad (3.15)$$

Equating *z axis* and *y axis* with its respective components

$$z\ axis : 0 = -z_2 + s\ (0) + 2sp_1 \frac{z_2 y_2}{r^2}$$

$$s = \frac{r^2}{2y_2 p_1} \qquad (3.16)$$

$$y\ axis : -g = -y_2 - s\ (p_1) + 2sp_1 \frac{{y_2}^2}{r^2} \qquad (3.17)$$

Substituting equation *(3.16)* in equation *(3.17)*

$$-g = -y_2 - \frac{r^2}{2y_2 p_1} p_1 (1 - 2 \frac{{y_2}^2}{r^2})$$

$$g = \frac{r/_2}{y_2/_r}$$

$$g = \frac{r/_2}{\cos\theta} \qquad (3.18)^{10}$$

[10] Pereira, Fernandes, and Guerra Rosa 2019

It is known that the reflected ray depends on the angle, which makes the focal point of the circular profile depend on the angle of incidence.

From the diagram it can be understood that the radius of the hemisphere (XY) is denoted by

$$XY = XC' + C'Y$$

$$r = f + g$$

$$f = r - g$$

$$f = r\left(1 - \frac{1}{2\cos\theta}\right) \qquad (3.19)$$

The above equation indicates that the focal point of a ray incident on a spherical surface depends on the angle at which it is reflected. The focal length is directly affected by the position of the ray within the hemispherical surface. It can be understood from the above equation that for small angles, the focal length of the circular profile is $\approx {}^{1}/_{2}$ r.

3.4: Paraboloidal Reflection Model

The paraboloidal model is made of a parabolic cross section along the 2D plane, which is revolved about y-axis. The previous assumption that the solar ray incident on the curved surface of the model is parallel to y-axis is considered here as well. The vector denoting all these rays can be assumed to be one and the same as the ray, which is represented along the y-axis. For better understanding of the ray trace, only a 2D model of the system is considered. The vector equation of a line parallel to y-axis is denoted by *(0, p_1).*

The incident rays are reflected at B *(z_2, y_2),* and converge at C' *(z_3, y_3),* which can also be represented as *(0, f)* as the circular profile converges the reflected rays at its focal point.

$$(0, f) = (z_2, y_2) + s\,\overrightarrow{BC'} \qquad (3.20)$$

Substituting equation *(3.2)* in our paraboloidal model

$$\overrightarrow{BC'} = \overrightarrow{AB} - 2\,(\overrightarrow{AB} \cdot \vec{n})\,\vec{n} \qquad (3.21)$$

$\overrightarrow{AB}$ is parallel to *y axis* making its vector point *(0 , p_1)*

To determine the unit normal vector to a paraboloid

Equation of parabola: $y = az^2$

$$F(z, y) = y - az^2 = 0$$

$$F(z) = -2az \;;\; F(y) = 1$$

$$\vec{n} = \frac{\nabla F}{\| \nabla F \|}$$

$$\vec{n} = \frac{(-2az, 1)}{\sqrt{(4a^2z^2 + 1)}}$$

$$\vec{n} = \frac{-2az}{\sqrt{(4a^2z^2 + 1)}}, \frac{1}{\sqrt{(4a^2z^2 + 1)}} \qquad (3.22)^{10}$$

[10] Pereira, Fernandes, and Guerra Rosa 2019

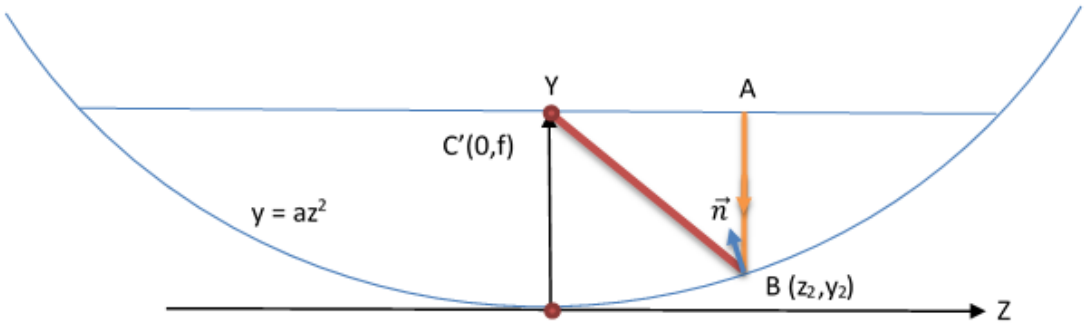

Figure 32: Specular reflection of solar ray $\overrightarrow{AB}$ by a paraboloidal surface (Pereira, Fernandes, and Guerra Rosa 2019)

Substituting equation *(3.22)* in equation *(3.21)*

$$\overrightarrow{BC'} = (0, p_1) - 2\{(0, p_1) \cdot \left(\frac{-2az_2}{\sqrt{(4a^2z^2+1)}}, \frac{1}{\sqrt{(4a^2z^2+1)}}\right)\} \left(\frac{-2az_2}{\sqrt{(4a^2z^2+1)}}, \frac{1}{\sqrt{(4a^2z^2+1)}}\right) \quad (3.23)$$

Substituting equation *(3.23)* in equation *(3.20)*

$$(0, f) = (z_2, y_2) + s[(0, p_1) - 2\{(0, p_1) \left(\frac{-2az_2}{\sqrt{(4a^2z^2+1)}}, \frac{1}{\sqrt{(4a^2z^2+1)}}\right)\} \left(\frac{-2az_2}{\sqrt{(4a^2z^2+1)}}, \frac{1}{\sqrt{(4a^2z^2+1)}}\right)\}]$$

$$(0, f) = (z_2, y_2) + [s\,(0, p_1) - 2\,s\,\{(0, p_1) \cdot \left(\frac{-2az_2}{\sqrt{(4a^2z^2+1)}}, \frac{1}{\sqrt{(4a^2z^2+1)}}\right)\} \left(\frac{-2az_2}{\sqrt{(4a^2z^2+1)}}, \frac{1}{\sqrt{(4a^2z^2+1)}}\right)]$$

$$(0, f) = (z_2, y_2) + s\,(0, p_1) - 2\,s \left(\frac{p_1}{\sqrt{(4a^2z^2+1)}}\right) \left(\frac{-2az_2}{\sqrt{(4a^2z^2+1)}}, \frac{1}{\sqrt{(4a^2z^2+1)}}\right)$$

$$(0, f) = (z_2, y_2) + s\,(0, p_1) - \left(\frac{2sp_1}{\sqrt{(4a^2z^2+1)}}\right) \left(\frac{-2az_2}{\sqrt{(4a^2z^2+1)}}, \frac{1}{\sqrt{(4a^2z^2+1)}}\right)$$

Equating *z axis* and *y axis* with its respective components

$$z \text{ axis} : 0 = z_2 + s\,(0) - 2sp_1 \frac{2az_2}{(4a^2z^2+1)}$$

$$s = -\left\{\frac{4a^2z^2 + 1}{4ap_1}\right\} \quad (3.24)$$

$$y \text{ axis} : f = y_2 + s\,(p_1) - \frac{2sp_1}{(4a^2z^2+1)} \quad (3.25)$$

Substituting equation *(3.24)* and $y = az^2$ in equation *(3.25)*

$$f = \frac{1}{4a} \quad (3.26)^{10}$$

The above equation indicates that the focal point of a ray incident on a paraboloidal surface is independent of the angle at which it is reflected. Focal length of the model remains the same irrespective of the position of the ray within the paraboloidal surface.

[10] Pereira, Fernandes, and Guerra Rosa 2019

3.5: Selection of Reflector Profile

In order to concentrate solar radiation onto the receiver surface, a reflector is required. The reflector is selected based on its optic properties. From the literature review, it was understood that the reflector can either possess a parabolic profile or a circular profile. The mathematical model of the solar ray trace with respect to these profiles is derived.

Based on the derived equation, it is understood that the ray-trace of a parabolic profile setup is independent of the rim angle. When the incident radiation is parallel to the axis of the reflector, the parabolic reflector focuses solar radiation to a point source, irrespective of the placement of the incident solar radiation within the reflector zone. This implies that solar radiation concentrated by the parabolic profile on the receiver will have a uniform behaviour.

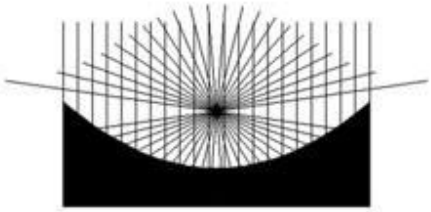

Figure 33: Parabolic mirror behaviour – axial incident (Rogers et al. 2012)

Based on the derived equation, it is understood that the ray-trace of the circular profile is dependent on the rim angle. When the incident radiation is parallel to the axis of the reflector, the circular reflector is unable to focus solar radiation to a point source, but rather forms a cluster. This cluster formation, also known as a spherical aberration, is formed due to cosine angle factor. Depending on the placement of incident solar radiation, the ray closer to the axis reflects at a higher focal point, while the ray farther from the axis reflects at a lower focal point. This implies that solar radiation concentrated by the circular profile on the receiver will have an aberration behaviour.

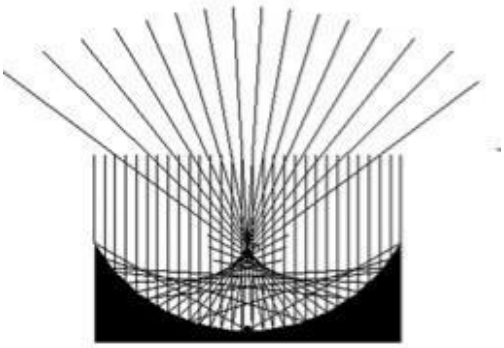

Figure 34: Circular mirror behaviour – axial incident (Rogers et al. 2012)

Although the parabolic profile exhibits a uniform behaviour, this holds true only when the incident radiation is axially inclined. Axial inclination is only possible when the tracking mechanism is of high precision to follow sun's path. For increased off-axis incidence, the magnitude of the aberration increases as well.

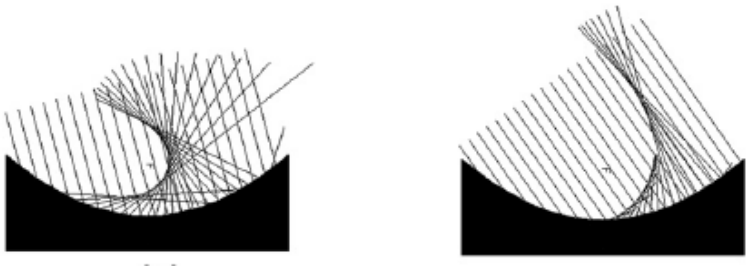

Figure 35: Parabolic mirror behaviour – off axis incident
(Rogers et al. 2012)

On the other hand, the circular profiles exhibit consistent aberrations irrespective of the off-axis incidence. This indicates that the tracking mechanism deployed for such profiles doesn't require high precision to follow sun's path.

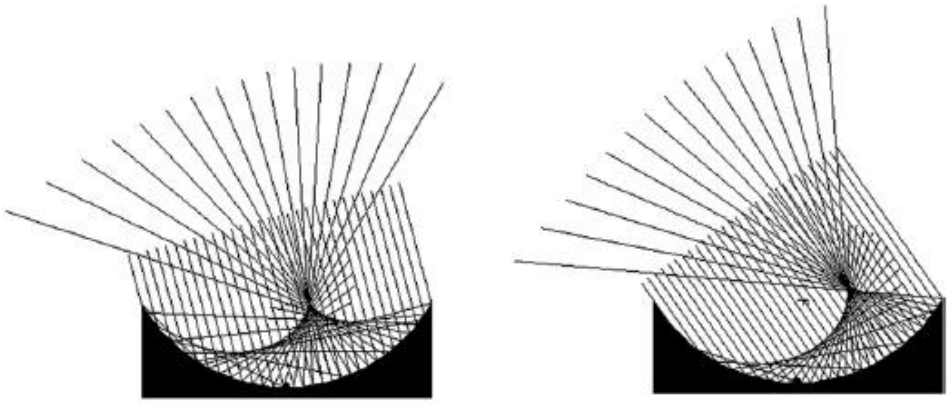

Figure 36: Circular mirror behaviour – off axis incident
(Rogers et al. 2012)

3.6: Design of Base Reflector

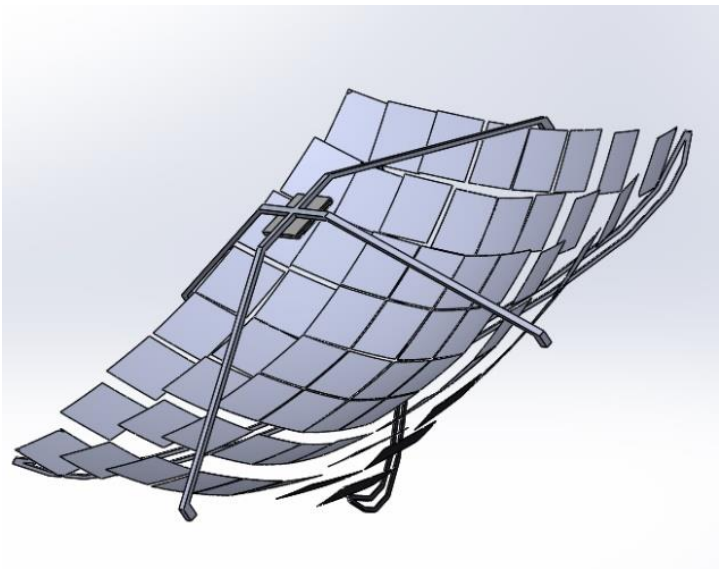

Figure 37: Iso view of Concentrator Optics along with receiver

The base reflector of our proposed model is comprises of 60 mirrors of size 600mm x 600 mm, with an additional 4 mirrors of size 250mm x 250mm. The arrangement of these mirrors is done in such a way, that overall shape of the base reflector resembles that of a distorted parabolic shape. This shape can be claimed as compound curvature in nature.

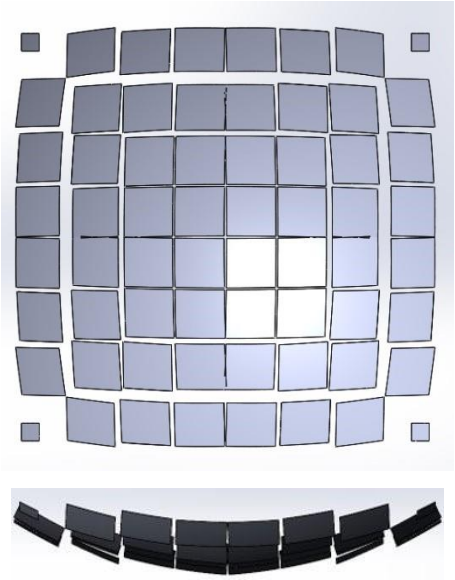

Figure 38: Top and Side view of Concentrator Optics without receiver

These reflectors are designed and positioned on the base as the primary optical setup. The design considers various parameters like shading effect of reflectors, complexity involved in mirror manufacture, and high uniformity in the distribution of radiation over the flat receiver.

3.7: Approximation Equation

The POE, as discussed above, is a compound curvature structure, which is carefully modelled to suit our requirements. Although it is mentioned that hemispherical mirrors almost equate to paraboloidal mirrors in performance when the ratio of $A_p/2f$ is 0.55 (Nijegorodov, Jain, and Devan 1995). This can only be verified by the Fermat's Principle of Least Time (FPLT). FPLT provides us with near approximation method. The FPLT states that the light rays always follow the path which takes the least amount of time.

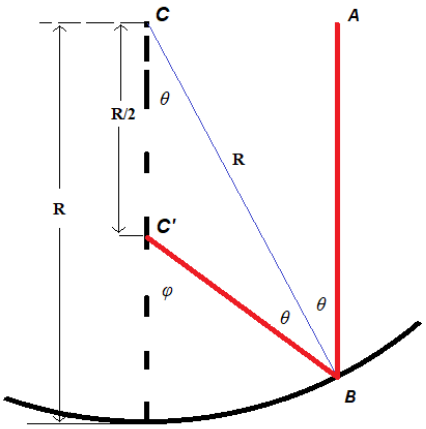

Figure 39: Reflection of light rays parallel to axis of spherical mirror (not to scale)

The centre point of the spherical mirror is C and the radius is R. The axis of the mirror is along the line CC'. The light ray starts from point A and is reflected off the mirror at B. According to Snell's law, the angle of incidence equals the angle of reflection. Assume the above reflection in a vertex arrangement with C' as a point on the receiver. In the graph below, a circle is plotted with the centre at y = 5 and x = 0 and radius R =5.

Equation of circle plotted in the above graph is

$$(x-0)^2 + (y-R)^2 = R^2$$

This can be rewritten as

$$x^2 = 2Ry - y^2$$

Substituting R = 5, the final equation is

$$x^2 = 10y - y^2$$

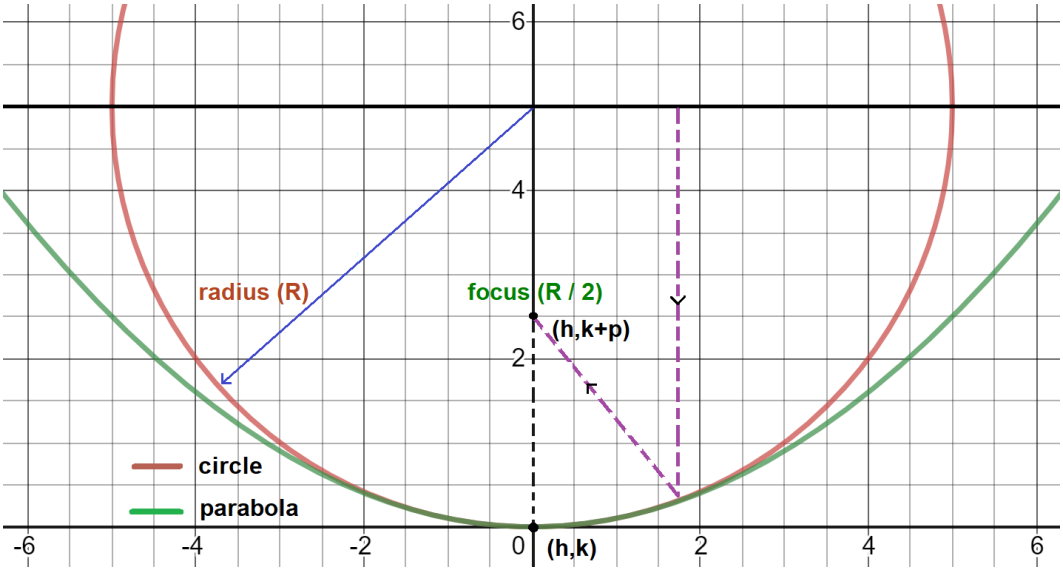

Figure 40: Near vertex approximation of circle and parabola ("Desmos | Graphing Calculator" n.d.)

In the graph a parabola is plotted with focus at y = 2.5 and x = 0. The axis of the parabola passes through the focus and is perpendicular to the directrix. The standard equation form of a parabola is:

$$(x-h)^2 = 4p(y-k)$$

Equation for our particular parabola is

$$x^2 = 4py$$

If the focus of the parabola is at (0, f), with the vertex at the origin and the centre of the circle at (0, R), then the parabola is

$$x^2 = 4fy$$

Substituting $f = \frac{R}{2} = 2.5$, the final equation is

$$x^2 = 10y$$

Through the above equation and graphical representation, it is concluded that in the region closer to the axis of the parabola, the two curves approximate to one another. In terms of the mathematical equation, there is a difference of y^2 between both profiles. However, the value of y^2 is negligible for relatively small values of y. When considering osculation and the approximation along the vertex of both profiles, there is a requirement for our base system to possess reflectors (POE) with a higher radius of curvature. The system should be mathematically designed for any chosen profile to trace the rays of solar irradiation falling onto the receiver provided that the incident angle of radiation is also low.

The individual mirrors of the compound curvature setup will largely reciprocate the parabolic profile, however, it will not remain truly parabolic in nature owing to the vertex approximation. Parabolic mirrors also come with manufacturing difficulty, and aberration, which increases with off axis incidence. On the other hand, a spherical mirror possesses great deal of manufacturing ease, and proves to be cost effective, but do not focus the light rays to a point. In order to address the problem at hand, the simple curvature of the individual mirrors, and their placements has been modelled to take advantage of both profiles. The rim angle of the compound curvature set-up is discussed in the later section.

3.8: Area of Curved Surface (3 Dimensional)

Considering the use of simple curvature for all our mirror reflectors, surface area must be calculated to determine the energy on the surface. The surface area of a linear profile (2D) is easy to calculate, while the surface area of a square cut hemispherical profile (3D) requires surface area calculation using double integration. In a spherical coordinate system, it is simple to calculate the surface area of sphere or a portion of a sphere. It is a known fact that, surface area of sphere is $A = 4\pi r^2$.

The spherical coordinate system is denoted by r, θ, Φ instead of x, y, z. A line is drawn at an angle θ above the xy plane and the same line is tilted away from yz plane at Φ. The length of the line indicates the radius of the sphere we have considered. The projected line of r on xy plane is $r \cos \theta$. The surface element dA is calculated by $r\, d\theta$ and $r \cos\theta\, d\Phi$

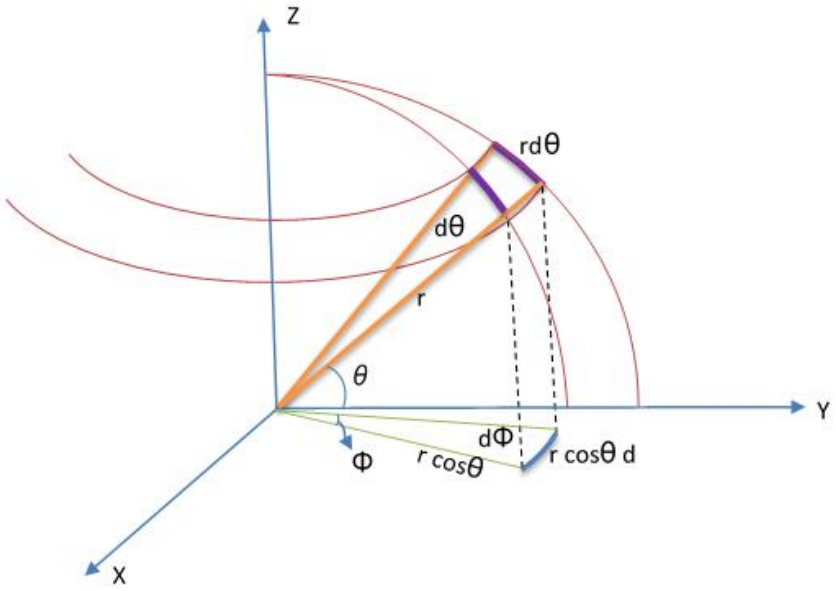

Figure 41: Representation of surface area of reflector

Surface area of reflector $A_{ref} = \iint dA$

$$A_{ref} = r^2 \int_{-\theta}^{+\theta} \cos\theta \, d\theta \int_0^{\emptyset} d\Phi \qquad (3.27)^7$$

3.9: System Design Parameters

To describe the design parameters of the proposed model, there are 3 key parameters must be discussed: geometric concentration, optic concentration, and optic efficiency of the system. The geometrical concentration ratio (C_g) is defined by the area of a reflector mirror to the receiver area. Our model uses multiple reflectors (64 in total), which focus solar irradiation onto a single receiver.

$$C_g = \frac{\sum_{j=1}^{n} A_{ref,j}}{A_{rec}} \qquad (3.28)^{11}$$

The optical efficiency of the model is defined as the ratio between the solar irradiation absorbed by the receiver to the solar radiation incident on the reflector

$$\eta_{opt} = \frac{Q_{rec}}{Q_{ref}} \qquad (3.29)^{11}$$

The total solar radiation absorbed by the receiver includes components such as reflectivity of the mirror, cosine of the angle ($f *_{cos\theta}$) of the incident ray on the reflector ($f *_{ref}$), and the incident rays that do not converge ($f *_{con}$) to the receiver area.

$$Q_{rec} = Q_{ref} . f *_{cos\theta} . f *_{ref} . f *_{conv} \qquad (3.30)^{12}$$

The optic concentration ratio of our system has a large number of reflectors, and a single receiver which receives uniform radiation.

$$C_{opt} = \frac{average\ flux\ over\ the\ receiver}{flux\ over\ the\ aperture}$$

$$= \frac{I_{rec}}{\frac{1}{\sum_{j=1}^{n} A_{ref,j}} \left\{ \sum_{j=1}^{n} A_{ref,j} \, . \, I_{ref,j} \right\}}$$

$$= \frac{\left[\sum_{j=1}^{n} A_{ref,j} \right] . \ I_{rec}}{\sum_{j=1}^{n} A_{ref,j} \, . \, I_{ref,j}} \qquad (3.31)^{11}$$

It can also be expressed in terms of the geometric concentration ratio

$$C_{opt} = C_g \eta_{opt} \qquad (3.32)^{13}$$

[7] Thomas 2013
[11] Sirimanna and Nixon 2019
[12] Rinaldi et al. 2014
[13] Brogren 2004

3.10: Design of Individual Reflector

All simple curvature mirrors are cut into a square profile of 600 mm x 600 mm in order to maintain the uniform projected arc length of reflectors irrespective of their radius of curvature.

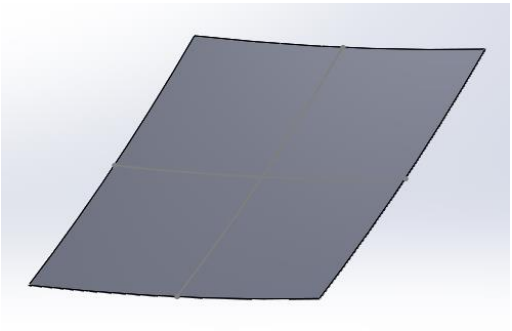

Figure 42: Simple curvature profile of single mirror

3.11: Rim Angle of Individual Reflector

In order to calculate the angle of ray traces which facilitate concentration, a simple approach is considered. A circular sector is taken into account, which is enclosed by 2 radii and an arc. For small angles, these radii lines act as the boundary lines of solar rays within which all focus lines are concentrated. Consider the single mirror in 2D, and impose the solar concentration by sector of circle formula.

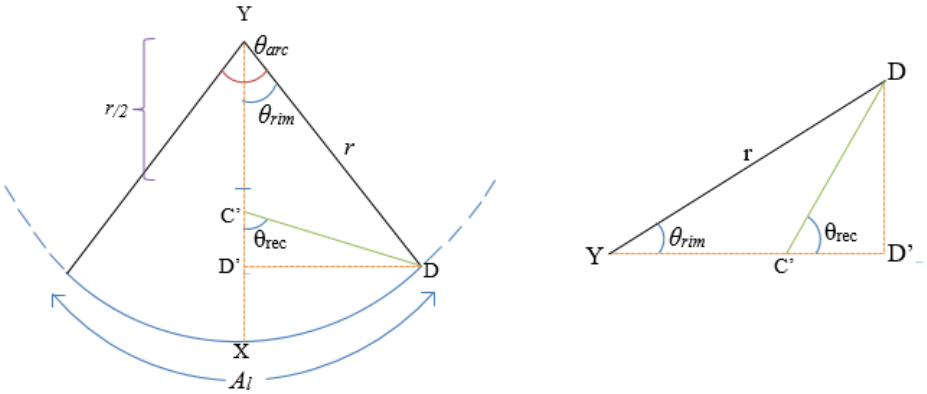

Figure 43: Rim angle of individual reflector

$$A_l = \frac{\theta_{arc}}{360} 2\pi r$$

For constant arc length A_l (0.60 m), the radius of curvature, and the angle of sector of the circle in 2D are proportional to each other. By rearranging the equation for the selected radius of curvature of the reflectors, the angle can be calculated as

$$\theta_{arc} = \frac{108}{\pi r} \qquad (3.33)$$

From equation *(3.18)* and *(3.33),* it is known that

$$\theta_{in} = \theta_{rim} = \frac{\theta_{arc}}{2} \qquad (3.34)$$

The angle of the reflected ray with respect to axis to revolution also establishes a relation with the rim angle of the reflector.

$$cos\,\theta_{rim} = \frac{YD'}{YD}$$

$$YD' = r.\cos\theta_{rim}$$

$$C'D' = YD' - C'Y$$

From equation *(3.18),* it is known that $C'Y = \frac{r}{2\cos\theta_{rim}}$

$$C'D' = r.\cos\theta_{rim} - \frac{r}{2\cos\theta_{rim}}$$

$$C'D' = r\left(\frac{2\cos^2\theta_{rim} - 1}{2\cos\theta_{rim}}\right)$$

By the double angle formula, it is known that *cos 2θ = 2cos²θ -1 and sin 2θ = 2sinθ.cosθ* substituting in the above equation

$$C'D' = r\left(\frac{cos\,2\theta_{rim}}{2\,cos\,\theta_{rim}}\right)$$

$$sin\,\theta_{rim} = \frac{DD'}{YD}$$

$$DD' = r.sin\,\theta_{rim}$$

$$tan\,\theta_{rec} = \frac{DD'}{C'D'}$$

$$tan\,\theta_{rec} = \frac{r.sin\,\theta_{rim}}{r\left(\frac{cos\,2\theta_{rim}}{2\,cos\,\theta_{rim}}\right)}$$

$$tan\,\theta_{rec} = \frac{2\ sin\,\theta_{rim}.cos\,\theta_{rim}}{cos\,2\theta_{rim}}$$

$$tan\,\theta_{rec} = \frac{sin\,2\theta_{rim}}{cos\,2\theta_{rim}}$$

$$\theta_{rec} = 2\theta_{rim} \qquad (3.35)$$

The reflected ray with respect to the axis of revolution is twice the rim angle of reflector. Hence a relationship between the arc angle of the reflector, and the reflected angle of ray is established as they are equal to one another.

3.12: Focal Length of Individual Reflector

For small angles *θ,* the assumption of paraxial approximation is always valid. For small values of *cos θ* (*cos θ ≈1),* the equation is simplified as given below. This equation is applicable only to calculate the focal length of reflector as a single entity with smaller arc length.

$$f_{ir} \approx \left(\frac{r}{2}\right)$$

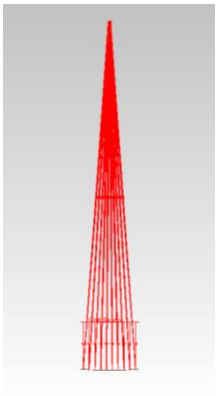

Figure 44: Ray tracing of a single reflector with large radii of curvature (TracePro)

The same case cannot be considered for reflectors with bigger arc lengths, as they have higher effect on the focal length. Thus, the cosine factor must be factored in. The true focal length of a spherical profile reflector is calculated in the equation *(3.19)* as

$$f = r\left(1 - \frac{1}{2\,cos\theta_{rim}}\right)$$

3.13: Modified Focal Length of Individual Reflector for Parallel Rays

An ideal curved mirror/reflector focuses solar irradiation at the same focal point irrespective of the incident angle. However, when it comes to commercially available reflectors, they always showcase aberrations over the focal point. Although parabolic mirrors have zero aberrations at the 0º incident angle (ray trace perpendicular to the surface), they have increased aberrations when there is a slight deviation from the incident angle. On the other hand, spherical reflectors always produce aberrations irrespective of the ray incidence angle (Saleh Ali et al. 2013).

This also plays a hand in selection of spherical profile reflectors over parabolic designs. These aberrations produce non-uniformity of concentrated solar radiation collected on the receiver. Non-uniformity of radiation results in reduced output for CPV designs. To overcome these spherical aberrations, the receiver is placed at a distance from the true focal length closer to the reflectors, resulting in uniform distribution of radiation over the receiver at any incident angle.

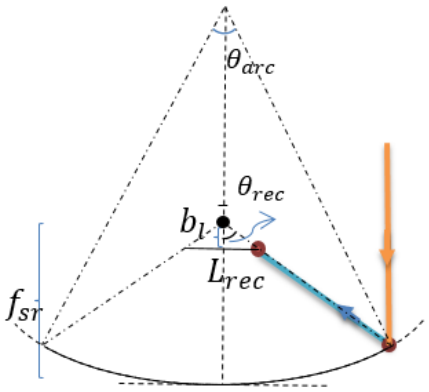

Figure 45: Modified focal length of incident ray

From equations (3.19), (3.33) and (3.34), it is understood that the angle of rays ($\theta_{rim,sr}$) and focal length of the model (f) is dependent on the radius of curvature. To calculate

rim angle, assume the incident ray is normal to the aperture of the mirror, then the rim angle Φ, the incidence angle θ, and slope angle ω are equal. Consider the receiver along a single axis, the length of the receiver (L_{rec}) is maintained at a constant (250 mm) to receive uniform radiation from the reflectors. The length of the receiver also determines the geometric concentration of the proposed model, which was discussed earlier.

$$f_{ir} = f_{mod,ir} + b_l$$
$$b_l = \frac{L_{rec}}{2\ tan\,\theta_{rec}} \qquad (3.36)$$
$$f_{mod,ir} = f_{ir} - \frac{1}{2}\left(L_{rec}\,.\tan^{-1}\theta_{rec}\right)$$

3.14: Effect of Solar Disc Angle on Modified Focal Length

Although the system is designed based on an assumption that the solar rays are truly parallel, the fact that the angular diameter of the sun has an influence over the angle between the rays emitted by the sun must be considered. The angular diameter of the sun varies between 0.52º to 0.54º. The half angular width of the sun is 4.625 x 10^{-3} radians.

Based on equations *(3.34)* and *(3.35)*

$$\theta_{rim} = \frac{\theta_{arc}}{2} = \frac{\theta_{rec}}{2} \qquad (3.37)$$

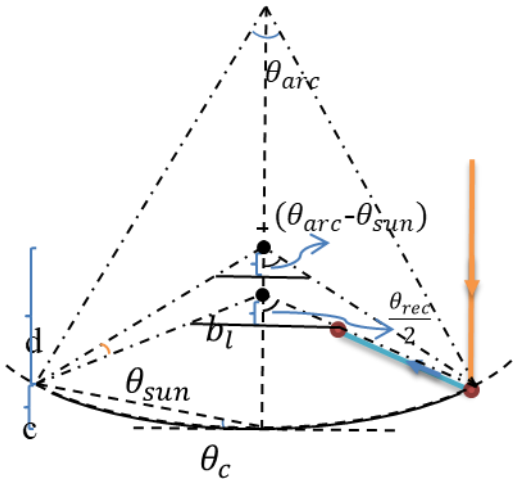

Figure 46: Modified focal length with solar disc angle

In order to calculate the modified focal length of the receiver with the sun's half angle factor (θ_{sun}) on a 2D plane, various parameters are considered such as focal length of the spherical reflector for uniform rays (f_{uni}), the vertical displacement of the receiver for uniform rays (b_{uni}), the vertical displacement between the center and edges of reflector (c), the vertical displacement of solar ray focal length of the edges of reflector (d), the focal length of spherical reflector for solar rays (f_{solar}), and the vertical displacement of the receiver for solar rays (b_{solar}). The solar rays are incident perpendicular to the receiver aperture as indicated in the Figure 33. The length of reflector (L_{ref}) along a single axis is 600 mm.

From equation *(3.19)* and *(3.35),* it is known that

$$f_{uni} = r\left(1 - \frac{1}{2\,cos\frac{\theta_{arc}}{2}}\right) \quad (3.38)$$

From equation *(3.36),* it is known that

$$b_{uni} = \frac{L_{rec}}{2\ tan\,\theta_{arc}} \quad (3.39)$$

$$f_{solar} = c + d$$

$$c = \frac{L_{ref}\ .\ tan\theta_c}{2}$$; For small values of θ_c

$$d = \frac{L_{ref}}{2\ tan(\theta_{arc} - \theta_{sun})} \quad (3.40)$$

From equation *(3.39),* it is known that

$$b_{solar} = \frac{L_{rec}}{2\ tan(\theta_{arc} - \theta_{sun})} \quad (3.41)$$

Modified focal length of the system with solar rays

$$f_{mod,solar} = f_{solar} - b_{solar}$$

$$f_{mod,solar} = \frac{(L_{ref}\ .\ tan\,\theta_c)}{2} + \left(\frac{L_{ref} - L_{rec}}{2\ tan(\theta_{arc} - \theta_{sun})}\right) \quad (3.42)$$

3.15: Design of Collective Reflectors

The design of an individual reflector is the first step towards the design of the base reflector. The parameters of the base reflectors are the same as those of individual reflectors with additional complexity added to the system. The overall model needs to focus solar irradiation onto the receiver, with uniformity in the radiation, irrespective of the placement and orientation of the reflectors on the base setup. The orientation of the reflector is hugely influenced by the angle at which the reflectors are aligned with respect to its placement. The initial setup is made using single curvature mirrors. The orientation of the reflectors is calculated using Pythagoras and single ray technique as shown below.

The placement of the reflectors is affected by various factors, which are mentioned in the above sections. For the required amount of uniformly distributed concentrated irradiation on the receiver, the radius of curvature of the individual reflectors should be different. Their positions accounts for shading effects, and optimal distance between reflectors to reduce losses. For the selected radius of each reflector, the rim angle is affected, as well as the focal length between the reflector and the receiver. This focal length influences the height at which the reflector is placed with respect to the receiver.

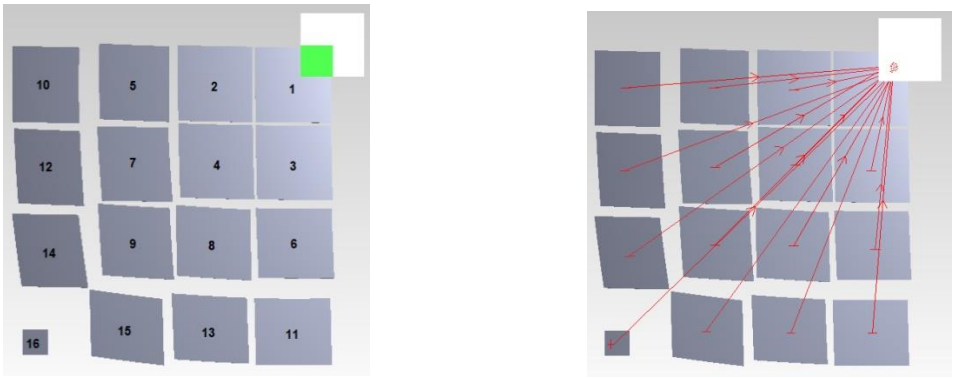

(a) (b)

Figure 47: *Numerical representation of reflectors with highlighted 1/4th receiver area (a) and determination of incident angle for each reflector using single ray trace technique*

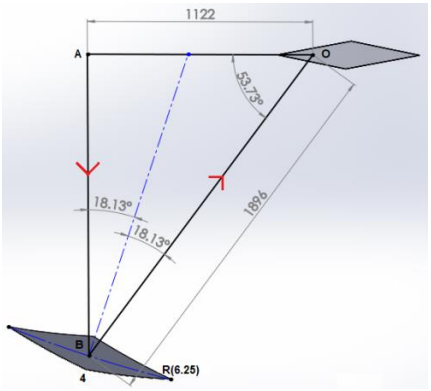

Figure 48: Pictorial representation of single ray trace on 4th reflector

The base model is designed symmetrically with 16 reflectors at measured distant from one another, and is aligned to concentrate on 1/4th of the receiver area. The design also takes into consideration the shading effects of the receiver holders. The relative distance of reflector to the mid-point of the highlighted receiver area along the 2D plane (x-y axis) is calculated based on the size and position of each reflector. The position of receiver is fixed while that of the reflector is altered along the x-z plane to attain the geometric concentration of 5.76 suns for each reflector. The 16th reflector is pro-rated in terms of size to fill the shading effect of the1st reflector.

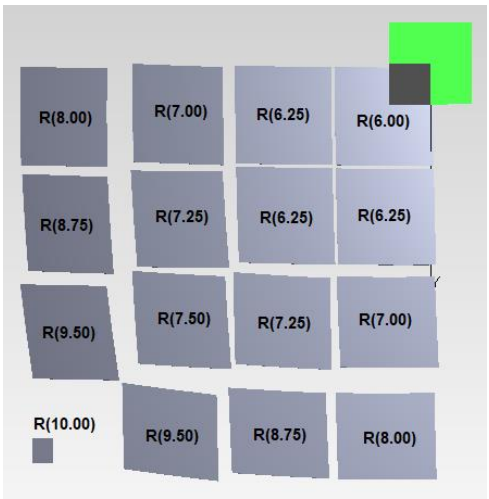

Figure 49: Radius of curvature of reflector design – iteration 1

Table 1: Design iteration 1 – Focal length, angle and radius of reflectors

Reflector number	Radius of curvature (m)	R-R Displacement in x-z plane (mm)	R-R Displacement in x-y plane (mm)	∠AOB (deg)	Incident Angle
1	6.00	1758	266	81.27	4.37
2	6.25	1828	823	63.23	13.39
3	6.25	1828	823	63.22	13.39
4	6.25	1896	1122	53.73	18.13
5	7.00	2109	1451	46.49	21.76
6	7.00	2109	1451	46.49	21.76
7	7.25	2169	1650	40.42	24.79
8	7.25	2169	1651	40.42	24.79
9	7.50	2424	2019	33.62	28.19
10	8.00	2519	2147	31.51	29.24
11	8.00	2519	2147	31.51	29.24
12	8.75	2592	2274	28.68	30.66
13	8.75	2592	2274	28.67	30.66
14	9.50	2844	2583	24.72	32.64
15	9.50	2844	2584	24.72	32.64
16	10.00	3435	3312	15.37	37.31

3.16: Design Consideration of Base Model

The base model, also known as the POE of our system is designed specifically as a combination of paraboloidal and hemispherical profiles. Consider a 2D cross section of a curved profile reflector, the focal length f for the circular mirror with a radius of curvature R is not constant, unlike parabolic mirrors, where the reflection of parallel rays concentrate at a focus. Instead, these rays are focused at a distance $\leq 0.5R$ from the vertex point of the reflector. 0.5 R is considered as the theoretical maximum focusing distance and as such, the focal length of a circular profile mirror.

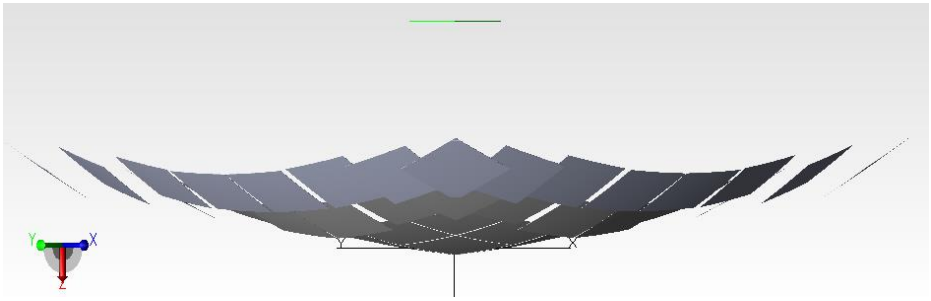

Figure 50: Side view of collective reflectors

The graph below shows the variation of the focal length with respect to the rim angle of the base. The advantage of the paraboloidal setup is the stability of the base model compared to the hemispherical model, where the height of the model is independent of the radius of curvature. In order to produce a more paraboloidal like profile for the base design, the proposed model should have lesser variation in terms of incident angle. As discussed in the earlier section, the base is made up of 63 identical sized reflectors along with 1 reduced size for shaded portion in terms of external dimensions (600 mm x 600 mm) which satisfies the ($A_p/2f$) ratio.

The variation in focal length of collective reflector design indicates that radiation produced on the receiver can be further improved.

$$f(\emptyset) = R\left\{1 - \frac{\sin \emptyset}{\sin\ 2\emptyset}\right\}$$

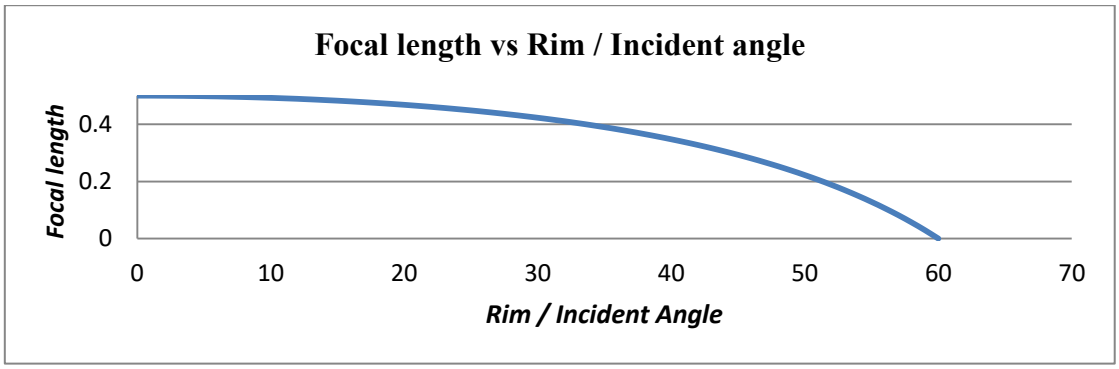

Figure 51: Dependence of focal length of proposed mirror design with circular cross-section on the rim angle
(Nijegorodov, Jain, and Devan 1995)

This observation is substantiated by the approximation equation, which was derived in an earlier section. The proposed base design has all the rays undergo only a single reflection. The incident angle of the above design varies from 4.37º to 37.31º, for its first reflector to the 16th reflector respectively.

3.17: Revised Position of the Reflectors – Design Iteration 2

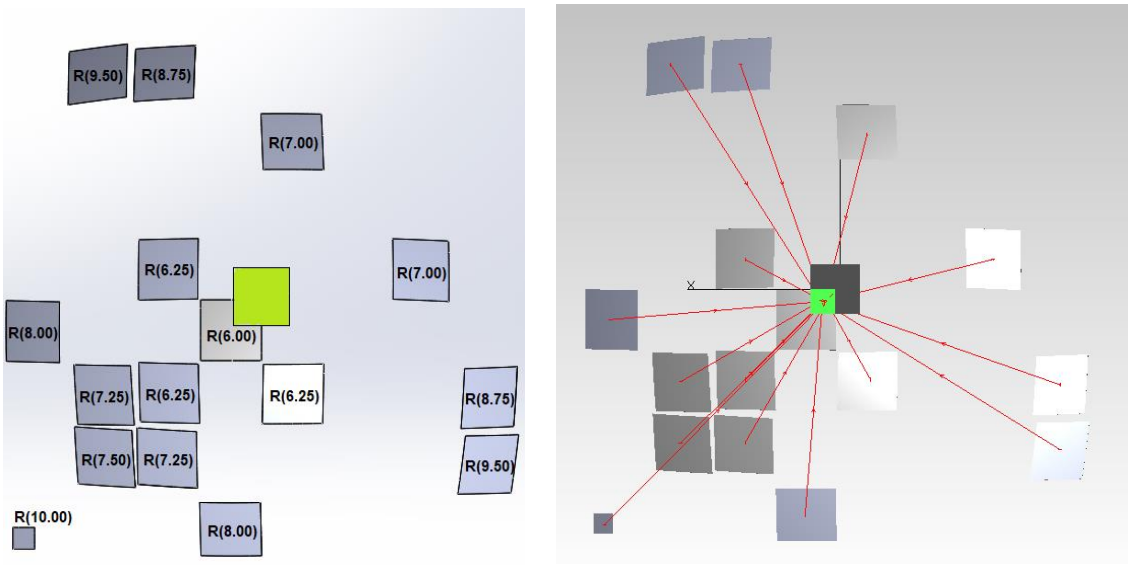

(a) (b)

Figure 52: (a) Design iteration 2 and (b) single ray trace technique to determine incident angle

In order to facilitate the design of collective reflectors as an entity, the orientation of the reflectors must be determined, which will help determine their placements. These placements are affected by various factors. The base design goes through an iteration procedure to find the angle of the individual reflectors by correction of modified focal length to achieve a constant value of 0.315 for the $f_{mod,solar}$/radius ratio. The design is also adjusted to reduce the shading effect of reflectors, which results in a reduced concentration. The angle of reflectors is also minimised by the placement of reflectors as shown in Figure 45 to reduce the loss due to aberrations.

3.18: Modified Focal Length of Revised Collective Reflector

The placement of reflectors with respect to the focal point of the receiver goes through an iteration process to reduce the variation in aberration formed on the receiver. The position of the reflectors is retained from the previous design, and the focus of the reflector is altered. This gives rise to new displacement values along the x-z plane and x-y plane with respect to the proposed focal point of the design. The new values are found in Table 2.

The 1st reflector is moved to the third quadrant as opposed to the previous design. This results in the shading of the receiver along the corners, instead of the central portion of the receiver as shown in Figure 47. As a result of change in the orientation of the 1st reflector, the orientation of the 16th reflector is also changed. The iteration process also helps us to determine the radius of curvature, and the displacement of reflectors for the new design with respect to the receiver position.

Table 2: Design iteration 2 – Focal length, angle and radius of reflectors

Reflector number	**Radius of curvature (m)**	**R-R Displacement in x-z plane (mm)**	**R-R Displacement in x-y plane (mm)**	**∠AOB (deg)**	**Incident Angle**
1	6.00	1845	619	70.61	9.69
2	6.25	1869	911	60.82	14.59
3	6.25	1869	911	60.82	14.59
4	6.25	1896	1122	53.73	18.13
5	7.00	2319	1743	41.26	24.37
6	7.00	2319	1743	41.26	24.37
7	7.25	2169	1650	40.42	24.79
8	7.25	2169	1651	40.42	24.79
9	7.50	2424	2019	33.62	28.19
10	8.00	2519	2147	31.51	29.24
11	8.00	2519	2147	31.51	29.24
12	8.75	2800	2508	26.38	31.81
13	8.75	2800	2508	26.37	31.81
14	9.50	3033	2790	23.08	33.46
15	9.50	3034	2791	23.07	33.46
16	10.00	3209	2999	20.86	34.57

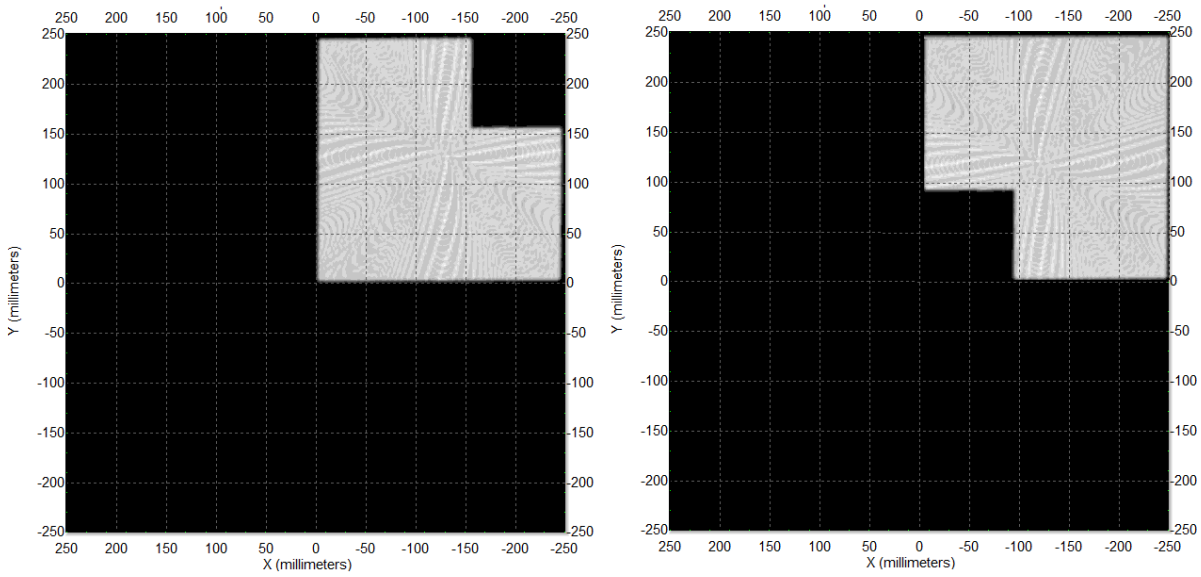

Figure 53: Shading on the receiver due to change in orientation of the 1st reflector

From equation *(3.34)* and *(3.35)*, it is known that the relation between the incident angle, rim angle, receiver angle and arc angle.

$$\theta_{in} = \frac{\theta_{arc}}{2}$$

From equation *(3.38),* it is understood that the focal length of the reflector.

$$f_{uni} = r\left(1 - \frac{1}{2\cos\theta_{in}}\right)$$

From equation *(3.28),* the geometric concentration ratio of the reflector and receiver in 2D is 2.4. This ratio is critical in the determination of the focal length of iterated incident angles.

$$A_{l,ref} = \frac{\theta_{in}}{360} 2\pi r$$

$$L_{rec} = \frac{A_{l,ref}}{2.4}$$

The length of reflector is calculated as

$$L_{ref} = r.sin\,\theta_{in}$$

In order to calculate the focal length of the reflector in their revised position.

From equation *(3.40),* the distance (d) is calculated

$$d = \frac{L_{ref}}{tan(\theta_{arc} - \theta_{sun})}$$

From equation *(3.36),* it is known

$$b_{mod,rev} = \frac{L_{rec}}{tan(\theta_{arc} - \theta_{sun})}$$

The vertical displacement between the receiver and reflector is given by

$$AB = d - b_{mod,rev} = \frac{L_{ref} - L_{rec}}{tan(\theta_{arc} - \theta_{sun})}$$

The horizontal difference between the receiver and reflector is given by

$$OA = L_{ref} - L_{rec}$$

The focal length is given by

$$f_{mod,rev} = \sqrt{(OA^2) + (AB^2)}$$

$$= (L_{ref} - L_{rec}) \cdot \sqrt{\left(\frac{1}{tan^2(\theta_{arc} - \theta_{sun})} + 1\right)}$$

$$f_{mod,rev} = \frac{L_{ref} - L_{rec}}{sin(\theta_{arc} - \theta_{sun})}$$

$$f_{mod,rev} = \frac{r\left[\sin\frac{\theta_{arc}}{2} - \left(\frac{11 \cdot \frac{\theta_{arc}}{2}}{1512}\right)\right]}{sin(\theta_{arc} - \theta_{sun})} \quad (3.42)$$

3.19: Revised Position of the Reflectors – Design Iteration 3

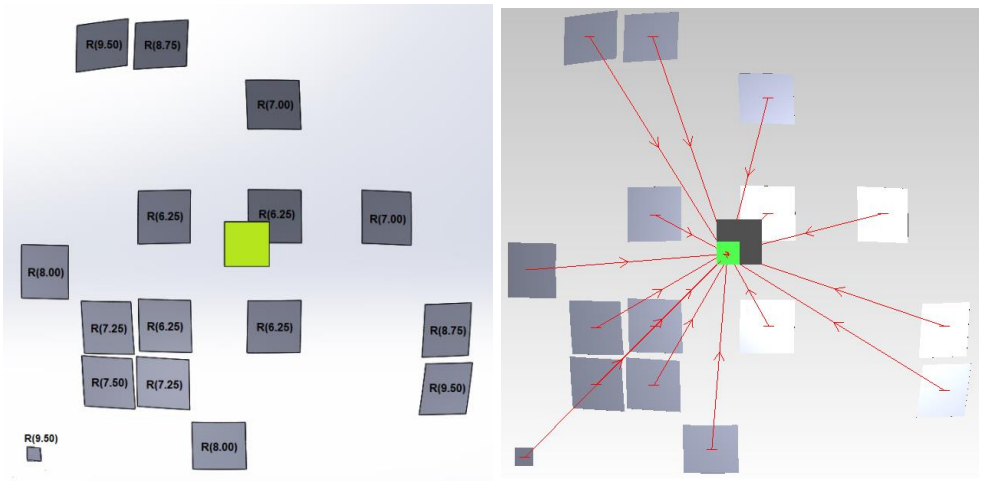

(b) (b)

Figure 54: (a) Design iteration 3 and (b) single ray trace technique to determine incident angle

Table 3: Design iteration 3 – Focal length, angle and radius of reflectors

Reflector number	Incident Angle (deg)	Radius of curvature (m)	Focal length of revised design (mm)
1	9.69	6.25	1866
2	14.59	6.25	1883
3	14.59	6.25	1883
4	18.13	6.25	1906
5	24.37	7.00	2200
6	24.37	7.00	2200
7	24.79	7.25	2284
8	24.79	7.25	2284
9	28.19	7.50	2414
10	29.24	8.00	2595
11	29.24	8.00	2595
12	31.81	8.75	2894
13	31.81	8.75	2894
14	33.46	9.50	3185
15	33.46	9.50	3185
16	34.57	9.50	3217

4: Thermal Modelling of Receiver

4.1: Introduction

The receiver part of our proposed system comprises of two main components. The first component is the MJSC, which receives the concentrated solar radiation. The second component, which is the solar collector, rejects the collateral excess heat generated to the domestic water tank. The collector is a type of heat exchanger that has the ability to transform solar radiation into heat. Solar collectors are usually designed based on their applications. The proposed system is designed to maintain the temperature of the CPV panel at less than 100 ºC, and provide enough energy to the water tank to maintain the temperature around 50ºC. A steady state analysis of heat transfer between the CPV panel and the water tank is performed to determine the thermal efficiency of the system. A simple system is considered for the model with a water tank used to store thermal energy through forced circulation of water through collector.

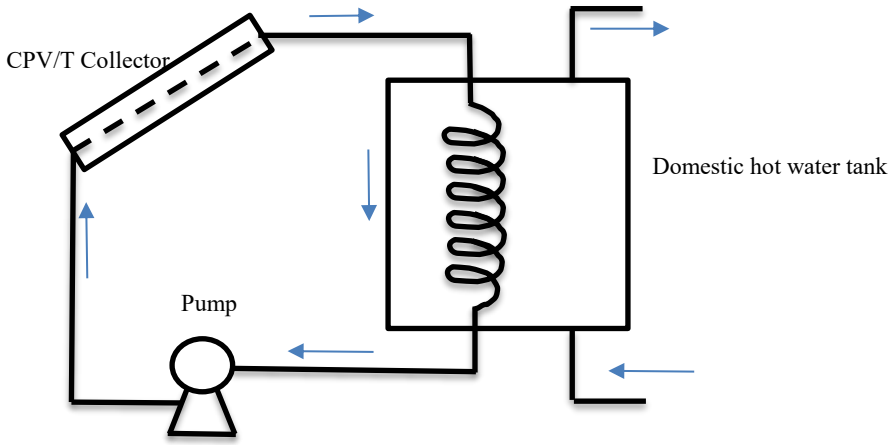

Figure 55: Schematic representation of thermal collector design

4.2: Flat Plate Collector

The proposed model is designed using a separate flat plate collector, as opposed to a concentrating collector design, which combines both the receiver and the collector as one unit. The design put forth in this thesis utilizes a water collector with an unglazed flat plate model, and uses a serpentine model, where the metal tubing or pipe is soldered to the metal sheet to transfer heat from the base plate to the water.

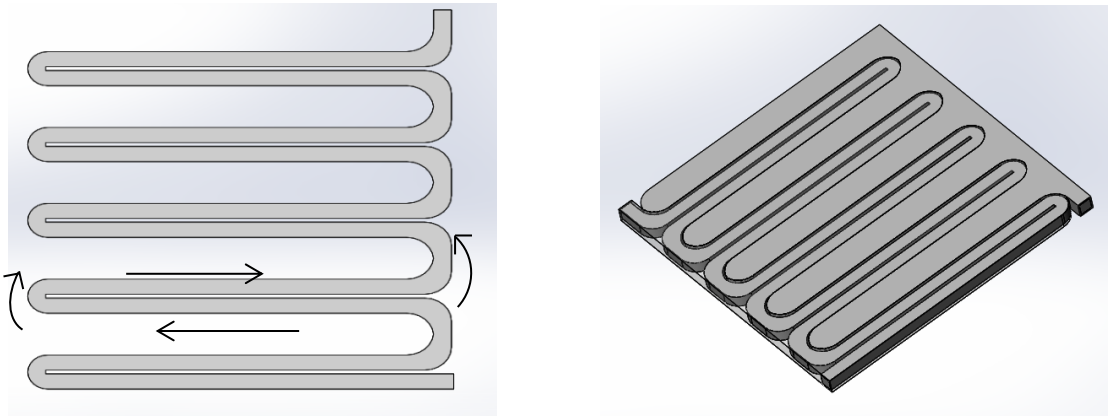

Figure 56: Serpentine model water path

The proposed serpentine model is slightly modified from regular serpentines in its use of parallel curves along the serpentine bend where the design is made to absorb heat through the pipe in the counter flow direction.

The cross section view of the proposed model indicates the placement of the tubes below the absorber plate, and does not have spacing between the tubes. Such arrangement of the tubes is required to extract heat from the absorber plate, which is subjected to concentrated solar irradiation. In order to model the thermal aspect of our system, the temperature distribution on the absorber plate is studied. The energy from the back side of the panel is passed to the absorber plate, which is welded with the tubes, and the gaps are filled with a conductance bond. This arrangement ensures the energy transfer to the fluid. Thus a temperature gradient can be observed. In order to calculate the performance of the collector, the temperature gradient along the axis of the tube and along the direction of flow must be modeled.

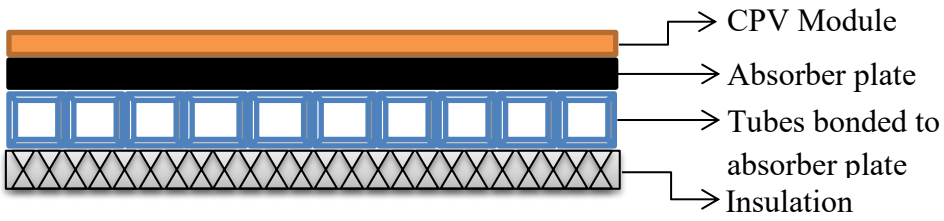

Figure 57: Cross sectional view of proposed solar collector

In order to transfer the heat to the liquid, it must be pumped through the serpentine design, which is connected to a heat exchanger. The heat exchanger is responsible for the removal of heat from the fluid. Thus the efficiency of the solar module is kept to its maximum peak value.

4.2.1: Analysis of CPVT Collector

The performance of the proposed model can be expressed in terms of combined thermal efficiency (η_{th}) and electrical efficiency (η_{CPV}), or overall efficiency. The electrical efficiency indicates the electrical gain of the proposed model, and the thermal efficiency indicates the ratio of useful thermal gain with respect to the incident solar irradiation.

$$\eta_{CPVT} = \eta_{CPV} + \eta_{th} \qquad (4.1)^{14}$$

The thermal performance of our model is affected by various design parameters. The proposed system is analysed for various incident solar irradiations with its ambient condition, and effect of different mass flow rates of the fluid used. In order to model the thermal aspect of our proposed system, the energy supplied to the receiver needs to be understood.

$$Q_u = A_{rec}\left[S_{PV} - U_L\left(T_{pm} - T_a\right)\right] \qquad (4.2)^{15}$$

The solar radiation absorbed by the collector per unit area (Q_u) equals the difference between incident solar radiation and summation of electrical gain and the heat loss (U_L) of the system. The thermal energy lost to the surroundings by conduction, convection and radiation is denoted by the product of heat transfer coefficient and temperature difference between the mean absorber plate temperature (T_{pm}) and ambient temperature (T_a).

[14] Fudholi et al. 2014
[15] Duffie and Beckman

4.2.2: Thermal Network of Proposed Model

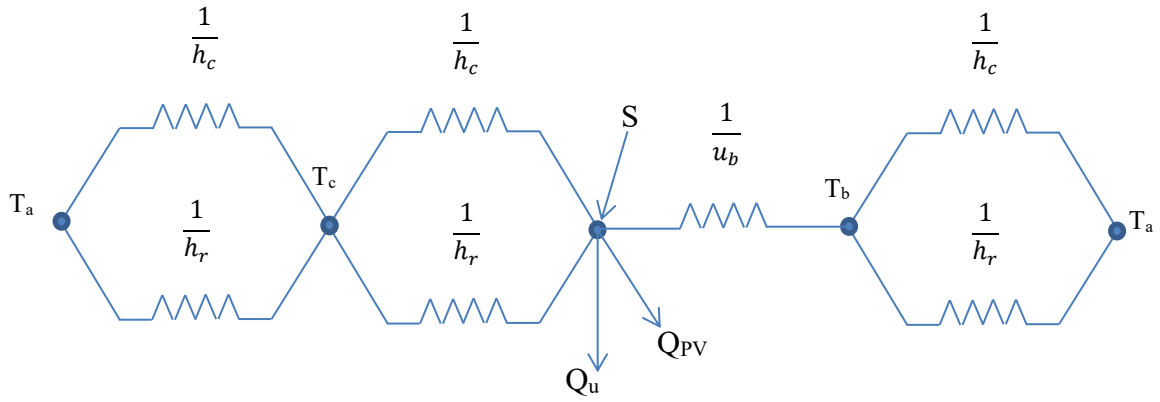

Figure 58: Thermal network in terms of conduction, convection and radiation resistance

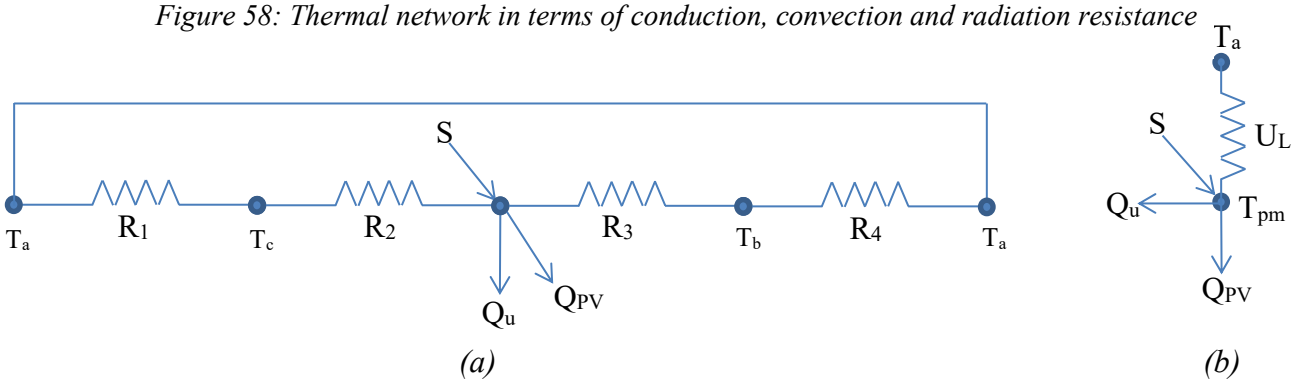

Figure 59: Simplified thermal network: (a) resistance between plates and (b) overall loss coefficient

The thermal efficiency of the system is given by the ratio of gained thermal energy by the collector to the total incident solar irradiation on the system is given by

$$\eta_{th} = \frac{Q_u}{S}$$

The useful heat gained by the model can be determined using a modified Hottel-Whillier equation

$$Q_u = F_R[S^* - A_{rec}U_L(T_i - T_a)] \qquad (4.3)^{15}$$
$$S^* = C_{opt}\, G_T - S_{PV}\ ;\ C_{opt} = C_g\eta_{opt}$$

Where S^* is the solar irradiation available at the receiver, C_{opt} is the product of optical efficiency of the mirror design and geometric concentration ratio and S_{PV} is the solar radiation gained by the multi junction solar module. In order to compute the mean plate temperature in *(4.2)* the equation is modified to express the heat gain in terms of inlet water temperature and a heat removal factor F_R is introduced. F_R is the ratio of actual heat transfer to the maximum possible heat transfer. The assumption made here is that the temperature of the surface of entire receiver is same as that of fluid inlet temperature.

$$F_R = \frac{\dot{m}C_p}{A_{rec}U_L}\left(1 - e^{-\frac{A_{rec}U_L F'}{\dot{m}C_p}}\right) \qquad (4.4)^{15}$$

[15] Duffie and Beckman

Where F' is the collector efficiency factor and can be calculated by

$$F' = \left[\frac{\frac{1}{U_L}}{U_L(D_h+(W-D_h)F)}\right] + \frac{1}{C_b} + \frac{1}{2(a+b)h_{fi}} \quad (4.5)^{14}$$

where C_b is bond conductance. It is required to bridge the gap between absorber plate and tube which reduces loss of performance. For an ideal metal-to-metal contact, the bond conductance is needed to be more than 30 W/m K.

The collector flow factor is a function of single variable that is dimensionless collector capacitance rate. This flow factor helps in finding the mean fluid temperature, which is given by

$$F'' = \frac{F_R}{F'} \quad (4.6)^{14}$$

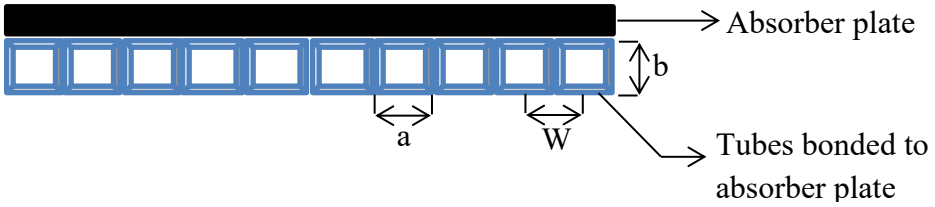

Figure 60: Schematics of absorber plate with water tubes

The fin efficiency (in this case tubes) is calculated using

$$F = \frac{tanh\left(M\frac{W-D_h}{2}\right)}{\sqrt{M\frac{W-D_h}{2}}} \quad (4.7)^{14}$$

The hydraulic diameter (D_h) is calculated by

$$D_h = \frac{2ab}{(a+b)} \quad (4.8)^{14}$$

The coefficient M in the above equation considers both the thermal conductivity of absorber plate and the multi junction solar module (Fernandez, Eduardo et al. 2015).

$$M = \sqrt{\frac{U_L}{k_{abs}l_{abs}+k_{PV}l_{PV}}} \quad (4.9)^{14}$$

The overall loss coefficient (U_L)is the sum of edge (U_e), top (U_t) and back (U_b)loss coefficients which is expressed by

$$U_L = U_e + U_t + U_b$$

[14] Fudholi et al. 2014

The edge loss coefficient is calculated by

$$U_e = \frac{\frac{k_e}{l_e} p t_{rec}}{A_{rec}} \quad (4.10)^{14}$$

The back loss coefficient is calculated by

$$U_b = \frac{k}{L} \quad (4.11)^{15}$$

The top loss coefficient is calculated by

$$U_t = h_r + h_c$$

The proposed model has adopted an unglazed collector design, and the heat loss due to radiation (h_r) is given by

$$T_s = 0.037536 T_a^{1.5} + 0.32\, T_a \quad (4.12)^{15}$$

$$h_r = \sigma \epsilon_p \left(T_{pm}^2 + T_s^2\right)\left(T_{pm} + T_s\right) \quad (4.13)^{15}$$

The heat loss due to forced and free convection is accounted by

$$h_w = 2.8 + 3.0\, v \quad (4.14)^{14}$$

$$h_{nat} = 1.78\left(T_{pm} - T_a\right)^{\frac{1}{3}} \quad (4.15)^{14}$$

$$h_c = \sqrt[3]{h_w^3 + h_{nat}^3} \quad (4.16)^{14}$$

Where v is the wind speed in m/s, h_w is forced convective heat transfer coefficient, h_{nat} is natural convective heat transfer coefficient and h_c is the overall convective heat transfer coefficient. The heat loss due to radiation is expressed in terms of sky temperature, mean absorber plate temperature and plate emissivity

Based on the data collected from National Ground Water Association (NGWA), the assumption is made on the inlet water temperature, and initial mean plate temperature.

$$T_{fm} = T_{fi} + \frac{Q_u / A_{rec}}{F_R U_L}\left(1 - F''\right) \quad (4.17)^{15}$$

$$T_{pm} = T_{fi} + \frac{Q_u / A_{rec}}{F_R U_L}\left(1 - F_R\right) \quad (4.18)^{15}$$

[14] Fudholi et al. 2014
[15] Duffie and Beckman

4.3: Thermal Storage Tank

It is known that solar energy is a time dependant energy source (Duffie and Beckman 2013). The energy demands of a residential building is independent of renewable energy supply. Furthermore, the patterns of the demand is dictated by the nature of the applications involved. Hence energy storage seems to be a viable solution to bridge the demand and supply mismatch. A storage tank helps store the excess energy generated during the day. Given that it may not be possible to meet all energy demands through the use of a storage tank, an additional heat source is needed depending on the season. This research work has utilised a forced circulation system to remove excess heat from the collector which is then stored in said tank.

The energy (Q) storage capacity of unstratified water storage system at uniform temperature which operates over a temperature difference of the storage tank (T_{st}) is given by

$$Q_{st} = (mC_p)_{st}\,\Delta T_{st} \qquad (4.19)^{15}$$

Energy balance equation on the unstratified tank

$$(mC_p)_{st}\frac{dT_{st}}{dt} = Q_u - L_s - (UA)_{st}(T_{st} - T_a') \qquad (4.20)^{15}$$

Euler integration is calculated on the above equation by rewriting the temperature derivatives as $(T_{st}^* - T_{st})/\Delta t$ and solving the mean temperature value of the tank at the end of every time increment

$$T_{st}^* = T_{st} + \frac{\Delta t}{(mC_p)_{st}}[Q_u - L_s - (UA)_{st}(T_{st} - T_a')] \qquad (4.21)^{15}$$

The energy is stored in the form of sensible heat where the temperature of the liquid is raised without the involvement of phase change. There are a number of parameters taken into consideration with respect to thermal storage system: the heat capacity of the liquid involved (water = 4190 J/kg K), the operating temperature range of the liquid, the method of heat addition or removal to the system, the stratification of the water storage tank, the additional power source to meet the demands, the size, shape, and structural aspects of storage tank.

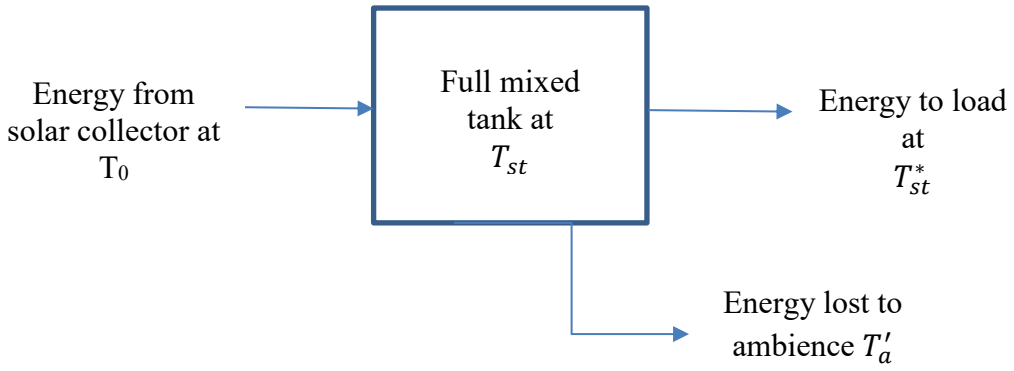

Figure 61: Unstratified water tank storage operating at temperature T_{st} in ambient condition

[15] Duffie and Beckman

5: Case Study

5.1: Background

A prototype house can help understand the needs and potential energy consumption of a residential house. Figure 65 depicts the floor plan for the considered model, a house located in USA. The living area of the chosen model is in par with both state and national average size of single family house, comprised of 2 stories and a basement. The model is a basic design which takes into account all necessary energy requirements such as: heating, cooling, lighting, cooking, appliances, and hot water.

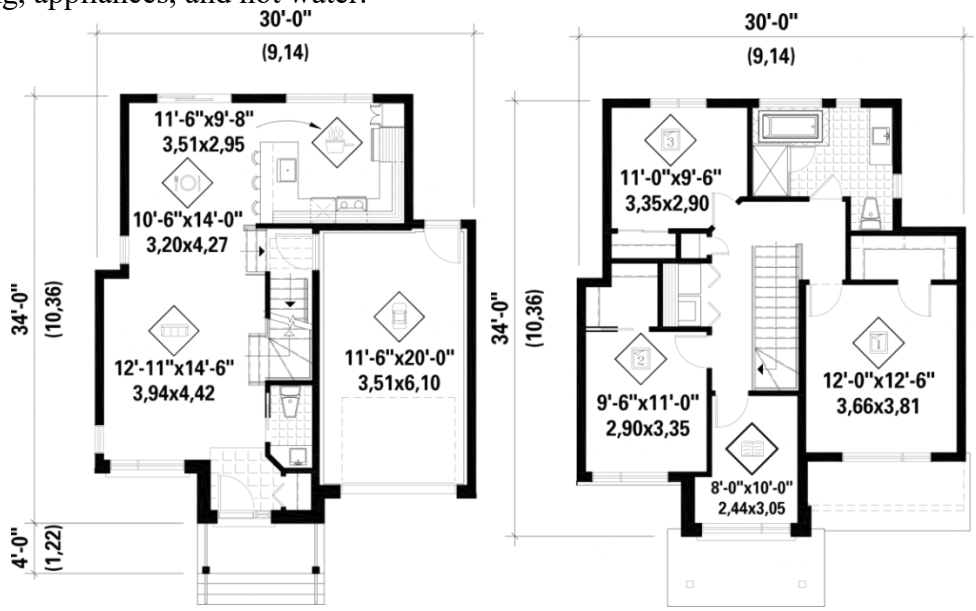

Ground floor *First floor*

Figure 62: The floor plans are courtesy of plan image architectural design services

5.2: Location Analysis

USA is ranked third largest country in the world with a wide variety of climates. Although this is a country with a wide range of climates, most of its geography falls under temperate or continental weathers (Kottek et al. 2006). As such, a location based on such a climate is chosen for the case study. Little Rock, Arkansas is a city located in the south central region of the USA. The location is known as humid subtropical under the Köppen–Geiger climate classification (Kottek et al. 2006). Figures 63, 64 and 65 illustrate the Direct Normal irradiance and average dry bulb temperature characteristics of Little Rock, Arkansas.

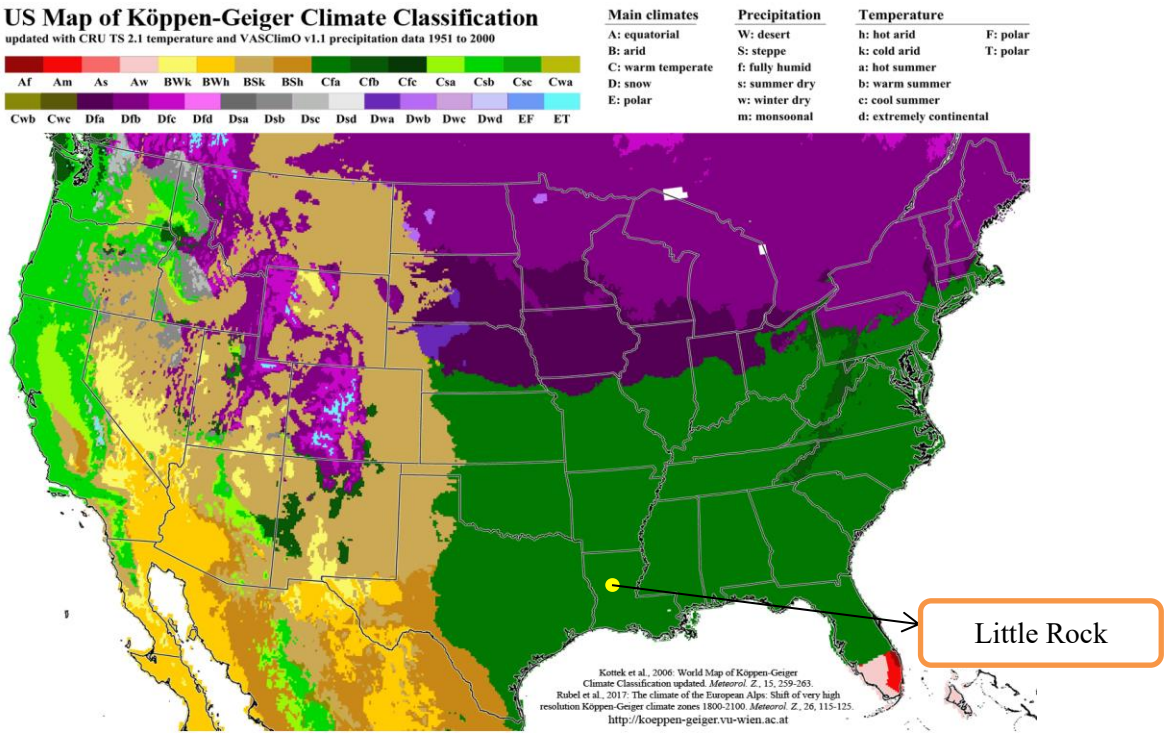

Figure 63: US Map of Köppen–Geiger Climate Classification (Kottek et al. 2006)

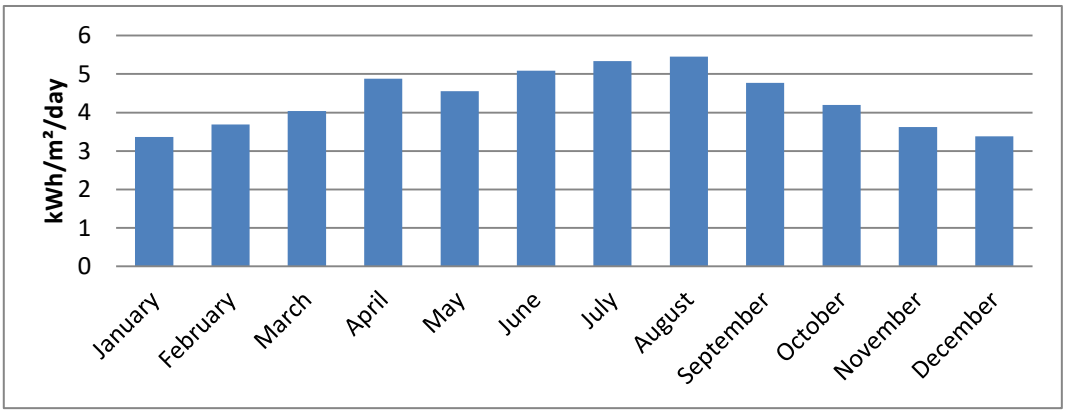

Figure 64: Direct Normal Irradiance of Little Rock, USA

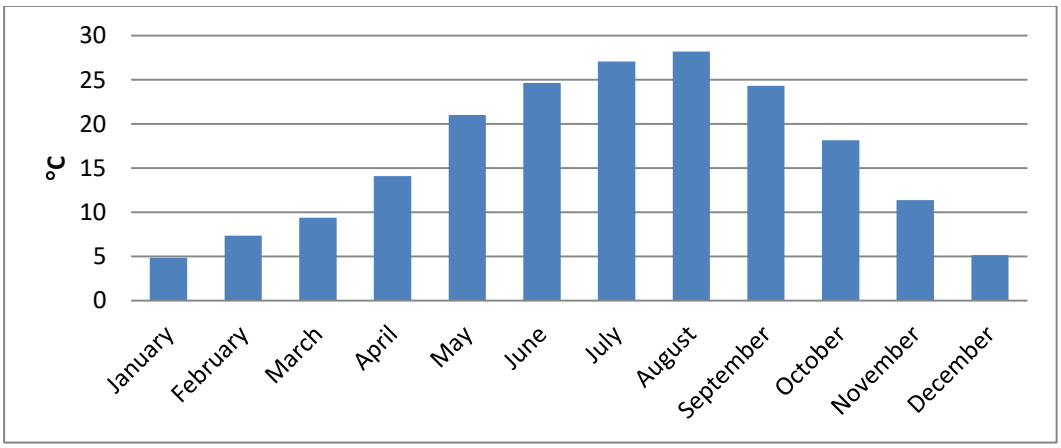

Figure 65: Dry Bulb Temperature of Little Rock, USA

5.3: Building Description

This sections deals with the 3D modelling of a low rise residential building which is subjected to energy simulations to determine the energy performance. Various parameters such as weather data, building envelopes, equipment, lighting, occupancy, ventilation etc., are taken into consideration to model the house in order to assess the energy demands. This assessment will help in determining the capacity of the heating, ventilation, and air conditioning (HVAC) systems used. The entire house is designed to suit the residential standards of Arkansas. (Neubauer and Nadel 2011). The report which is prepared by the ACEEE briefly gives insight about the various aspects based on the data collected from 18 single families in Arkansas. The measured parameters are estimated based on the average lifetime, savings and costs per home upon replacements of the products (Neubauer and Nadel 2011). According to the report, the average number of occupants is 3, with 1724 hours of occupancy duration in a day. Air leakage is set at 0.39% with a vented attic. The walls are constructed using bricks on the exterior layer with hardboard and fill insulation amounting to an R-value of less than 19, while the ceiling is set at 30. The windows used are Double pane in most houses. 52% of the residents use a furnace for heating with centralized air condition. 50% of the residents produce hot water using electricity, while the rest use a boiler. The ground floor of the house consists of a car parking, living/family room, dining area, and kitchen with a small restroom. The first floor has three bedrooms, one of which is the master bedroom. The house is also equipped with a basement.

5.4: Building Shell

Based on the available information on both state and national averages of house area, the average size of a residential building in determined to be 2100 ft^2 (reference). The house is oriented along the North-South direction. The floor plans are provided in Figure 65. The house is designed and simulated using eQuest 3.65. The ground floor covers a total area of 70.5 m^2 (759 ft^2), which consists of a car parking, hall, restroom, and a kitchen with dining space. The first floor covers a total area of 68.4 m^2 (736 ft^2), which consists of 3 bedrooms, a bathroom and a small reading room. The basement covers a total area of 49.1 m^2 (529 ft^2).

The floors above ground have components that are made up of 3 materials. The outside layer is a 16 inch wood frame combined with an interior insulation rated R-4, and an exterior insulation rated R-1.3. The basement is constructed with a 6 inch concrete with an insulation rated R-10 (Neubauer and Nadel 2011).

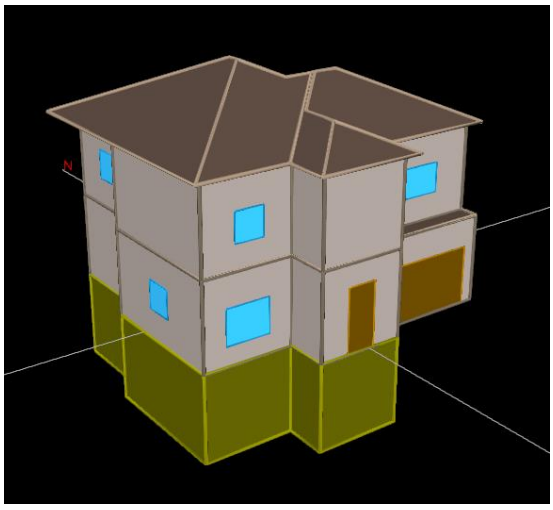

Figure 66: Prototype model developed and simulated in eQuest

5.5: HVAC Specification

The proposed research work uses a simple solar collector to remove excess heat generated by the system. This heat is transferred to the forced circulating water within the collector design. Hence, space heating is provided by hot water coils, and space cooling is provided by chilled water coil. The HVAC system is a 4-pipe fan coil with hot water heat. The thermostat setting is designed to cool the house when the temperature exceeds 76°F, and heats up the system when the temperature dips below 72°F. The water side HVAC system is connected to the thermal storage tank to reduce the electric consumption of electric hot water boiler. The chiller used in this eQuest model is an electric hermetic reciprocating compressor.

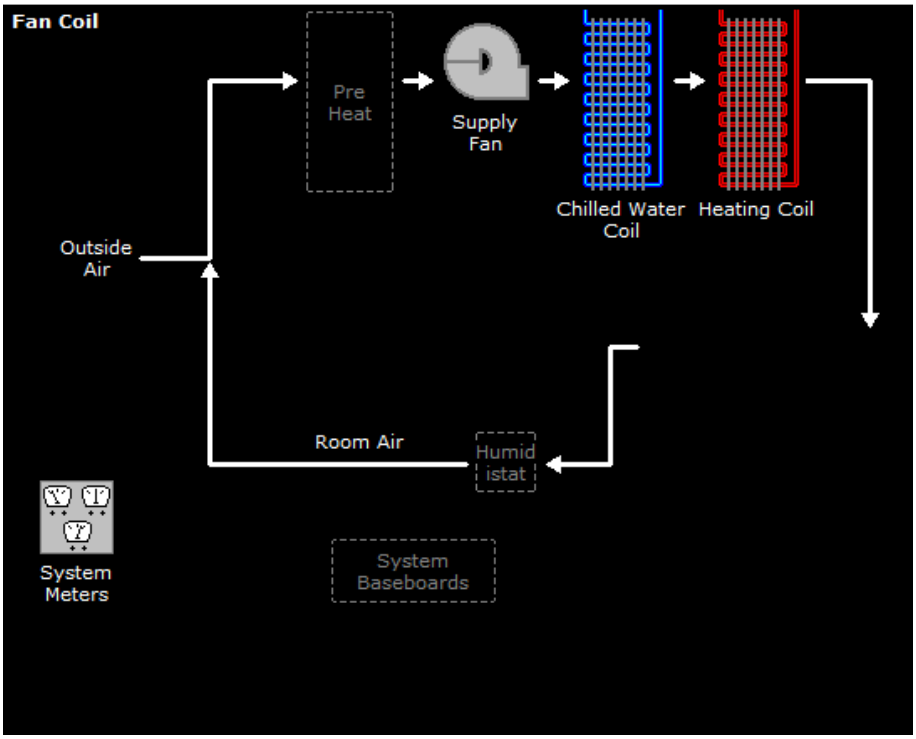

Figure 67: Air side HVAC system

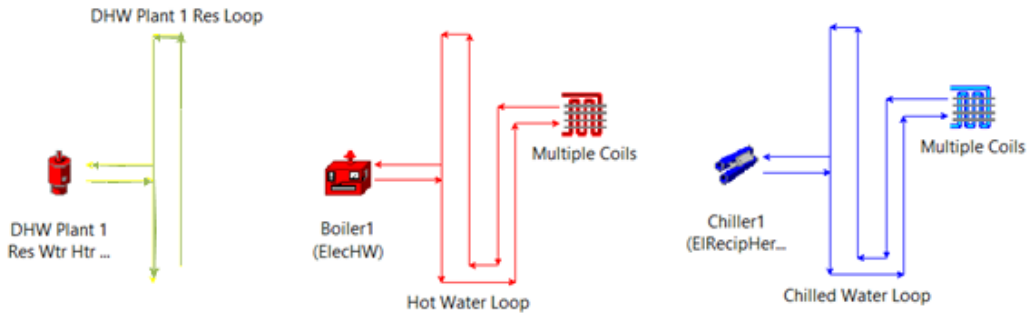

Figure 68: Water side HVAC system

5.6: Simulated Results

eQUEST generates reports for consumption loads which includes electric, space cooling, and space heating in both graphical, and tabular manners. It also provides hourly reports for the loads of the building simulation using the DOE-2 program. In the following section, monthly peak load and energy consumptions are discussed.

5.6.1: Input data to eQUEST

The eQuest helps in understanding the energy demand of a building. It takes into the consideration of the type of building and its location. It also provides us with seasonal description to understand the dynamic need of the house based on consumer practice.

The eQuest helped to design the building shell one floor at a time. The foot print shape of each floor is customised along with its zoning pattern. Floor heights are designed for 9 feet and the second floor has pitched roof. The building operating schedule is programmed for the consumer to leave house at 10 am and return at 4 pm during weekdays. It is also programmed to be open during weekends and holidays. The access to basement is closed during weekdays. The house is air conditioned centrally with an exception for garage. The interior end uses include cooking equipment, self-contained refrigeration and miscellaneous for other electronic gadgets. The interior lighting and miscellaneous loads are set to default for dwelling unit, conditioned storage and laundry.

5.6.2: Output data from eQUEST

The electric consumption and electric demand are shown for the designed residential building as shown in figures 69. The lighting load, miscellaneous load, ventilation equipment pumps and other auxiliary appliances are same throughout the year. The building operating schedule is fixed throughout the year without any change in seasonal requirement. It is observed that from the month of June to September the cooling consumption is predominant while the rest of the year has heating consumption. It is also observed that during peak winter there is a rise in heating demand.

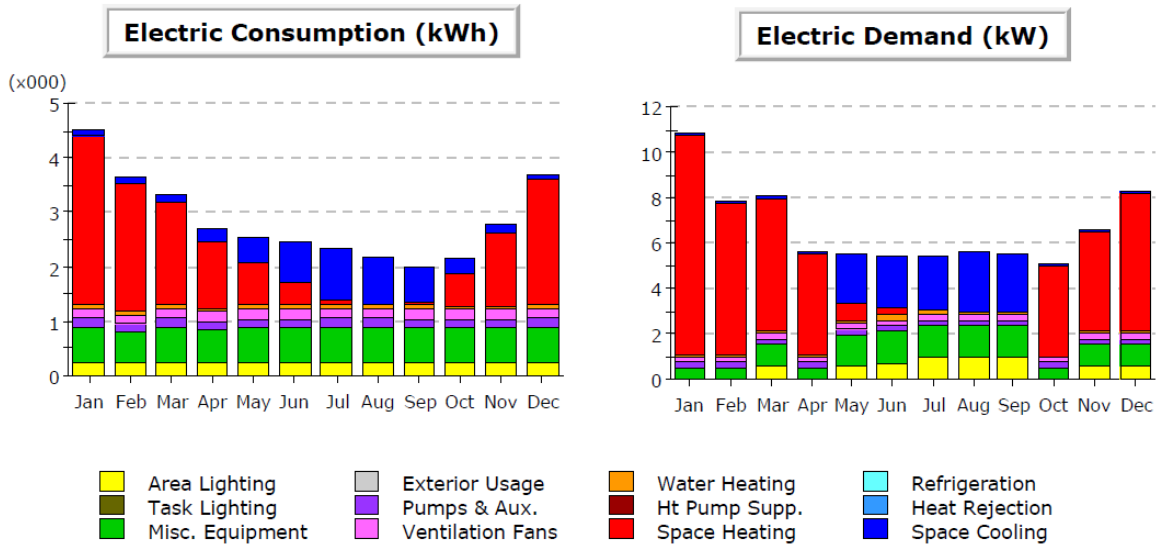

Figure 69: Bar chart: Peak demand and Energy consumption of prototype model

The total energy consumption of the residential building is 34,330 kWh. Figure 70 shows that the monthly energy consumption indicates that space heating accounts for 41% of the total consumption, while space cooling accounts for a mere 14%. The hot water consumption accounts for 820 kWh annually. The peak demand for cooling is observed in the month of august while peak demand for heating is observed in the month of December, as shown in figure 71.

	Jan	Feb	Mar	Apr	May	Jun	Jul	Aug	Sep	Oct	Nov	Dec	Total
Space Cool	0.10	0.10	0.17	0.27	0.46	0.73	0.96	0.86	0.64	0.28	0.15	0.11	4.83
Heat Reject.	-	-	-	-	-	-	-	-	-	-	-	-	-
Refrigeration	-	-	-	-	-	-	-	-	-	-	-	-	-
Space Heat	3.09	2.36	1.87	1.21	0.79	0.40	0.05	0.00	0.05	0.57	1.34	2.30	14.03
HP Supp.	-	-	-	-	-	-	-	-	-	-	-	-	-
Hot Water	0.07	0.06	0.07	0.06	0.06	0.09	0.08	0.08	0.07	0.05	0.05	0.06	0.82
Vent. Fans	0.18	0.16	0.18	0.18	0.18	0.18	0.18	0.18	0.18	0.18	0.18	0.18	2.15
Pumps & Aux.	0.18	0.16	0.18	0.18	0.18	0.18	0.18	0.18	0.18	0.18	0.18	0.18	2.13
Ext. Usage	-	-	-	-	-	-	-	-	-	-	-	-	-
Misc. Equip.	0.63	0.57	0.63	0.60	0.62	0.63	0.64	0.64	0.63	0.62	0.62	0.63	7.45
Task Lights	-	-	-	-	-	-	-	-	-	-	-	-	-
Area Lights	0.25	0.22	0.25	0.23	0.24	0.25	0.25	0.25	0.25	0.24	0.25	0.25	2.93
Total	4.51	3.65	3.35	2.72	2.54	2.45	2.34	2.19	1.99	2.13	2.77	3.71	34.33

Figure 70: Monthly energy consumption of prototype model (kWh X000)

	Jan	Feb	Mar	Apr	May	Jun	Jul	Aug	Sep	Oct	Nov	Dec	Total
Space Cool	0.12	0.12	0.12	0.12	2.18	2.28	2.41	2.65	2.55	0.12	0.12	0.12	12.95
Heat Reject.	-	-	-	-	-	-	-	-	-	-	-	-	-
Refrigeration	-	-	-	-	-	-	-	-	-	-	-	-	-
Space Heat	9.72	6.71	5.79	4.49	0.78	0.31	-	-	-	3.94	4.38	6.08	42.21
HP Supp.	-	-	-	-	-	-	-	-	-	-	-	-	-
Hot Water	0.03	0.03	0.14	0.03	0.10	0.29	0.21	0.14	0.14	0.02	0.09	0.12	1.34
Vent. Fans	0.24	0.24	0.24	0.24	0.24	0.24	0.24	0.24	0.24	0.24	0.24	0.24	2.94
Pumps & Aux.	0.24	0.24	0.24	0.24	0.24	0.24	0.24	0.24	0.24	0.24	0.24	0.24	2.92
Ext. Usage	-	-	-	-	-	-	-	-	-	-	-	-	-
Misc. Equip.	0.48	0.48	0.96	0.48	1.35	1.39	1.43	1.43	1.43	0.48	0.96	0.96	11.84
Task Lights	-	-	-	-	-	-	-	-	-	-	-	-	-
Area Lights	0.03	0.00	0.55	0.03	0.60	0.70	0.93	0.93	0.93	0.00	0.55	0.55	5.79
Total	10.87	7.83	8.06	5.64	5.51	5.47	5.46	5.63	5.53	5.07	6.60	8.32	79.98

Figure 71: Monthly peak demand by end use (kW)

6. Results

This section provides insight on the work carried over in the sub sections of the proposed CPV/T model. In order to do so, the proposed model is divided into three parts. The first part covers the results on various parameters of concentrators such as, ray trace methods, uniformity, ray trace results of approximation equation, effects of solar disc angle, design of collective reflector, and error function of the revised designs. The second part covers the results on working fluid temperature, thermal efficiency of the collector, effect of temperature on the solar module, and effect of solar radiation on the fluid temperature. The third part covers the supply and demand energy gap, and the effect of peak demand on the modelled house based on average size of location.

6.1: Ray trace on Reflectors

In order to understand the behaviour of the reflectors, two similar reflectors with spherical profile and paraboloidal profile are simulated. The simulations are carried out for different scenarios. Apart from these simulations, a comparison is made between theoretical single paraboloid entities of full magnitude with proposed collective entities.

6.1.1: Vertex approximation for profile selection of reflectors

This simulation is setup with rays that are incident along the horizontal axis of the reflector. The position of the reflector, the ray source and the receiver are parallel to each other. The front view of the setup can be seen in figure 72. A graph is plotted (figures 73 and 74) with the help of TracePro to understand the concentration variation on the surface of receiver with paraxial incident rays.

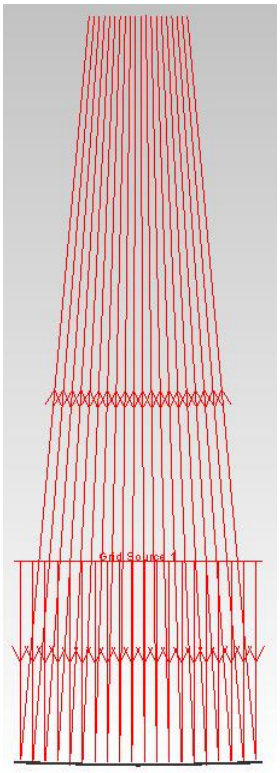

Figure 72: Paraxial rays incident on reflector

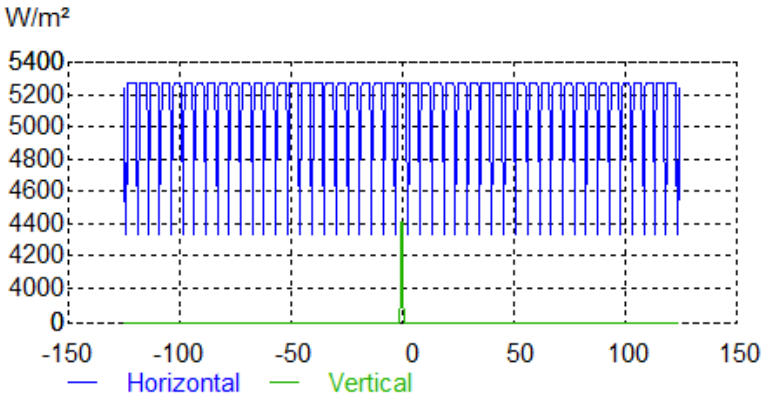

Figure 73: Concentrated rays on the receiver from a circular shape

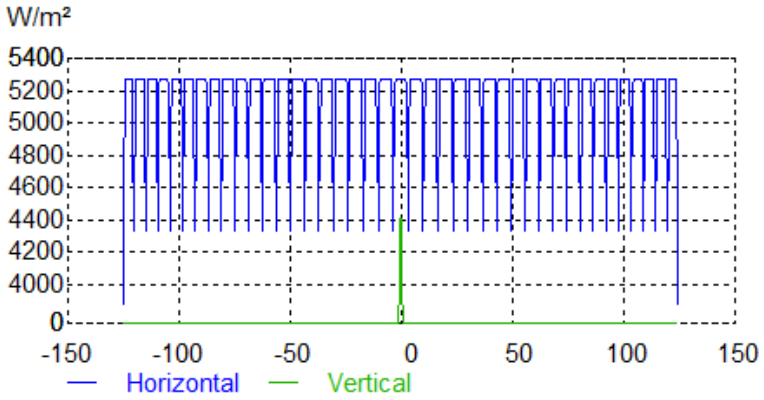

Figure 74: Concentrated rays on the receiver from a parabolic shape

The incident perpendicular rays concentrates the radiation along the same direction as the reflector. This reflects the previously demonstrated similarity between the circular and parabolic shape due to the near vertex approximation; the output of the circular profile reflector is identical to the output of the parabolic profile.

6.1.2: Effect of solar angular profile on single reflector

Firstly, the ray trace was carried out on single reflectors of magnitude 600 mm x 600 mm on both the profiles.

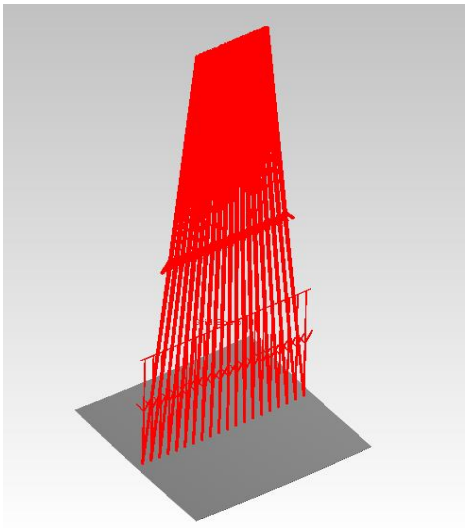

Figure 75: Solar angular profile rays incident on single reflector

The reflector is subjected to solar angular profile to replicate real time scenario. 1D incident radiation is considered to help understand the profile of the reflector. The selected irradiance is 1000 w/m^2.

Figure 76 demonstrates that the concentration peak achieved by spherical profile reflectors are higher compared to paraboloid profiles. This indicates that paraboloid profiles have better uniformity compared to its former part, despite the fact that both reflectors are designed for the same concentration ratio.

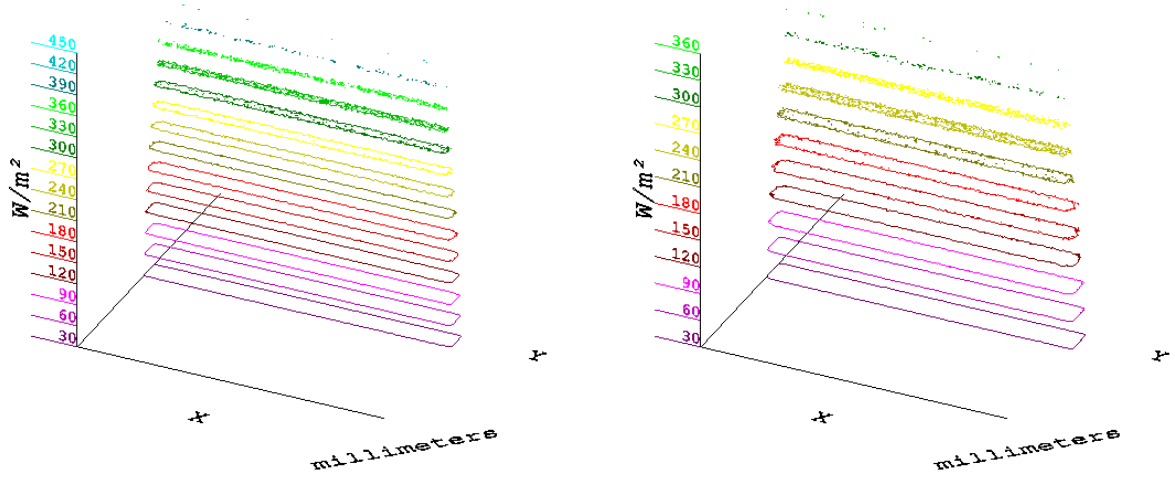

(a) *(b)*

Figure 76: Contour graphs of concentrated rays for (a) spherical and (b) paraboloidal profiles

Secondly, the incident radiation is focused on the reflector along x-y axis. The total surface of the reflector is subjected to incident radiation. This setup helps understand the concentration factor of solar radiation on the receiver with respect to its profile. Figure 77 demonstrates that flux concentration is almost identical in spherical and paraboloidal reflectors as previously discussed. The incident radiation is set to 1000 W/m^2 falling on the reflector of 600 mm x 600 mm. The difference in flux concentration is less than 3 watts and the performance is almost identical.

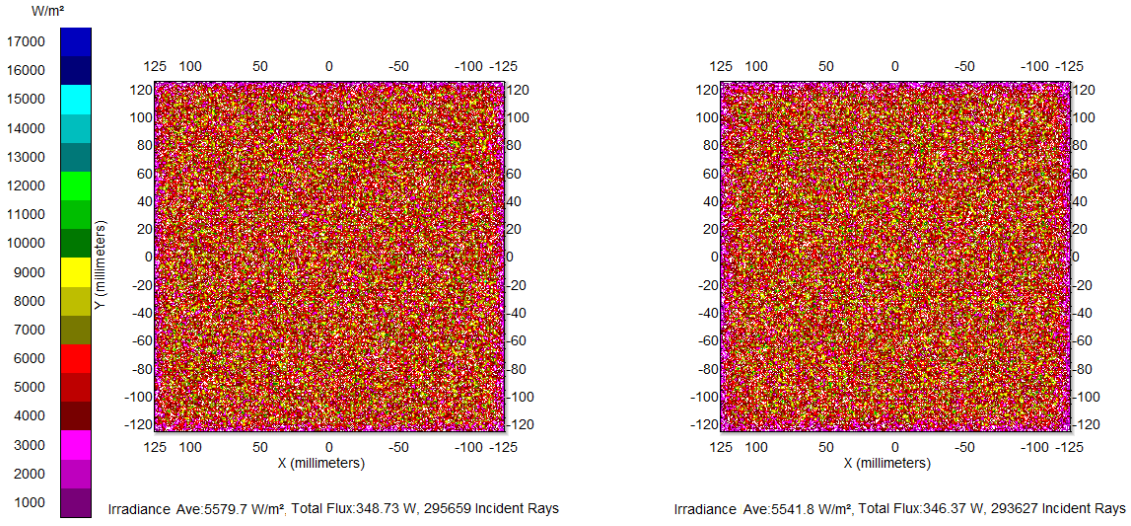

(a) *(b)*

Figure 77: Concentrated rays of (a) spherical and (b) paraboloidal profile

6.1.3: Collective Reflector

The performance characteristics of a single reflector and its spherical profile have been established, which in turn facilitates the desired design process. However, the complexity of this design has been elaborated in previous sections. In this research, the assembly of 60 spherical profile reflectors of dimensions 600 mm x 600 mm and 4 spherical profile reflectors of dimensions 240 mm x 240 mm are called the collective reflector entity. The collective reflector entity design, as seen in figure 78, is governed by various factors such as the optical efficiency of the system, the uniformity of concentrated solar irradiation, the manufacturability, the stability, the robustness, and the reflectivity losses.

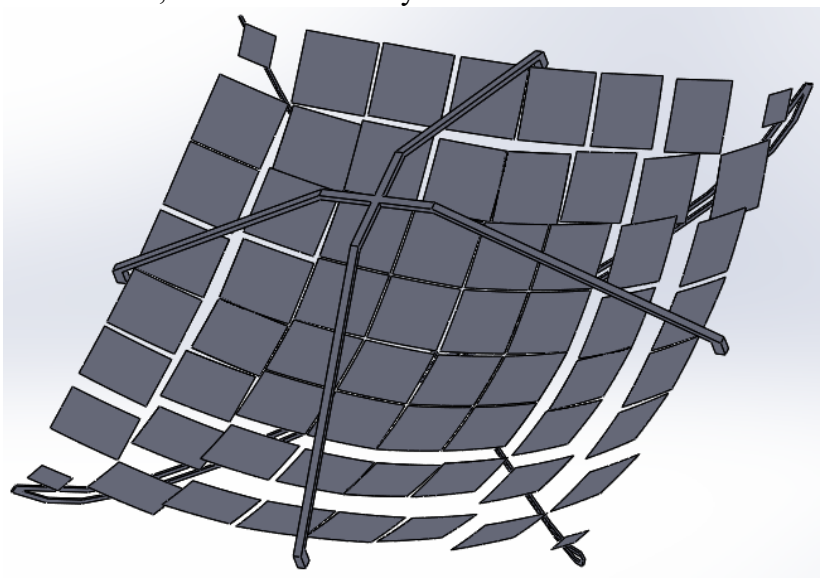

Figure 78: Conceptualized base reflector construction support

The spherical profile reflector are coated with Polyethylene Terephthalate or commonly called as polyester films. These films have the advantage of reflectivity as much as 94% across the full spectrum. Reflectivity across full spectrum is required as the efficiency of MJSC is high compared to other commercially available solar cells, due to its capacity to convert a higher spectrum range of solar radiation.

The construction of the system has taken into account the receiver in order to avoid structural losses further to the above mentioned losses. The system also has better stability as the receiver is placed at a height of 1750 mm from the base reflector (figure 79), unlike flat mirrors (Chong, Kok-Keong et al. 2017), where the stability of the system is compromised to accommodate the geometric concentration ratio.

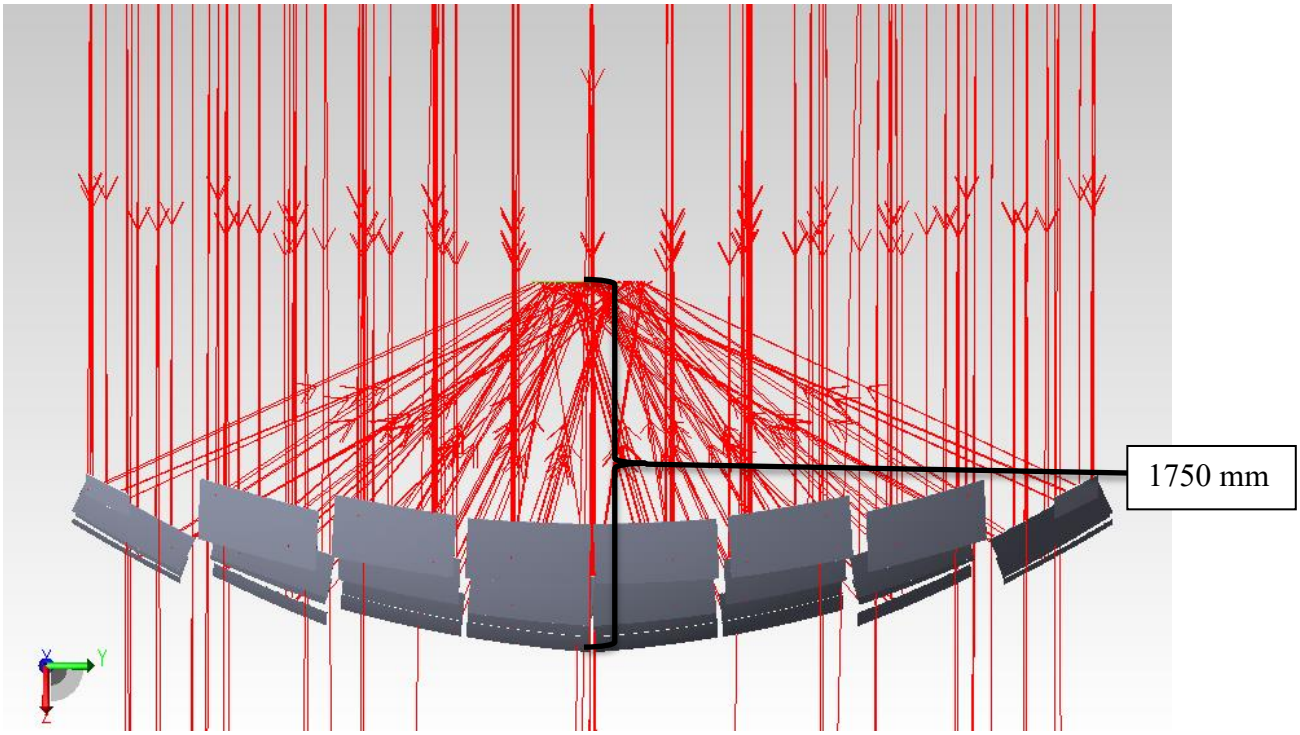

Figure 79: Schematic representation of ray trace on the entire assembly

6.2: Uniformity Analysis of Concentrated Solar Irradiation

In order to achieve maximum output from the solar cells, the uniformity of the solar radiation is of vital importance (Benítez et al. 2010) (Pan et al. 2011). The uniformity of solar radiation on the receiver surface is mathematically modelled using the ray trace technique which has previously been discussed in detail. To achieve this status, the base reflector design needs to be optimized based on focal length-radius of curvature ratio. The optimal focal length is calculated to maximise concentration factor without compromising the uniformity of solar radiation. In this research, the design process has undergone a series of iterations out of which the 3 major stages of iterations are discussed in detail below.

6.2.1: Design iteration 1

In the first design phase, the system is established with one paraboloid reflector of a 25 m^2 surface area. This setup is divided into 64 equal sizes symmetrically along horizontal and vertical axis. Hence this symmetrical split can be grouped into 4 parts. These 4 parts represents each quadrant and are identical to one another. The symmetrical concept is extended to the receiver. Thus the receiver is also split into 4 parts and corresponds to its reflector quadrant.

The sizes of MJSCs are around 4 cm^2. Thus the receiver is designed as shown in figure 80. The (i, j) represents the position of the MJSC locally.

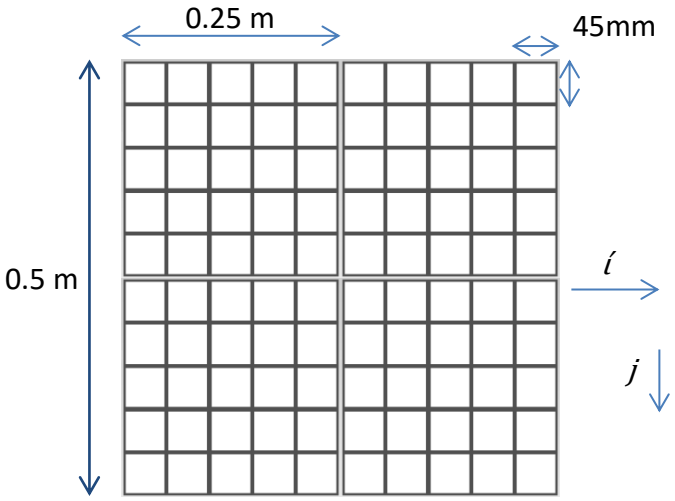

Figure 80: Receiver with MJSC (45mm x 45mm)

The concentrated solar radiation falling on the receiver is modelled as seen in figure 81. The degree of uniformity (UF) can be expressed in terms of concentration factor. It is the ratio between system concentrations to local concentration.

$$UF = \frac{C_g}{\sum_{i=1,j=1}^{i=10,j=10}(C_{i,j}-C_{avg})^2 \Big/ i \,.\, j}$$

(6.1)[14]

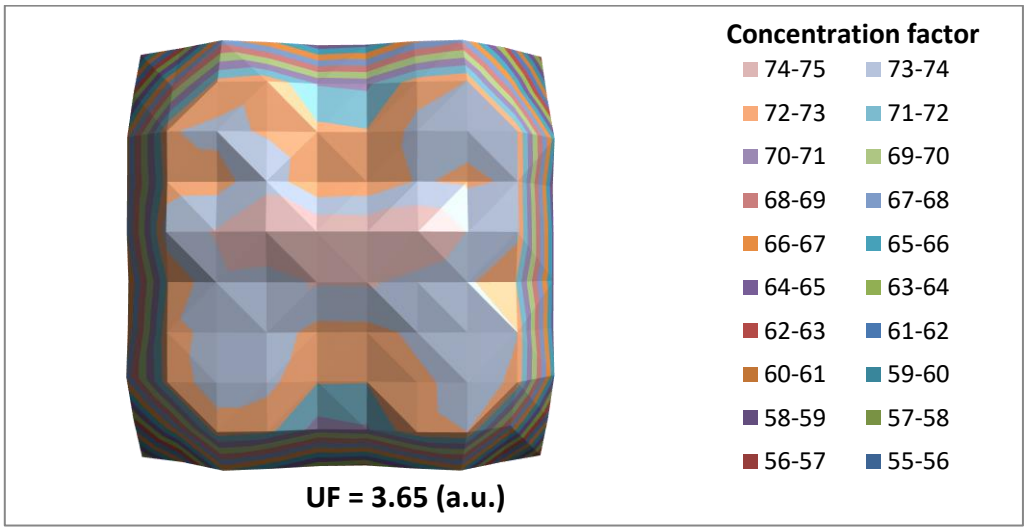

Figure 81: Concentrated solar irradiation distribution on the receiver (W/m^2)

Based on the mathematical modelling established in the methodology section, the focal length – radius of the reflector are determined. A graph is plotted (figure 82) to understand the design implications with respect to its true value. The displacement error of reflector position based on focal length-radius ratio is calculated.

[14] Pan et al. 2011

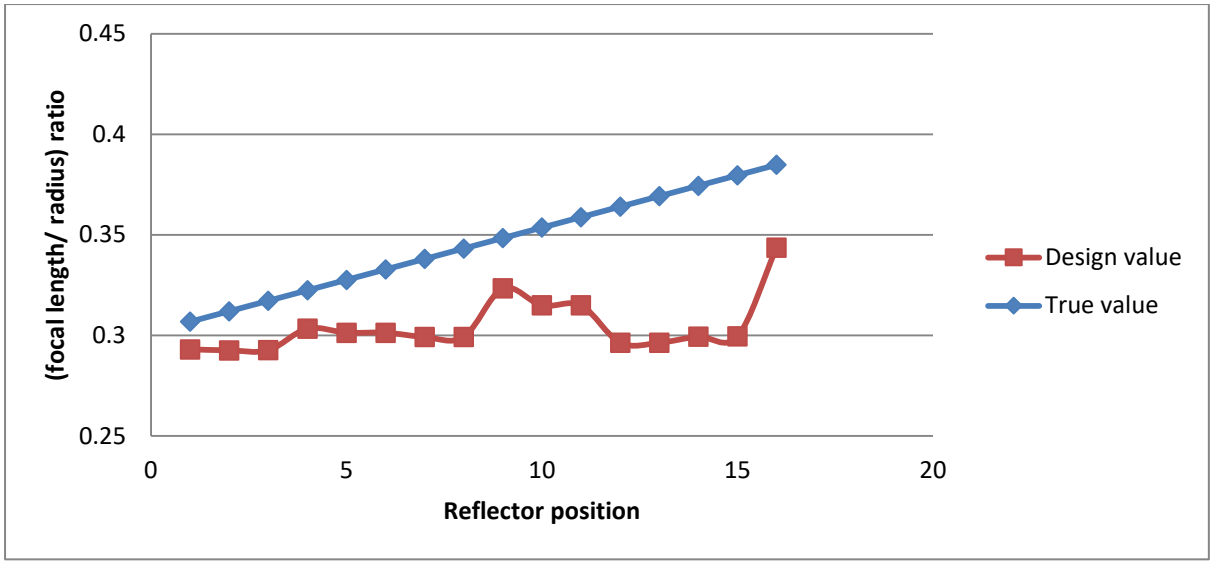

Figure 82: Displacement error based on position: iteration 1

6.2.2: Design iteration 2

In the second design phase, the system is made more flexible. Quadrant constraint on the reflector position has been removed. This gives rise to new set of design strategy. The mathematical model for this setup has been discussed in detail in the methodology chapter. The revised collective reflector design is plotted for concentrated solar irradiation on the receiver; a significant improvement in the uniformity factor is observed in figure 83.

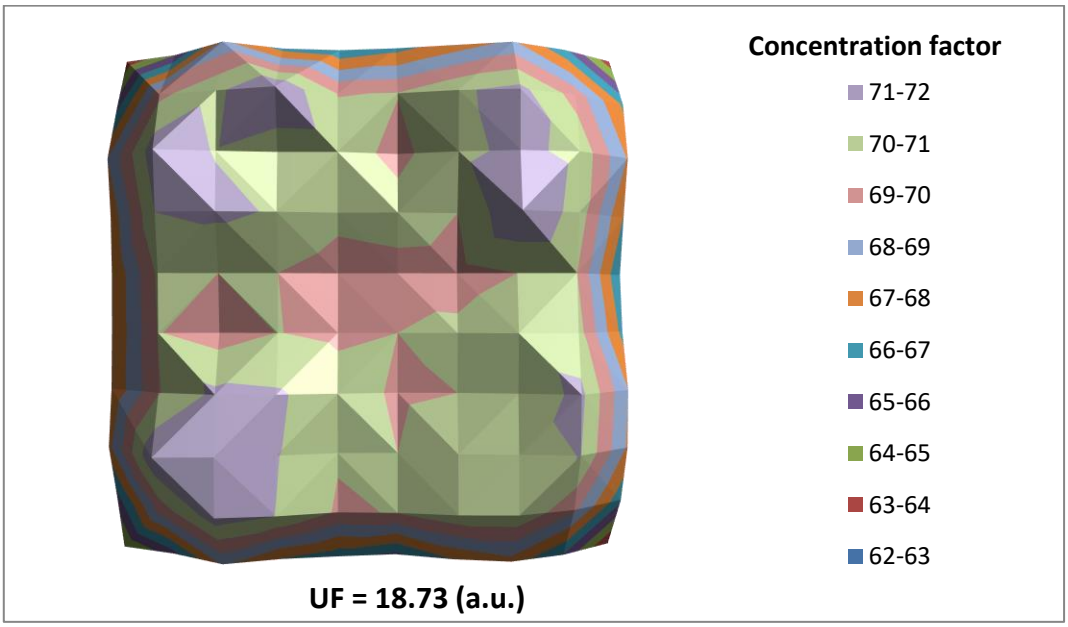

Figure 83: Concentrated solar irradiation distribution on the receiver (W/m^2)

Based on the mathematical modelling established in the methodology section, the focal length – radius of the reflector are determined for this iteration. A graph is plotted (figure 84) to understand the design implications with respect to its true value. The displacement error of reflector position based on focal length-radius ratio is recalculated.

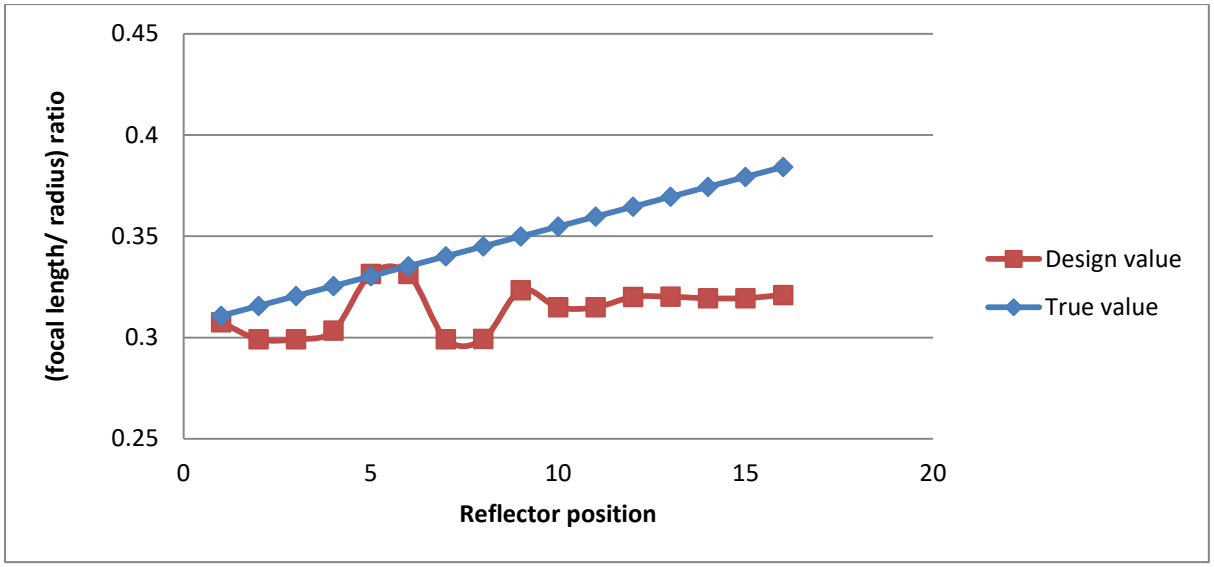

Figure 84: Displacement error based on position: iteration 2

6.2.3: Design iteration 3

In the third design phase, the corner reflectors are realigned to focus radiation to the corners of the receiver. Thus the reflectors that are located in the inner most circle are positioned to focus radiation to the diagonally opposite quadrant of the receiver. With the new design approach, the concentrated solar irradiation on the receiver is mapped out as shown in figure 85; a slight improvement in uniformity can be observed.

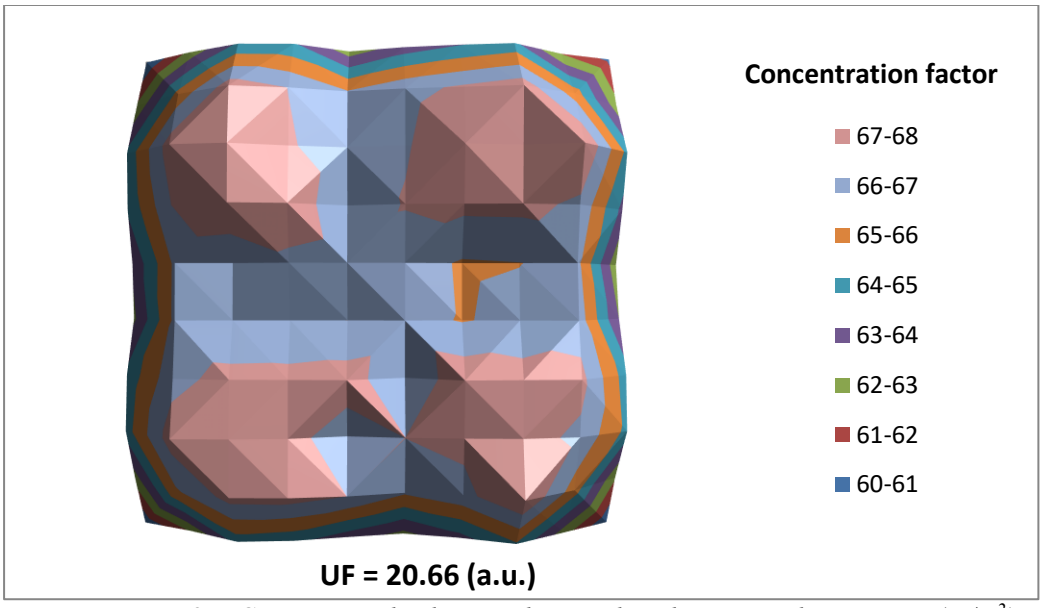

Figure 85: Concentrated solar irradiation distribution on the receiver (W/m^2)

Based on the mathematical modelling established in the methodology section, the focal length – radius of the reflector are determined for this iteration. A graph is plotted (figure 86) to understand the design implications with respect to its true value. The displacement error of reflector position based on focal length-radius ratio is recalculated.

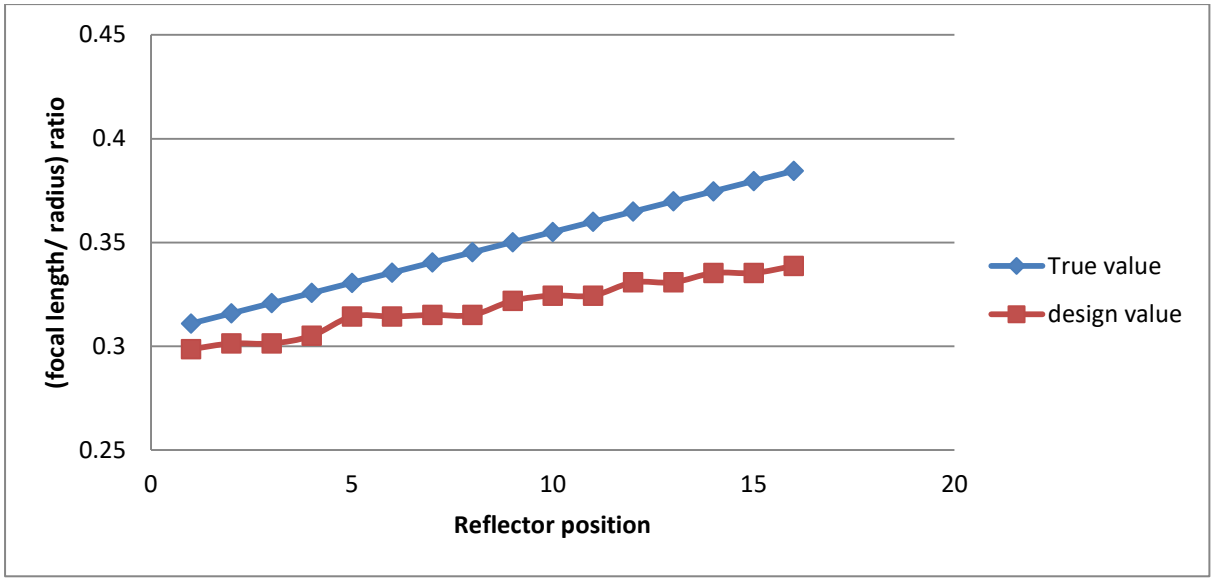

Figure 86: Displacement error based on position: iteration 3

6.3: Output data

The proposed collective reflector entity is subjected to 900 W/ m^2 on its 60 + 4 spherical profile reflectors, which is coated with polyester films that possess about 94% reflectivity. The proposed design is able to achieve a uniformity factor of 20.66 as discussed above. The simulation is performed on the third iterative design module with above specifications through the TracePro software. Through the optics software, the collective reflector entity is exposed to 3232571 rays, out of which 2330004 rays are reflected towards the receiver.

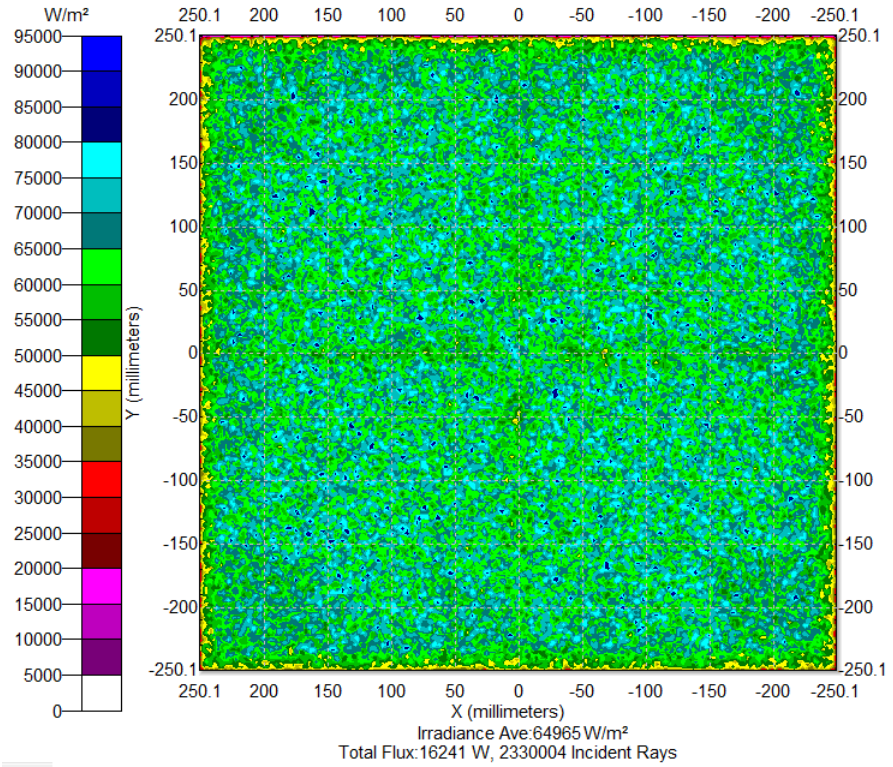

Figure 87: Concentrated solar irradiation on the receiver surface

Total incident radiation on reflectors	19440 W @ 900 W/m^2
Optical efficiency of concentrator	83%
Reflectivity of spherical mirrors	94 %
Theoretical incident radiation on receiver	16241 W
Actual incident radiation on receiver	15275 W

Another graph is generated using TracePro to understand the uniformity of concentrated solar irradiation on the receiver surface. Figure 88 shows the graph which comprises of a comparison between paraboloid mirror setup and third iterative design setup. The proposed design takes into the consideration of shading effect of receiver. The paraboloid mirror setup design, although has higher output, lacks uniformity, and cannot be used for concentrated photovoltaic technologies.

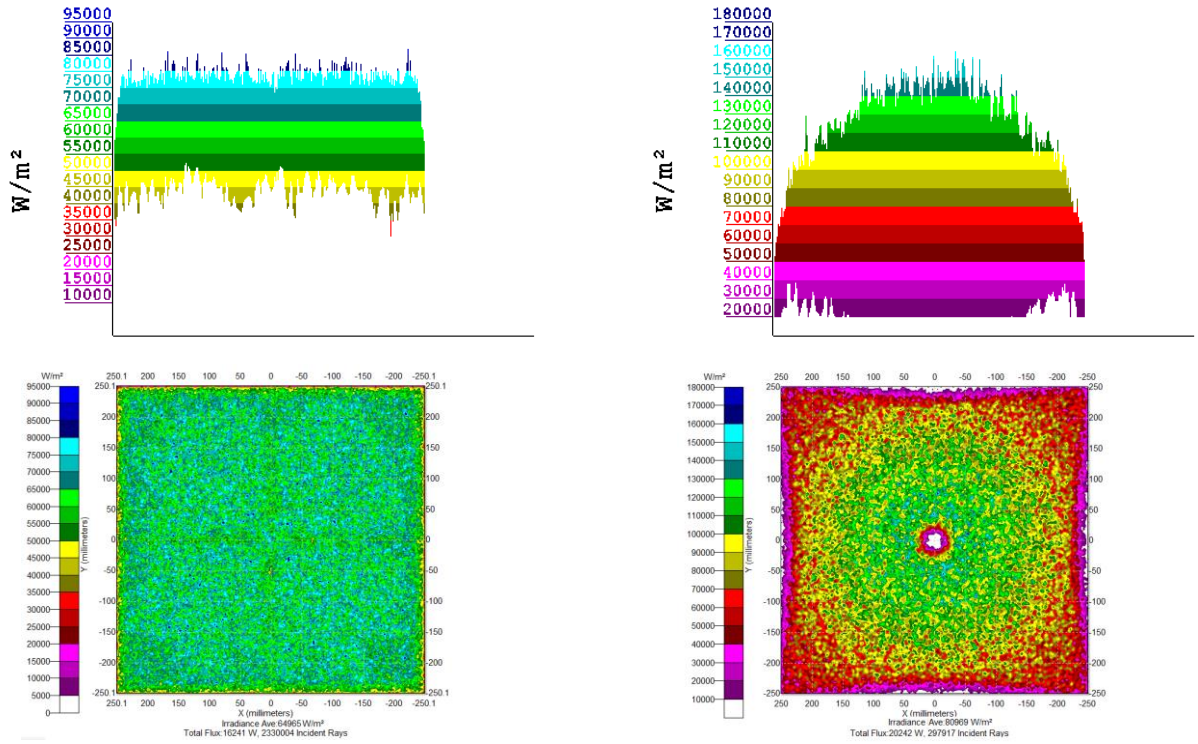

(a) Proposed design *(b) Paraboloid design*

Figure 88: Comparison between concentrated solar irradiation on the receiver for the (a) proposed design vs the (b) paraboloid design

6.4: Assumptions made in optics modelling

The following assumptions were made in the optics section of the proposed model.

- The placement of the mirrors are not governed by structural assembly (i.e) clamps are not utilised in the assembly of 64 mirrors
- Zero manufacturing error is assumed on the spherical mirrors; however in real time conditions, manufacturing defect can lead to loss of radiation convergence.
- Reflectivity loss of mirrors are assumed to be same throughout the assembly

- The Receiver material is assumed to be a perfect absorber.
- The simulation is carried over a single wavelength (546.1 nanometer)

6.5: Thermal Modelling

The incident solar radiation is concentrated on the receiver and the receiver is fitted with water collector coupled with MJSC. The suitable solar cell for this design is GaInP/GaAs/InGaAs or GaInP/GaAs//Si. The working temperatures of these cells are up to 100ºC. The efficiency at maximum power of this concentrated photovoltaic is around 30%. The system works at higher efficiency for collector model due to the concentrated solar input. It is also a known fact that heat loss coefficients are much smaller in case of concentrating collectors as the factors are inversely proportional to the concentration ratio. The thermal efficiency of the system is about 50% depending on the flow rate of the water.

6.5.1: Effect of CPV plate temperature on the solar collector

Figure 89 is a graph which indicates the analytical results of the solar thermal collector after getting exposed to solar irradiation ranging from 400 – 900 W/m^2 at 0.1 – 0.25 kg/s mass flow rates. The concentration of solar irradiation provided by the optics design is 65.5, which results in the intensity ranging from 24 kW/m^2 – 40 kW/m^2. The results show that CPV absorber plate temperature significantly depends on the mass flow rate of the water. Increased mass flow rates decreases the CPV absorber plate temperature. It is also observed that, at same mass flow rate, the temperature increased with increase to solar radiation levels.

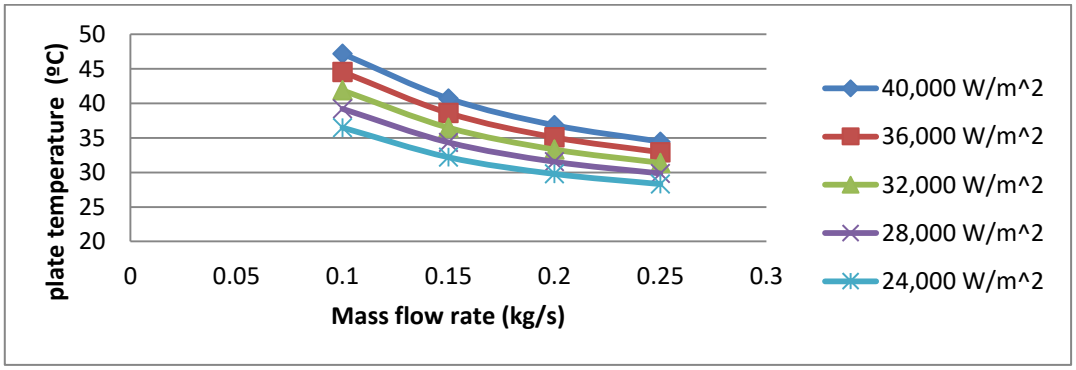

Figure 89: Change in CPV absorber plate temperature with different mass flow rates

6.5.2: Effect of STC water outlet temperature on the solar collector

The below graph indicates the analysis results of solar thermal collector after getting exposed to solar irradiation ranging from 400 – 900 W/m^2 at 0.1 – 0.25 kg/s mass flow rates. The results show that STC water outlet temperature depends on the mass flow rate of the water. With increased mass flow rate of water, it is observed that the outlet temperature of water is decreased. The outlet temperature also depends on the intensity of the solar radiation. The inlet water temperature is considered as 17.7°C. Steady state analysis of collector design is performed (see appendices) and the graph is plotted (figure 90).

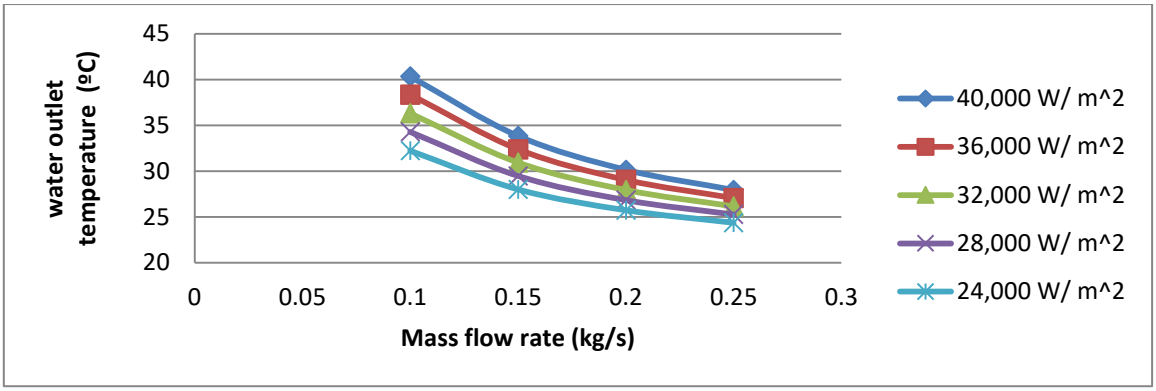

Figure 90: Change in outlet water temperature with different mass flow rates

6.5.3: Thermal performance of STC

Figure 91 is of a graph which indicates that the thermal performance of the collector after excess heat is available for collector through CPV setup. It is observed that there is increase in collector efficiency as mass flow rate is increased. The overall efficiency is not affected by much, which indicates losses incurred in concentrated collectors are very minimal.

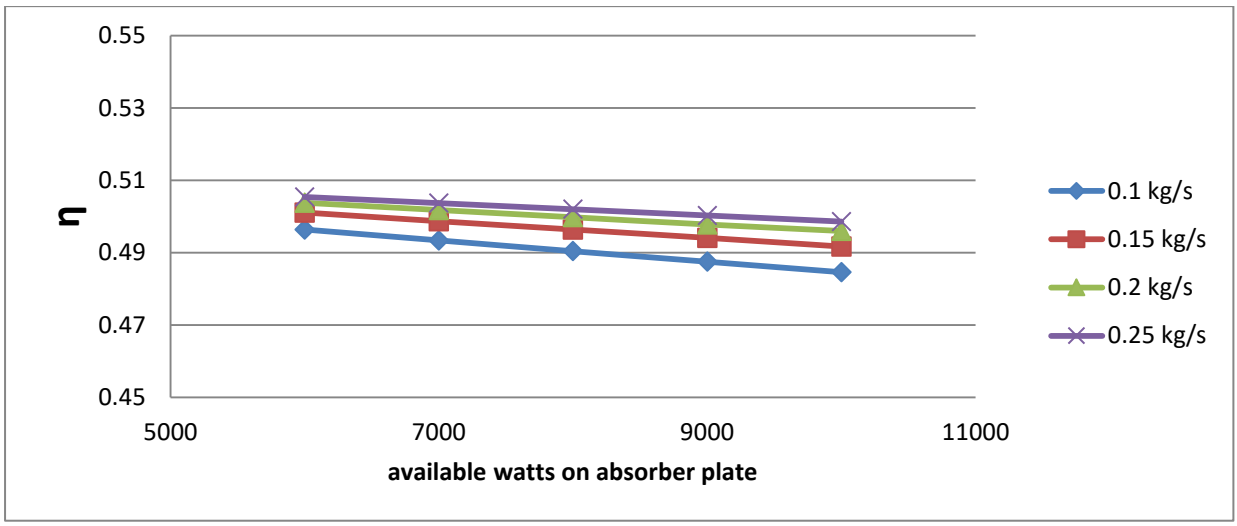

Figure 91: Thermal efficiency of collector

6.5.4: Energy balance on a Storage tank

Water is known as the best material used to store sensible heat. Energy from collector can be added to it or energy can be removed from it for domestic purposes. A tank is used as a storage medium, which is filled with water. The water is forced circulated from the collector through a pump, and their results were observed in the previous section. The water tank considered for the thermal design has storage capacity of 1500 L. A simple energy balance on the tank is performed in a time dependant scenario.

The input energy to the tank is calculated using the collector thermal efficiency and available energy from the collector. The energy required by the residential building is provided by the hourly reports of eQuest. It includes domestic hot water demands, and hot water for the hot water coils used for space heating. This energy is the same energy that will be removed from the storage tank. The heat loss coefficient for the storage tank is assumed to be 1.5 W/m^2K. The temperature of water tank is maintained at 50°C. The graph is plotted for 6

scenarios which include 2 equinoxes, 2 solstices, the hottest, and the coldest days of the year in Little Rock, USA in 2019.

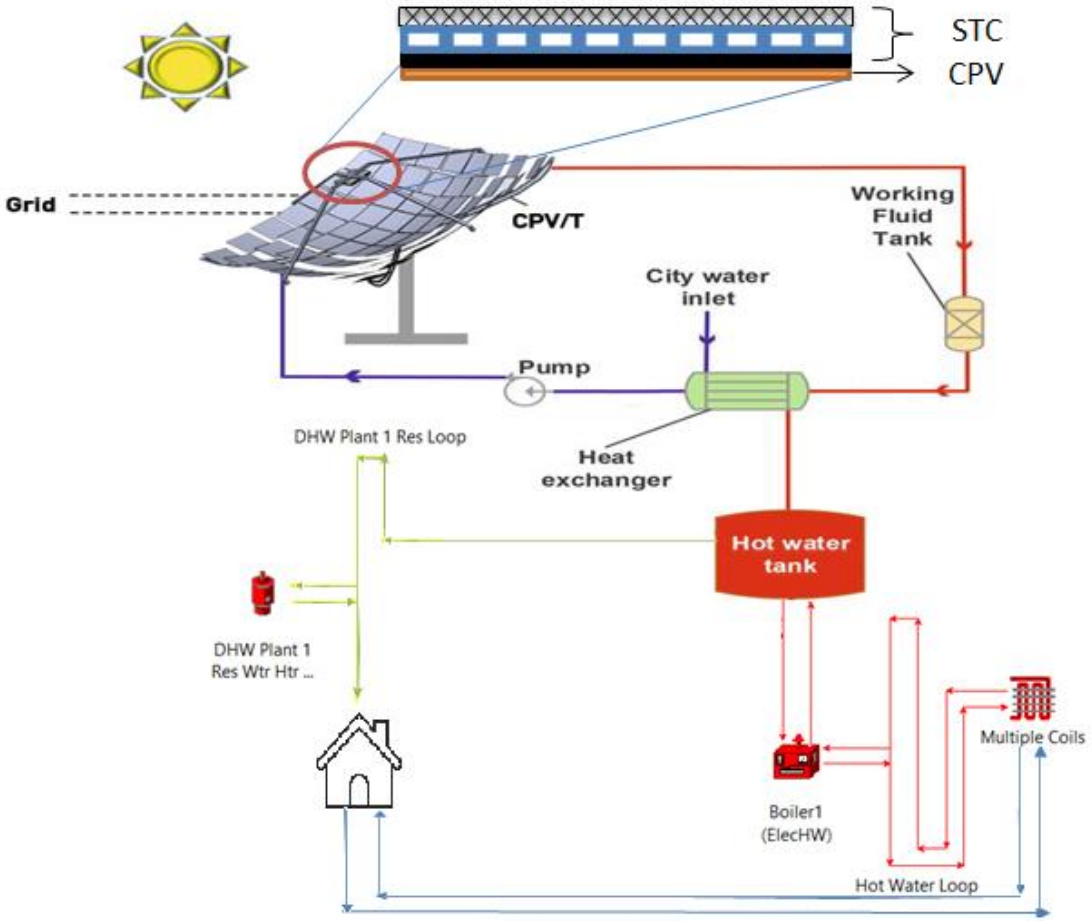

Figure 92: Integration of proposed model with the residential building

On the coldest day, the water temperature in the tank (T_{st}) goes as low as 24°C before the scheduled operation of the proposed system as shown in figure 92. The proposed system is scheduled to operate between 0900 hours and 1500 hours. The temperature in the water tank never exceeds the initial set temperature of 50°C regardless of the amount of energy focused on the solar collector (Qu) and the heat removed from the storage tank (L`s).

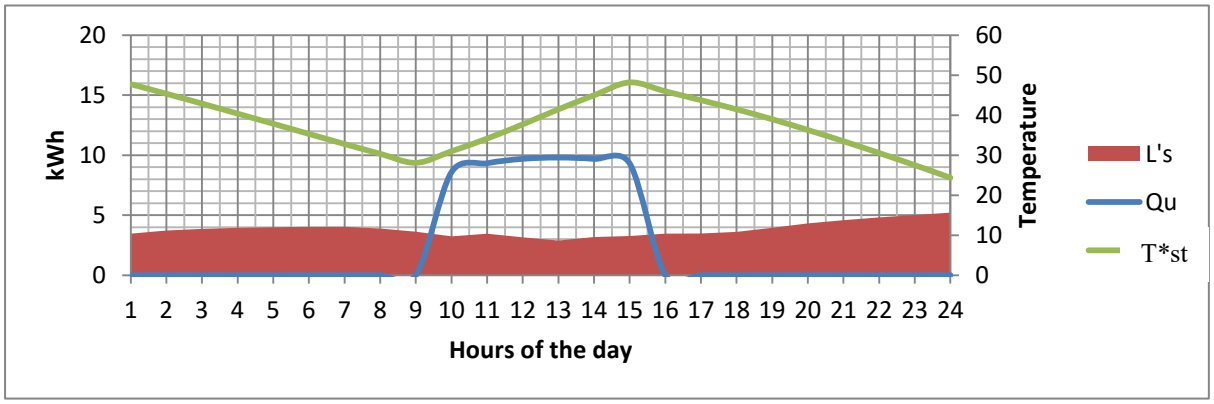

Figure 93: Energy balance equation on March 4th, 2019 – coldest day

On spring equinox, the water temperature in the tank goes as low as 23°C before the scheduled operation of the proposed system. The proposed system is scheduled to operate between 0900 hours and 1500 hours. The temperature in the water tank never exceeds the initial set temperature of 50°C.

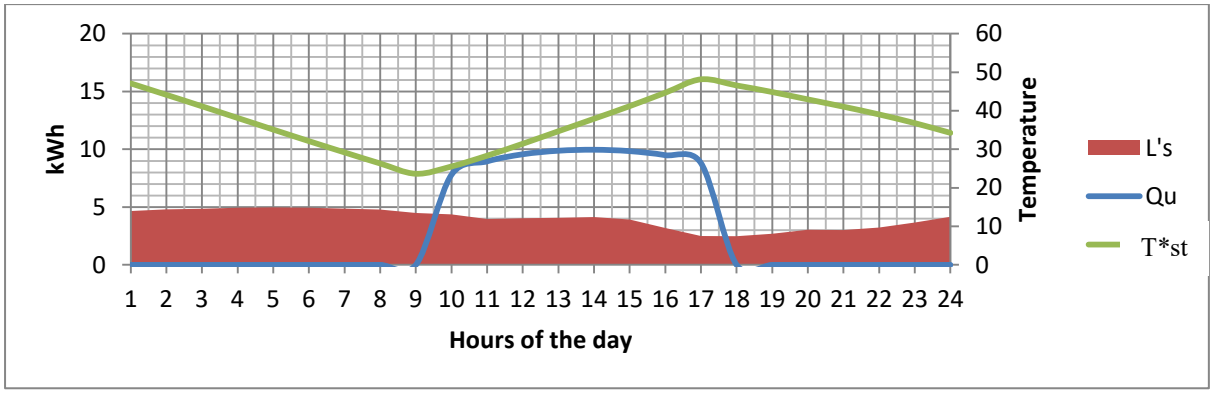

Figure 94: Energy balance equation on March 19th, 2019 – spring equinox

On summer solstice, the water temperature in the tank goes as low as 36°C before the scheduled operation of the proposed system. The proposed system is scheduled to operate between 0900 hours and 1700 hours. The temperature in the water tank exceeds the initial set temperature to 67°C. This is due to the reduced demand of heat energy and increased supply during the summer season.

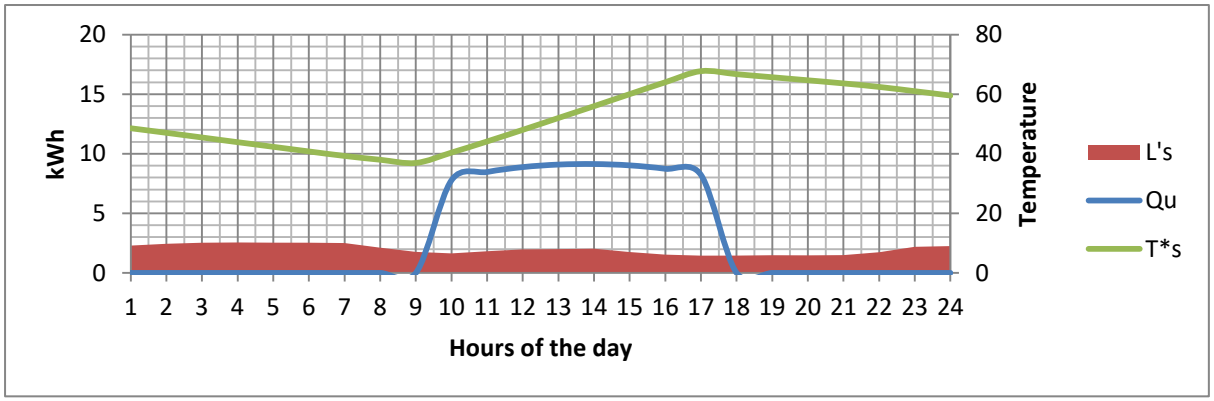

Figure 95: Energy balance equation on June 21st, 2019 – summer solstice

Figure 95 demonstrates that on the hottest day, the water temperature in the tank goes as low as 38°C before the scheduled operation of the proposed system. The proposed system is scheduled to operate between 0900 hours and 1700 hours. The temperature in the water tank exceeds the initial set temperature to 71°C. This is due to the reduced demand of heat energy and increased supply during the summer season.

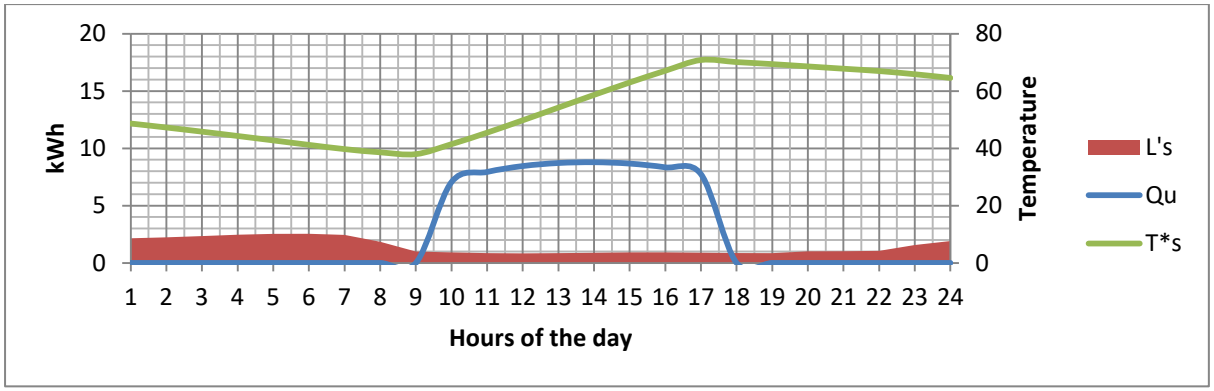

Figure 96: Energy balance equation on August 13th, 2019 – hottest day

On fall equinox, the water temperature in the tank goes as low as 36°C before the scheduled operation of the proposed system. The proposed system is scheduled to operate between 0900 hours and 1700 hours. The temperature in the water tank exceeds the initial set temperature to 69°C. This is due to the reduced demand of heat energy and increased supply during the fall season.

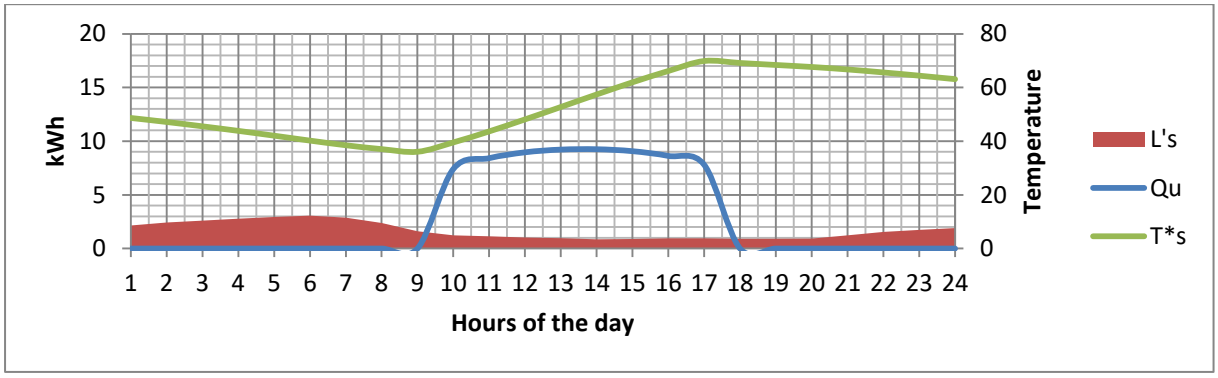

Figure 97: Energy balance equation on September 23rd, 2019 – fall equinox

Figure 97 demonstrates that on winter solstice, the water temperature in the tank goes as low as 2°C during the night. The proposed system is scheduled to operate between 0900 hours and 1500 hours. The temperature in the water tank never exceeds the initial set temperature of 50°C. The demand of heat energy is high and supply is low during the winter season.

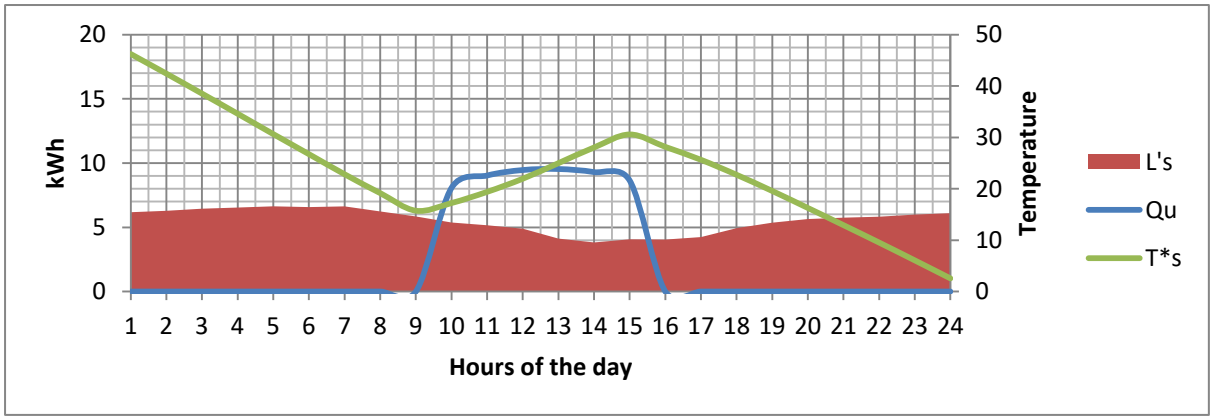

Figure 98: Energy balance equation on December 21st, 2019 – winter solstice

Thus heat energy demand is met by the proposed system except during the winter season, implying the proposed system can help achieve a near zero energy in terms of heat energy requirements.

6.6: Energy demand – supply curve

To understand how the proposed system will enhance a residential house in terms of energy consumption, graphs are plotted. The output data from eQUEST is used to map out the energy consumption for the day. The potential energy supplied to the CPV is calculated through TracePro. The efficiency of the CPV is assumed to be at its highest. Entergy the energy company that is responsible for the electric power production in Arkansas also allows net metering during daytime without any difference in tariff.[16] This is beneficial in utilizing the produced energy when needed.

The proposed system provides 27% of the daily need during the coldest day of the year as shown in figure 98. The hours of operation considered during this day is from 0900 hours to 1500 hours

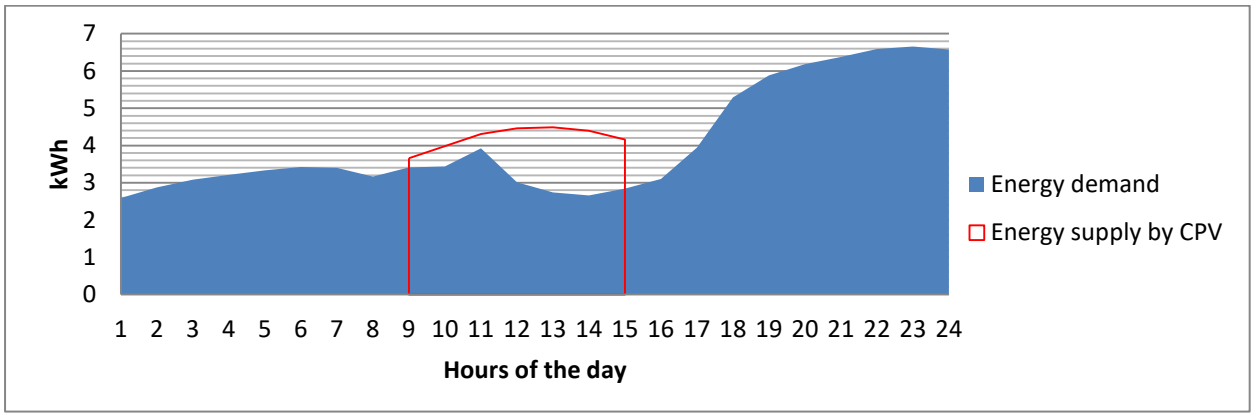

Figure 99: Demand vs Supply on March 4th, 2019 – coldest day

During the spring equinox, the system provides 26% of the daily need. The hours of operation considered during this day is from 0800 hours to 1600 hours

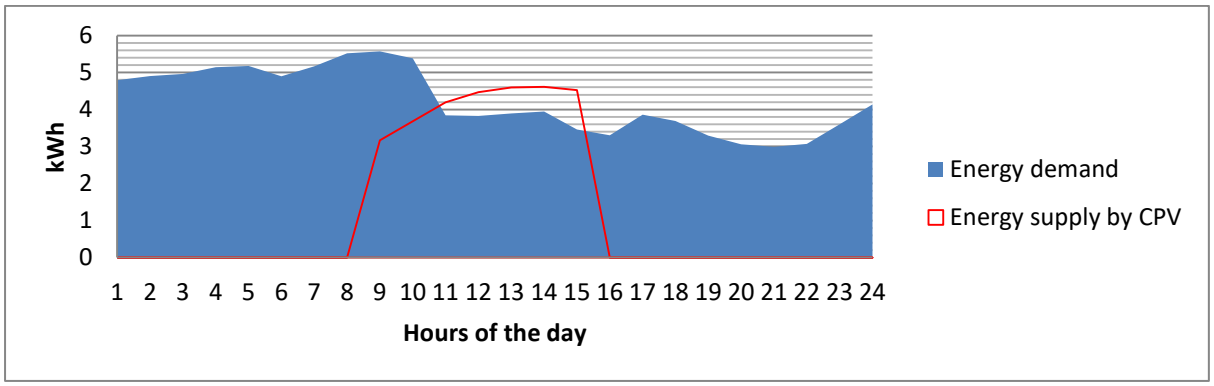

Figure 100: Demand vs Supply on March 19th, 2019 – spring equinox

As per figure 100, the system provides 67% of the daily need during the summer solstice of the year. The hours of operation considered during this day is from 0700 hours to 1900 hours.

16. "Net Metering." Net Metering | Entergy Arkansas | We Power Life, n.d. https://www.entergy-arkansas.com/net_metering.

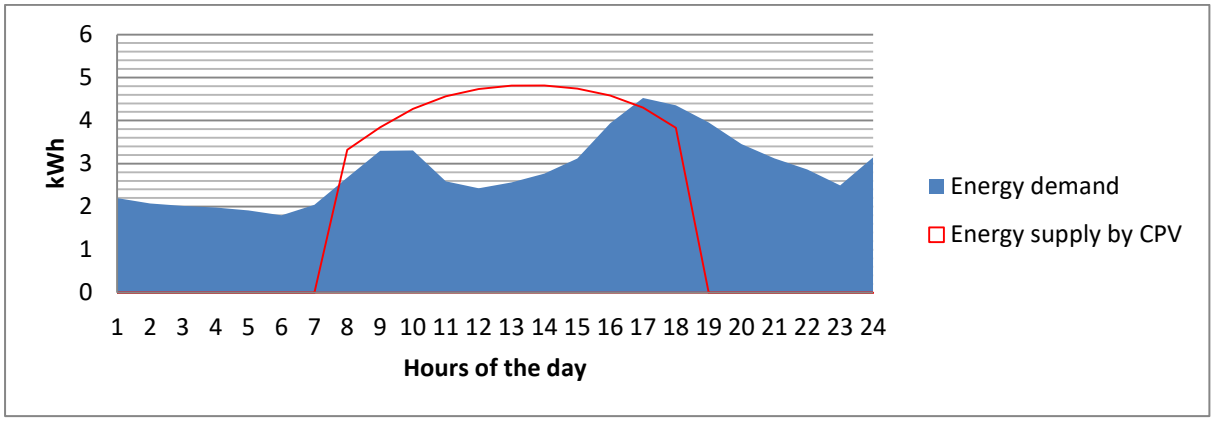

Figure 101: Demand vs Supply on June 21st, 2019 – summer solstice

The proposed system provides 68% of the daily need during the hottest day of the year. The hours of operation considered during this day is from 0700 hours to 1900 hours

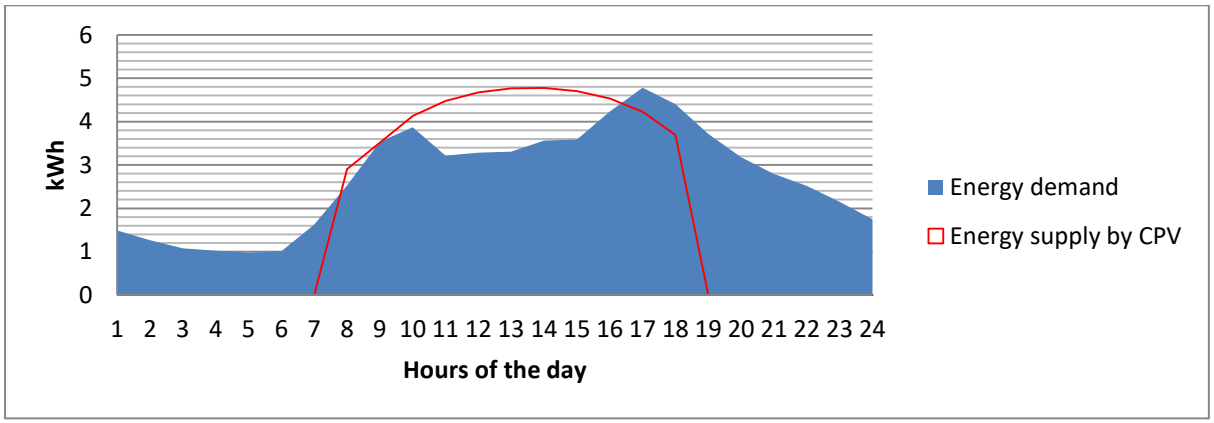

Figure 102: Demand vs Supply on August 13th, 2019 – hottest day

During fall equinox, the system provides 49% of the daily need during the summer solstice of the year. The hours of operation considered during this day is from 0800 hours to 1600 hours.

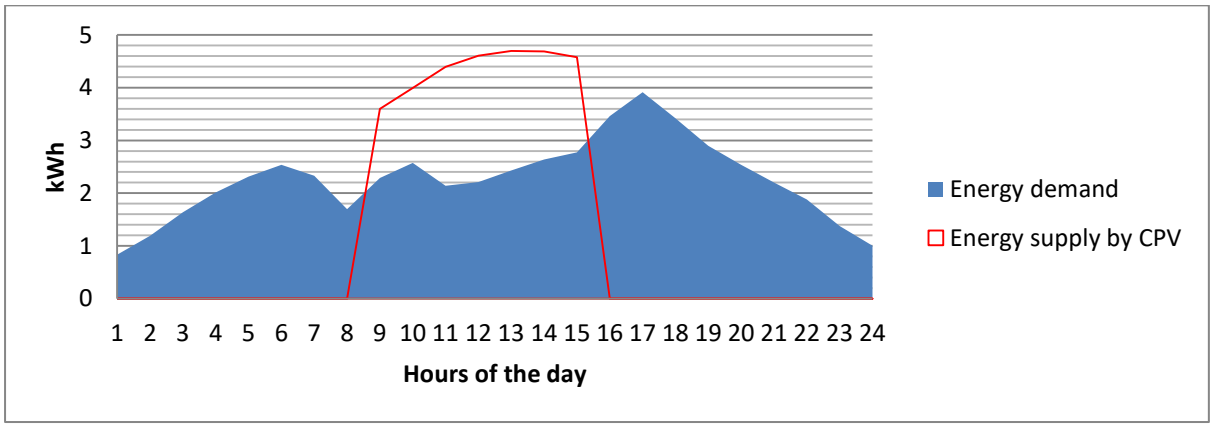

Figure 103: Demand vs Supply on September 23rd, 2019 – fall equinox

And finally, as shown in figure 103, the system provides 14% of the daily need during the winter solstice of the year. The hours of operation considered during this day is from 0800 hours to 1600 hours

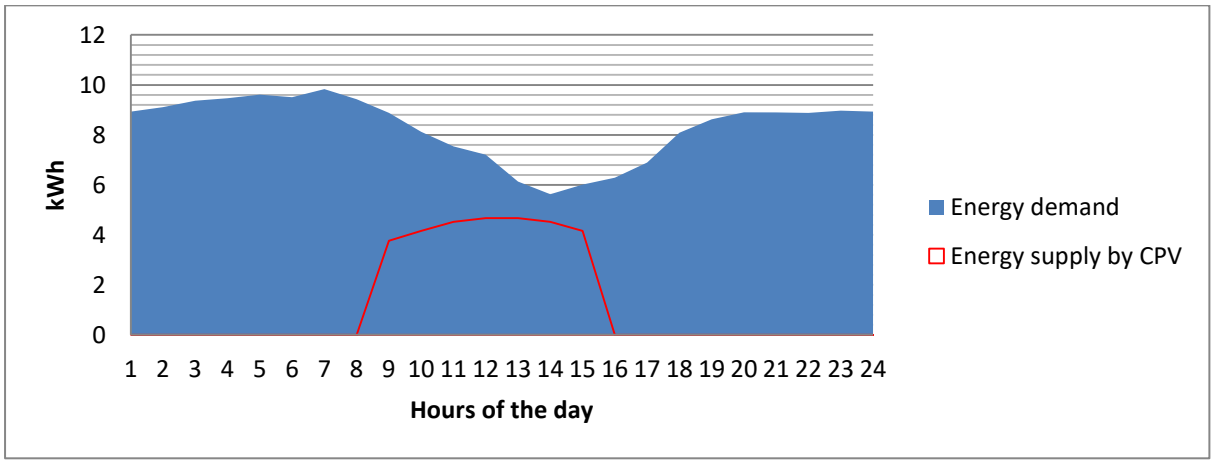

Figure 104: Demand vs Supply on December 21st, 2019 – winter solstice

6.7: Assumptions made in thermal modeling

The following assumptions were made in the optics section of the proposed model;

- The thermal calculations were made for clear sky conditions throughout the year.
- The thermal calculations did not account for other weather scenarios.
- The energy losses incurred in piping and transportation between collector and tank is neglected
- The output energy of the CPV is calculated based on highest uniformity of receiver surface
- The storage tank is assumed to be unstratified
- The energy calculation did not account for energy consumed by the proposed model
- The decrease in CPV efficiency due to the increase in absorber plate temperature is neglected
- The data presented is energy balance equation is based on a steady state analysis

7. Conclusion

In this research, the design aspect of the novel concentrator design is discussed briefly. The novel design proposed in the thesis can be made economical as the manufacturing process to produce spherical profile is easier. The proposed system is mathematically modelled and validated them through software simulation. It can reach up to a 65% overall efficiency with MJSC providing up to 30% input solar radiation. The optics design achieved **83%** optical efficiency and **20.66 (a.u.)** uniformity for collective reflector entity. The collective reflector entity is made up of spherical reflectors whose performance is in par with the paraboloidal reflectors. The excess heat from the receiver surface is used to provide heat energy for the residential domestic hot water and space heating throughout the year with the exception of winter.

The complexity of the system can be increased further by introducing a SOE to increase further concentration. Although the proposed technology has numerous advantages, the negative aspect needs to be addressed. The energy generation is carried out through a concentrated solar technology which can have an impact on the environment. The technology requires land space without shading effects or in order to operate at better position, it requires a specialised construction to accommodate the system. Maintenance is also required for smooth operation. The efficiency of the system is sub-par under cloudy conditions, as the design can work only under direct normal radiation. Feasibility of this project is higher for countries with better normal irradiance.

7.1: Contributions

- Through this research a novel design is proposed which has the possibility to promote sustainable energy, and replace conventional grid dependant centralised energy providers. A mathematical model is derived for the proposed system, and a design is implemented through a modeling software. This design encourages the use of cost effective circular mirrors.
- A design methodology for integration of the proposed model into hot water needs of residential building was developed.
- A variant of thermal serpentine model is used in the system for better heat dissipation to increase efficiency.

7.2: Future work

Lately, concentrated technologies have been a point of interest after the recent jump in the efficiency of MJSC. However, the predominant focus remains on power plants. The reverse approach of scaling down the concentrated technology, in order to utilise it on a residential scale can solve the purpose of distributed generation. This technology has the capability to change the dependency on other sources of energy as the efficiency of the proposed system is relatively higher. The possibilities of the proposed technology to combine with HVAC systems, and heat pumps are endless. A transient analysis on the proposed system can provide further insight on the application of this project. Further investigations to consider include;

- Investigation of a CPV/T vapour absorption system and performance analysis of the hybrid setup
- Integration of CPV along with heat pump and to meet heating and cooling demands
- Integration of CPV along with homogenizer to upgrade the MCPV/T to HCPV/T

References

Anderson, T.N., M. Duke, G.L. Morrison, and J.K. Carson. “Performance of a Building Integrated Photovoltaic/Thermal (BIPVT) Solar Collector.” *Solar Energy* 83, no. 4 (2009): 445–55. https://doi.org/10.1016/j.solener.2008.08.013.

Andreev, Vyacheslav M. “GaAs and High-Efficiency SPACE CELLS.” *McEvoy's Handbook of Photovoltaics*, 2018, 421–38. https://doi.org/10.1016/b978-0-12-809921-6.00011-2.

ASHRAE climatic design conditions 2009/2013/2017. Accessed August 23, 2021. http://ashrae-meteo.info/index.php?lat=34.727&lng=-92.239&place=%27%27&wmo=723403&si_ip=SI&ashrae_version=2017.

Aste, Niccolò, Claudio del Pero, and Fabrizio Leonforte. “Water Flat Plate Pv–Thermal Collectors: A Review.” *Solar Energy* 102 (2014): 98–115. https://doi.org/10.1016/j.solener.2014.01.025.

Barlett, R, M Halverson, V Mendon, J Hathaway, Y Xie, and M Zhao. Rep. *Arkansas Residential Energy Code Field Study: Baseline Report*, 2017.

Barrutia, L, I Garcia, C Algora, I Rey-Stolle, L Cifuentes, J Bautista, P Cano, et al. “Development of the Lattice Matched GaInP/GaInAs/Ge Triple Junction Solar Cell with an Efficiency over 40%.’ .” *2018 Spanish Conference on Electron Devices (CDE)*, November 2018. https://doi.org/10.1109/CDE.2018.8596996.

Bell, Louis. “Notes on the Early Evolution of the Reflector.” *Proceedings of the American Academy of Arts and Sciences* 57, no. 4 (1922): 69. https://doi.org/10.2307/20025889.

Benítez, Pablo, Juan C. Miñano, Pablo Zamora, Rubén Mohedano, Aleksandra Cvetkovic, Marina Buljan, Julio Chaves, and Maikel Hernández. “High Performance FRESNEL-BASED Photovoltaic Concentrator.” *Optics Express* 18, no. S1 (2010). https://doi.org/10.1364/oe.18.000a25.

Brogren, Maria. *Optical Efficiency of Low-Concentrating Solar Energy Systems with Parabolic Reflectors*. Uppsala: Univ, 2004.

Brunotte, M., A. Goetzberger, and U. Blieske. “Two-Stage Concentrator Permitting Concentration Factors up to 300x with One-Axis Tracking.” *Solar Energy* 56, no. 3 (1996): 285–300. https://doi.org/10.1016/0038-092x(95)00107-3.

Butti, Ken, and John Perlin. *2500 Years of Solar Architecture and Technology*. Van Nostrand Reinhold Inc., U.S., 1980.

Canavarro, D., J. Chaves, and M. Collares-Pereira. “New Optical Designs for Large Parabolic Troughs.” *Energy Procedia* 49 (2014): 1279–87. https://doi.org/10.1016/j.egypro.2014.03.137.

Canavarro, Diogo, Julio Chaves, and Manuel Collares-Pereira. “New Second-Stage CONCENTRATORS (XX SMS) for PARABOLIC Primaries; Comparison with

Conventional Parabolic Trough Concentrators." *Solar Energy* 92 (2013): 98–105. https://doi.org/10.1016/j.solener.2013.02.011.

Cariou, R, J Feldmann, O Hohn, H Hauser, P Beutel, B Blasi, D Lackner, et al. "III–V-on-Silicon Solar Cells Reaching 33% Photoconversion Efficiency in Two-Terminal Configuration." *Nature Energy 3*, April 2018. https://doi.org/10.1038/s41560-018-0125-0.

Chong, Kok-Keong, Tiong-Keat Yew, Chee-Woon Wong, Ming-Hui Tan, Woei-Chong Tan, and Boon-Han Lim. "Dense-Array Concentrator Photovoltaic Prototype Using Non-Imaging Dish Concentrator and an Array of Cross Compound Parabolic Concentrators." *Applied Energy* 204 (2017): 898–911. https://doi.org/10.1016/j.apenergy.2017.03.108.

de Greve, Bram. "Reflections and Refractions in Ray Tracing," November 13, 2006.

Dimroth, Frank, Thomas N. Tibbits, Markus Niemeyer, Felix Predan, Paul Beutel, Christian Karcher, Eduard Oliva, et al. "Four-Junction Wafer-Bonded Concentrator Solar Cells." *IEEE Journal of Photovoltaics* 6, no. 1 (2016): 343–49. https://doi.org/10.1109/jphotov.2015.2501729.

Duffie, John A., and William A. Beckman. *Solar Engineering of Thermal Processes*. Hoboken, NY: Wiley, 2013.

Eicker, Ursula. *Solar Technologies for Buildings*. Chichester: John Wiley & Sons, 2003.

Entergy Arkansas, LLC § (2019).

Feldman, Joel. "Vectors and Geometry in Two and Three Dimensions." *CLP-3 Multivariable Calculus*. Lecture presented at the University of British Colombia, January 23, 2011.

Fernández, Eduardo F., Antonio J. García-Loureiro, and Greg P. Smestad. "Multijunction Concentrator Solar Cells: Analysis and Fundamentals." *High Concentrator Photovoltaics*, 2015, 9–37. https://doi.org/10.1007/978-3-319-15039-0_2.

Fudholi, Ahmad, Kamaruzzaman Sopian, Mohammad H. Yazdi, Mohd Hafidz Ruslan, Adnan Ibrahim, and Hussein A. Kazem. "Performance Analysis of Photovoltaic Thermal (Pvt) Water Collectors." *Energy Conversion and Management* 78 (2014): 641–51. https://doi.org/10.1016/j.enconman.2013.11.017.

Fudholi, Ahmad, Kamaruzzaman Sopian, Mohammad H. Yazdi, Mohd Hafidz Ruslan, Adnan Ibrahim, and Hussein A. Kazem. "Performance Analysis of Photovoltaic Thermal (Pvt) Water Collectors." *Energy Conversion and Management* 78 (2014): 641–51. https://doi.org/10.1016/j.enconman.2013.11.017.

Gai, Boju, John F. Geisz, Daniel J. Friedman, Huandong Chen, and Jongseung Yoon. "Printed Assemblies of Microscale Triple-Junction Inverted Metamorphic Gainp/Gaas/Ingaas Solar Cells." *Progress in Photovoltaics: Research and Applications* 27, no. 6 (2019): 520–27. https://doi.org/10.1002/pip.3127.

Garland, J. W., T. Biegala, M. Carmody, C. Gilmore, and S. Sivananthan. “Next-Generation Multijunction Solar CELLS: The Promise of II-VI Materials.” *Journal of Applied Physics* 109, no. 10 (2011): 102423. https://doi.org/10.1063/1.3582902.

Geisz, J. F., Sarah Kurtz, M. W. Wanlass, J. S. Ward, A. Duda, D. J. Friedman, J. M. Olson, W. E. McMahon, T. E. Moriarty, and J. T. Kiehl. “High-Efficiency Gainp/Gaas/Ingaas Triple-Junction Solar Cells Grown Inverted with a Metamorphic Bottom Junction.” *Applied Physics Letters* 91, no. 2 (2007): 023502. https://doi.org/10.1063/1.2753729.

González, Juan C. “Design and Analysis of a CURVED Cylindrical Fresnel Lens That Produces High Irradiance Uniformity on the Solar Cell.” *Applied Optics* 48, no. 11 (2009): 2127. https://doi.org/10.1364/ao.48.002127.

“Graphing Calculator.” Desmos. Accessed August 23, 2021. https://www.desmos.com/calculator/5bdexxtcg1.

Hernández, M., P. Benítez, J. C. Miñano, A. Cvetkovic, R. Mohedano, O. Dross, R. Jones, D. Whelan, G. S. Kinsey, and R. Alvarez. “XR: A High-Performance PV Concentrator.” *High and Low Concentration for Solar Electric Applications II*, 2007. https://doi.org/10.1117/12.736910.

Jeff, HIrsch J. “EQUEST the Quick Energy Simulation Tool.” Computer software. *EQUEST*, March 2013. https://www.doe2.com/equest/.

Jing, Lei, Hua Liu, Huifu Zhao, Zhenwu Lu, Hongsheng Wu, He Wang, and Jialin Xu. “Design of Novel Compound Fresnel Lens for High-Performance Photovoltaic Concentrator.” *International Journal of Photoenergy* 2012 (2012): 1–7. https://doi.org/10.1155/2012/630692.

Kalogirou, Soteris. “Recent Patents in Solar Energy Collectors and Applications.” *Recent Patents on Engineering* 1, no. 1 (2007): 23–33. https://doi.org/10.2174/187221207779814644.

Kalogirou, Soteris. “Space and Concentrator Systems.” Essay. In *McEvoy's Handbook of Photovoltaics: Fundamentals and Applications*. London: Academic Press an imprint of Elsevier, 2018.

Kao, Yu-Cheng, Hao-Ming Chou, Shun-Chieh Hsu, Albert Lin, Chien-Chung Lin, Zun-Hao Shih, Chun-Ling Chang, Hwen-Fen Hong, and Ray-Hua Horng. “Performance Comparison OF Iii–v//Si AND III–V//InGaAs Multi-Junction Solar Cells Fabricated by the Combination of Mechanical Stacking and Wire Bonding.” *Scientific Reports* 9, no. 1 (2019). https://doi.org/10.1038/s41598-019-40727-y.

King, R R, D Bhusari, D Larrabee, X Q Liu, E Rehder, K Edmondson, H Cotal, et al. “Solar Cell Generations over 40% Efficiency.” *Progress in Photovoltaics: Research and Applications*, 2012. https://doi.org/10.1002/pip.1255.

Kottek, Markus, Jürgen Grieser, Christoph Beck, Bruno Rudolf, and Franz Rubel. “World Map of the Köppen-Geiger Climate Classification Updated.” *Meteorologische Zeitschrift* 15, no. 3 (2006): 259–63. https://doi.org/10.1127/0941-2948/2006/0130.

Languy, Fabian, Karl Fleury, Cédric Lenaerts, Jérôme Loicq, Donat Regaert, Tanguy Thibert, and Serge Habraken. “Flat Fresnel DOUBLETS Made Of PMMA and PC: Combining Low Cost Production and Very High Concentration Ratio for CPV.” *Optics Express* 19, no. S3 (2011). https://doi.org/10.1364/oe.19.00a280.

Lee, Bruno. “Passive Solar Building Design.” Lecture, n.d.

Lloyd, Humphrey. *Lectures on the Wave-Theory of Light*. Dublin: A. Milliken, 1841.

Long, Junhua, Meng Xiao, Xinping Huang, Zhiwei Xing, Xuefei Li, Pan Dai, Ming Tan, Yuanyuan Wu, Minghui Song, and Shulong Lu. “High Efficiency Thin Film GaInP/GaAs/InGaAs Inverted METAMORPHIC (Imm) Solar Cells Based On Electroplating Process.” *Journal of Crystal Growth* 513 (2019): 38–42. https://doi.org/10.1016/j.jcrysgro.2019.02.057.

Murphree, Quincy C. “A Point Focusing Double Parabolic Trough Concentrator.” *Solar Energy* 70, no. 2 (2001): 85–94. https://doi.org/10.1016/s0038-092x(00)00138-9.

“Net Metering.” Net Metering | Entergy Arkansas | We Power Life, n.d. https://www.entergy-arkansas.com/net_metering.

“Net Metering.” Net Metering | Entergy Arkansas | We Power Life. Accessed August 23, 2021. https://www.entergy-arkansas.com/net_metering.

Neubauer, Max, and Steven Nadel. Rep. *Advancing Energy Efficiency in Arkansas: Opportunities for a Clean Energy Economy; Report E104*, 2011.

Nijegorodov, N., P.K. Jain, and K.R.S. Devan. “A Non-Tracking, Cylindrical Solar Concentrator with Circular Cross-Section: Theoretical and Experimental Analysis.” *Renewable Energy* 6, no. 1 (1995): 1–9. https://doi.org/10.1016/0960-1481(94)00066-f.

Nilsson, J, R Leutz, and B Karlsson. “Micro-Structured Reflector Surfaces for a Stationary Asymmetric Parabolic Solar Concentrator.” *Solar Energy Materials and Solar Cells* 91, no. 6 (2007): 525–33. https://doi.org/10.1016/j.solmat.2006.11.003.

Nishioka, Kensuke, Tatsuya Takamoto, Takaaki Agui, Minoru Kaneiwa, Yukiharu Uraoka, and Takashi Fuyuki. “Evaluation of Temperature Characteristics of HIGH-EFFICIENCY InGaP/InGaAs/Ge Triple-Junction Solar Cells Under Concentration.” *Solar Energy Materials and Solar Cells* 85, no. 3 (2005): 429–36. https://doi.org/10.1016/j.solmat.2004.05.008.

Norton, Brian. “Solar Energy Thermal Technology,” 1992. https://doi.org/10.1007/978-1-4471-1742-1.

Pan, Jui-Wen, Jiun-Yang Huang, Chih-Ming Wang, Hwen-Fen Hong, and Yi-Ping Liang. “High Concentration and Homogenized Fresnel Lens without Secondary Optics Element.” *Optics Communications* 284, no. 19 (2011): 4283–88. https://doi.org/10.1016/j.optcom.2011.06.019.

Pereira, José Carlos, Jorge Cruz Fernandes, and Luís Guerra Rosa. “Mathematical Models for Simulation and Optimization of High-Flux Solar Furnaces.” *Mathematical and Computational Applications* 24, no. 2 (2019): 65. https://doi.org/10.3390/mca24020065.

Pereira, José Carlos, Jorge Cruz Fernandes, and Luís Guerra Rosa. “Mathematical Models for Simulation and Optimization of High-Flux Solar Furnaces.” *Mathematical and Computational Applications* 24, no. 2 (2019): 65. https://doi.org/10.3390/mca24020065.

Philipps, Simon P., and Andreas W. Bett. “Iii-v Multi-Junction Solar Cells and Concentrating Photovoltaic (Cpv) Systems.” *Advanced Optical Technologies* 3, no. 5-6 (2014). https://doi.org/10.1515/aot-2014-0051.

Rinaldi, F., M. Binotti, A. Giostri, and G. Manzolini. “Comparison of Linear and Point Focus Collectors in Solar Power Plants.” *Energy Procedia* 49 (2014): 1491–1500. https://doi.org/10.1016/j.egypro.2014.03.158.

Rogers, Steven C., Connor Barickman, Greg Chavoor, Matt Kinni, Nik Glazar, and Peter V. Schwartz. “Concentrating Sunlight with an Immobile Primary Mirror and Immobile Receiver: RAY-TRACING RESULTS.” *Solar Energy* 86, no. 1 (2012): 132–38. https://doi.org/10.1016/j.solener.2011.09.012.

Saleh Ali, Imhamed M., Tadhg S. O’Donovan, K.S. Reddy, and Tapas K. Mallick. “An Optical Analysis of a Static 3-d Solar Concentrator.” *Solar Energy* 88 (2013): 57–70. https://doi.org/10.1016/j.solener.2012.11.004.

Sasaki, Kazuaki, Takaaki Agui, Katsuya Nakaido, Naoki Takahashi, Ryusuke Onitsuka, and Tatsuya Takamoto. “Development of Ingap/Gaas/Ingaas Inverted Triple Junction Concentrator Solar Cells,” 2013. https://doi.org/10.1063/1.4822190.

Sellami, Nazmi, and Tapas K. Mallick. “Optical Efficiency Study of PV Crossed Compound Parabolic Concentrator.” *Applied Energy* 102 (2013): 868–76. https://doi.org/10.1016/j.apenergy.2012.08.052.

Shanks, Katie, S. Senthilarasu, and Tapas K. Mallick. “Optics for Concentrating Photovoltaics: Trends, Limits and Opportunities for Materials and Design.” *Renewable and Sustainable Energy Reviews* 60 (2016): 394–407. https://doi.org/10.1016/j.rser.2016.01.089.

Silvi, Cesare. “The Future of Solar Energy.” *Leonardo* 28, no. 4 (1995): 325. https://doi.org/10.2307/1576198.

“Simulation Software: Engineering in the Cloud.” SimScale, August 19, 2021. https://www.simscale.com/.

Sirimanna, M. P., and J. D. Nixon. “Effects of Mirror Geometry on the Optical Efficiency of a Linear Fresnel Reflector (Lfr).” *Renewable Energy and Sustainable Buildings*, 2019, 337–47. https://doi.org/10.1007/978-3-030-18488-9_26.

Stine, William B, and Michael A Geyer. “Power from the Sun.” The Library of Congress, 2010. https://www.loc.gov/item/lcwaN0004585/.

Swanson, Richard M. “The Promise of Concentrators.” *Progress in Photovoltaics: Research and Applications* 8, no. 1 (2000): 93–111. https://doi.org/10.1002/(sici)1099-159x(200001/02)8:1<93::aid-pip303>3.0.co;2-s.

Takamoto, Tatsuya, Hidetoshi Washio, and Hiroyuki Juso. “Application of Ingap/Gaas/Ingaas Triple Junction Solar Cells to Space Use and Concentrator Photovoltaic.” *2014 IEEE 40th Photovoltaic Specialist Conference (PVSC)*, 2014. https://doi.org/10.1109/pvsc.2014.6924936.

Takamoto, Tatsuya, Minoru Kaneiwa, Mitsuru Imaizumi, and Masafumi Yamaguchi. “Ingap/Gaas-Based Multijunction Solar Cells.” *Progress in Photovoltaics: Research and Applications* 13, no. 6 (2005): 495–511. https://doi.org/10.1002/pip.642.

Thomas, Geroge B. *Thomas' Calculus*. Boston, MA: Pearson, 2013.

“Total Energy - U.S. Energy Information Administration (EIA).” Total Energy - U.S. Energy Information Administration (EIA). Accessed August 23, 2021. https://www.eia.gov/totalenergy/.

Tzivanidis, C., E. Bellos, D. Korres, K.A. Antonopoulos, and G. Mitsopoulos. “Thermal and Optical Efficiency Investigation of a Parabolic Trough Collector.” *Case Studies in Thermal Engineering* 6 (2015): 226–37. https://doi.org/10.1016/j.csite.2015.10.005.

“U.S. Energy Information Administration - Eia - Independent Statistics and Analysis.” U.S. energy facts explained - consumption and production - U.S. Energy Information Administration (EIA). Accessed August 23, 2021. https://www.eia.gov/energyexplained/us-energy-facts/.

“What Is U.S. Electricity Generation by Energy Source? - FAQ - U.S. Energy Information Administration (EIA).” Frequently Asked Questions (FAQs) - U.S. Energy Information Administration (EIA). Accessed August 23, 2021. https://www.eia.gov/tools/faqs/faq.php?id=427&t=3.

Wilson, Eric, Craig Christensen, Scott Horowitz, Joseph Robertson, and Jeff Maguire. “Electric End-Use Energy Efficiency Potential in the U.S. Single-Family Housing Stock,” 2017. https://doi.org/10.2172/1339938.

Winston, Roland. “Nonimaging Optics an Overview.” *Optics and Photonics News* 6, no. 11 (1995): 33. https://doi.org/10.1364/opn.6.11.000033.

Yamaguchi, Masafumi, and Kenji Araki. “Concentrated Solar Cells.” *Encyclopedia of Sustainability Science and Technology*, 2019, 1–34. https://doi.org/10.1007/978-1-4939-2493-6_1062-1.

Yamaguchi, Masafumi, Tatsuya Takamoto, Kenji Araki, and Nicholas Ekins-Daukes. “Multi-Junction Iii–v Solar Cells: Current Status and Future Potential.” *Solar Energy* 79, no. 1 (2005): 78–85. https://doi.org/10.1016/j.solener.2004.09.018.

Yang, Wei-Chen, Chieh Lo, Chin-Ying Wei, and Wen-Shiung Lour. “Cell-Temperature Determination in InGaP–(In)GaAs–Ge Triple-Junction Solar Cells.” *IEEE Electron Device Letters* 32, no. 10 (2011): 1412–14. https://doi.org/10.1109/led.2011.2163294.

Zamora, P., A. Cvetkovic, M. Buljan, M. Hernandez, P. Benitez, J. C. Minano, O. Dross, R. Alvarez, and A. Santamaria. “Advanced Pv Concentrators.” *2009 34th IEEE Photovoltaic Specialists Conference (PVSC)*, 2009. https://doi.org/10.1109/pvsc.2009.5411135.

Zanganeh, G., R. Bader, A. Pedretti, M. Pedretti, and A. Steinfeld. “A Solar Dish Concentrator Based on Ellipsoidal Polyester Membrane Facets.” *Solar Energy* 86, no. 1 (2012): 40–47. https://doi.org/10.1016/j.solener.2011.09.001.

Zhuang, Zhenfeng, and Feihong Yu. “Optimization Design of Hybrid Fresnel-Based Concentrator for GENERATING Uniformity Irradiance with the Broad Solar Spectrum.” *Optics & Laser Technology* 60 (2014): 27–33. https://doi.org/10.1016/j.optlastec.2013.12.021.

Appendices

Appendix A: Solar insolation

The Sun can be considered as a hemispherical blackbody that provides radiation through space as a result of its temperature of about 6000°C. The solar constant which is a measurement of flux density of electromagnetic radiation received on a unit area falling perpendicular to its surface has 1367 W/m^2.

When sunlight enters the atmosphere of the earth, the intensity (extra-terrestrial radiation) is reduced by various factors by about 30%. The light is scattered through atmospheric molecules and dust particles which is caused by Rayleigh scattering. These scattered lights are absorbed and reflected back into space. Based on clear sky model approximately 1000 W/m^2 reaches the ground. However, this clear sky data is greatly influenced by atmospheric conditions and the position of the Earth with respect to the Sun.

The term air mass (AM) is defined as the ratio of the actual path length travelled by solar radiation through the atmosphere to the shortest path length it can travel (sun is directly overhead).

$$m = \frac{1}{\cos(\theta z)}$$

Where

m = air mass coefficient
θ_z = zenith angle (degrees)

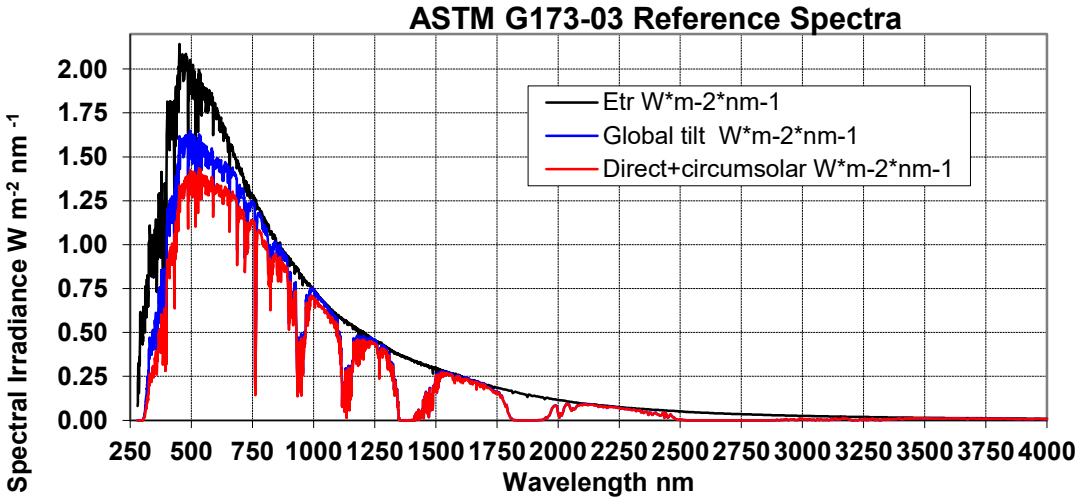

Figure 105: ASTM G173-03 Reference Spectra derived from SMARTS v. 2.9.2

The ASTM G173 emphasize on the use of AM1.5 solar spectrum for testing and rating of solar energy components for terrestrial applications and it is obtained at $\theta_z = 48°$. Air mass zero (AM0) refers to the absence of atmospheric attenuation. AM1.5 solar spectrum attenuates atmosphere where incident radiation is approximated to 970 W/m^2, while the intensity of solar radiation is about 1367 W/m^2 at AM0 solar spectrum.

In order to conclude the amount of solar energy that can be harvested at a particular geographic location, the resources should be characterized. The irradiance is the solar irradiation incident on the surface. The total irradiance on the surface, (I_t) comprises of 2 components, direct radiation (I_b) which has solar radiation travelled in a straight path directly

from the sun, and the diffuse radiation, (I_d) which is received due to solar radiation scattered by molecules in the atmosphere and reflected from surface earth.

$$I_t = I_b + I_d$$

Where

I_t = Total solar irradiation (Watts / metre^2)
I_b= Beam direct radiation (Watts / metre^2)
I_d= Beam diffuse radiation (Watts / metre^2)

Appendix B: Solar radiation on inclined surface

The position of the sun relative to an inclined surface can be described using different angles. For concentrated solar applications the diffuse radiation is neglected and only direct beam radiation or beam normal irradiance is taken into account.

$$\delta = 23.45\ ^{o} \sin\left(360\ ^{o} \times \frac{N+284}{365}\right)$$

Where

N = Day number of the year
δ = Solar declination

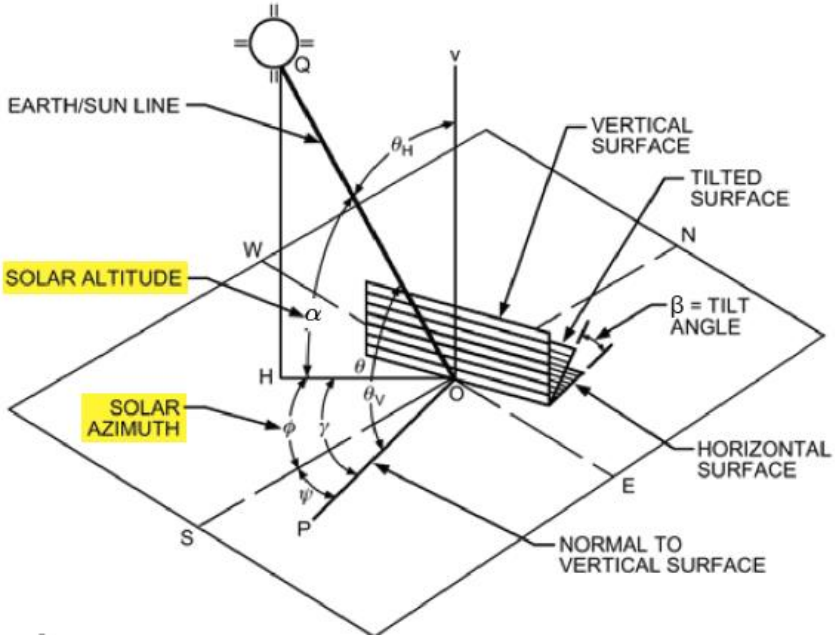

Figure 106: Schematics of Solar angles

$$AST = LST + (LSTM - Long)\frac{4\ min}{deg} + ET$$

Where

LST = Local standard time (in minutes)

Long = Longitude, and
LSTM = local longitude of standard time meridian (Montreal: 75 º W)

$$ET = 2.2918[0.0075 + 0.1868 \cos(\Gamma) - 3.2077 \sin(\Gamma) - 1.4615 \cos(2\Gamma) - 4.089 \sin(2\Gamma)]$$

Where

ET = Equation of time (in minutes)
$\Gamma = 360^{\circ} \times \frac{N-1}{365}$
N = Day number of the year

$$h = 15 (AST - 12)$$

Where

h = Hour angle (in minutes)
AST = Apparent solar time (in minutes)

$$\sin \alpha = \cos L \times \cos \delta \times \cos H + \sin L \times \sin \delta$$

$$\cos \varphi = \frac{\sin \alpha . \sin L - \sin \delta}{\cos \alpha . \cos L} \frac{h}{|h|}$$

Where

α = Solar altitude angle (in degrees)
L = Latitude (in degrees)
δ = Declination angle (in degrees)
φ = Azimuth angle (in degrees)

$$E_o = E_{sc} \{1 + 0.033 \cos [360^{\circ} \times \frac{(N-3)}{365}]\}$$

$$E_b = E_o \exp [-\tau_b m^{ab}]$$

$$ab = 1.454 - 0.406 \tau_b - 0.268 \tau_d + 0.021 \tau_b \tau_d$$

Where

E_o = Extra-terrestrial normal irradiance (Watts/metre^2)
E_{sc} = Solar constant (1367 W/m^2)
E_b = Beam normal irradiance (Watts/metre^2)
τ_b = Clear sky optical depth for beam irradiance
τ_d = Clear sky optical depth for diffuse irradiance
m = air mass coefficient
ab = beam air mass exponent

$$\gamma = \varphi - \psi$$

Where

γ = Solar surface azimuth angle (in degrees)
φ = Solar azimuth angle (in degrees)
ψ = Surface azimuth angle (in degrees)

$$\cos \theta_i = \cos(\alpha) \times \cos|\gamma| \times \sin(\beta) + \sin(\alpha) \times \cos(\beta)$$

where
α = Solar altitude angle (in degrees)
γ = Solar surface azimuth angle (in degrees)
β = Tilt angle (in degrees)
θ_i = Incidence angle (in degrees)

$$I_b = E_b \times \cos \theta_i$$

where

I_b = Normal beam radiation

E_b = Beam normal irradiance (Watts/metre^2)

Appendix C: Steady state analysis

A steady state analysis was carried out with conjugate heat transfer on the Absorber plate temperature. The customised serpentine model is validated through computational fluid dynamics software.[17] It plays a vital role in understanding the temperature of the back side of the panel.

Input heat flux power: 10,000 W
Mass flow rate: 0.1 kg/s
Inlet temperature of water: 17.7 ºC
Ambient temperature: 25 ºC

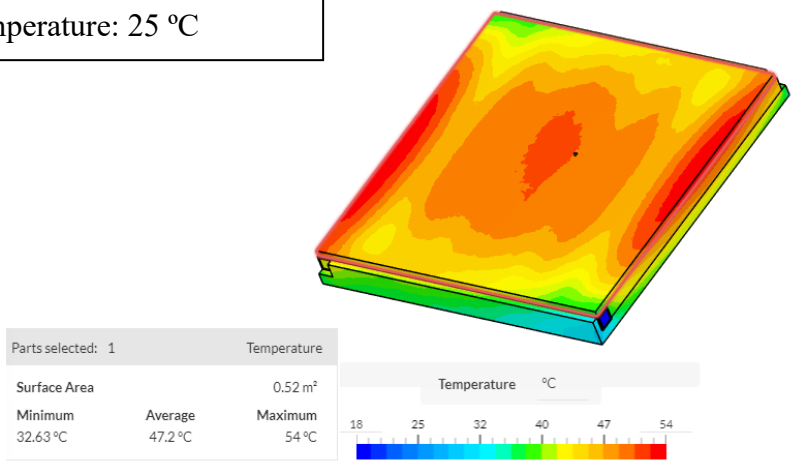

Figure 107: Temperature distribution on the receiver at highest concentrated solar irradiation

17. "Simulation Software: Engineering in the Cloud." SimScale, August 19, 2021. https://www.simscale.com/.

The temperature variation on the absorber plate for the highest incident of concentrated solar radiation 40,000 W/m^2 (10,000 W) at 0.1 kg/s flow rate of water is shown in figure 107. The average temperature of the receiver is 47.2 ºC.

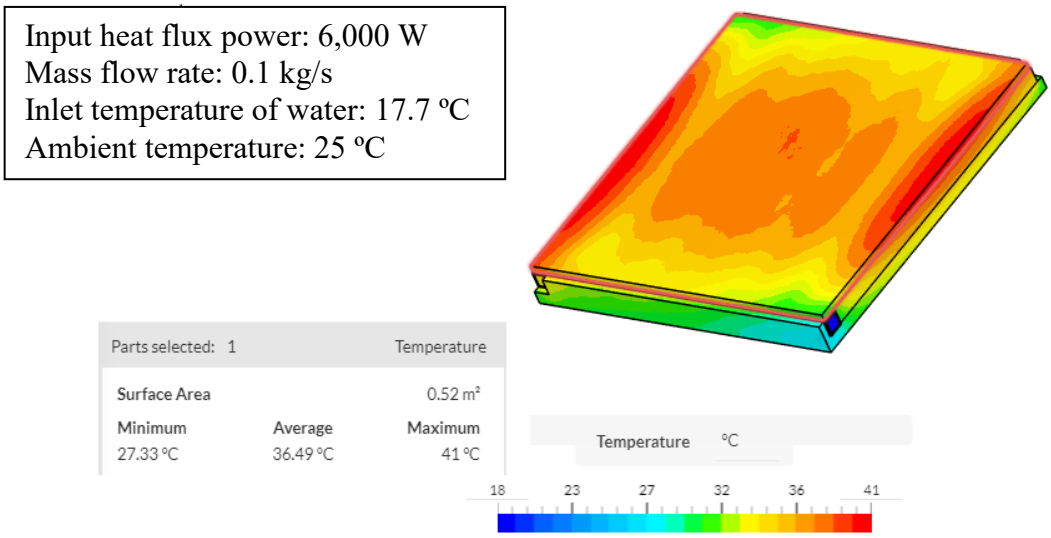

Figure 108: Temperature distribution on the receiver at lowest concentrated solar irradiation

The temperature variation on the absorber plate for the lowest incident of concentrated solar radiation 24,000 W/m^2 (6,000 W) at 0.1 kg/s flow rate of water is shown in figure 108. The average temperature of the receiver is 36.5 ºC.